ATOMIC SCALE INVESTIGATION OF MOLECULAR SELF-ASSEMBLY AND SINGLE MOLECULE MANIPULATION ON SURFACES

ZHANG JIALIN

(B.Sc. SICHUAN UNIVERSITY)

A THESIS SUBMITTED

FOR THE DEGREE OF DOCTOR OF PHILOSOPHY

DEPARTMENT OF PHYSICS

NATIONAL UNIVERSITY OF SINGAPORE

(2014)

Declaration

I hereby declare that this thesis is my original work and it has been written by me in its entirety. I have duly acknowledged all the sources of information which have been used in the thesis.

This thesis has also not been submitted for any degree in any university previously.

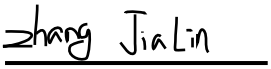

ZHANG JIALIN

25 July 2014

Dedicated to my beloved family, boyfriend and friends.

Acknowledgement

I would like to thank all those people who have given me help, support and encouragement during my PhD life.

First and foremost, I would like to take this opportunity to express my deepest gratitude towards my supervisor Prof. Chen Wei for his continuous support of my PhD study and research. I appreciate all his contributions of time, ideas and encouragement to make my PhD experience stimulating. Even though when occupied with work, his tireless review of my manuscripts as well as the valuable comments provided by him have never failed to impress me. Without his guidance and persistent help, this thesis would not have been possible.

I would also like to thank the group members in the Surface Science Laboratory: Dr. Niu Tianchao, Dr. Wong Swee Liang, Dr. Huang Han, Dr. Huang Yuli, Dr. Pan Feng, Dr. Yao Guanggeng, Dr. Xu Wentao, Ms. Lin Jiadan, Ms. Zhong Shu, Mr. Zhong Jianqiang, Dr. Mao Hongying, Mr. Wang Rui, Mr. Han Cheng and so many others for the stimulating discussions, for the days we were working together, and for all the fun we have had in our lab. I would also like to thank Mr. Wong for his kind help in our daily laboratory management. Their companionship throughout the course of my PhD study is priceless and will be sorely missed.

In particular, I would like to mention my deepest thanks for Tianchao,

who spent a lot of time and effort teaching me the experimental operations, helping me with the equipment maintenance and answering the scientific questions of mine. He never refused any request for help nor took any credit for the great assistance he has rendered in my projects. He is always willing to help others and I was very lucky to work together with him.

I would like to express my sincere thanks to Prof. Andrew Wee Thye Shen for his valuable comments on my manuscript. I am also thankful to Prof. Liu Lei, Prof. Li Zhenyu, Mr. Xu Jilian and Ms. Wang Zhunzhun for their great help in conducting the DFT calculations.

Finally, I would like to thank my family for all their endless love and supports throughout my life. Special thanks to my loving, supportive and patient boyfriend Mr. Jianfeng, his faithful support and love is so appreciated not only during my pursuit of the doctorate but also my entire life.

List of Publications

1. J. L. Zhang, K. H. L. Zhang, J. Q. Zhong, T. C. Niu, W. Chen, "LT-STM/UPS investigation of two-dimensional crystallization of C_{60}: pentacene binary system on Ag(111)", J. Appl. Phys. **111**, 034304 (2012).
2. J. L. Zhang, T. C. Niu, A. T. S. Wee, W. Chen, "Self-assembly of binary molecular nanostructure arrays on graphite", Phys. Chem. Chem. Phys. **15**, 12414-12427 (2013).
3. J. L. Zhang, J. L. Xu, T. C. Niu, Y. H. Lu, L. Liu, W. Chen, "Reversible switching of single dipole molecule imbedded in two dimensional hydrogen-bonded binary molecular networks", J. Phys. Chem. C **118**, 1712-1718 (2014).
4. J. L. Zhang, Z. Z. Wang, T. C. Niu, Z. Y. Li, W. Chen, "Single molecule tunneling spectroscopy investigation of reversibly switched dipolar vanadyl phthalocyanine on graphite", Appl. Phys. Lett. **104**, 113506 (2014).
5. J. L. Zhang, Z. Z. Wang, T. C. Niu, S. N. Wang, Z. Y. Li, W. Chen, "Elementary process for CVD graphene on Cu(110): size-selective carbon clusters", Sci. Rep. **4**, 4431 (2014).
6. T. C. Niu, J. L. Zhang, W. Chen, "Molecular ordering and dipole alignment of vanadyl phthalocyanine monolayer on metals: the effects of interfacial interactions", J. Phys. Chem. C **118**, 4151-4159 (2014).
7. T. C. Niu, C. G. Zhou, J. L. Zhang, S. Zhong, H. S. Cheng, W. Chen, "Substrate reconstruction mediated unidirectionally aligned molecular dipole dot arrays", J. Phys. Chem. C **116**, 11565-11569 (2012).
8. T. C. Niu, M. Zhou, J. L. Zhang, Y. P. Feng, W. Chen, "Dipole orientation reduction of ClAlPc on Cu(111)", J. Phys. Chem. C **117**, 1013-1019 (2013).
9. T. C. Niu, M. Zhou, J. L. Zhang, Y. P. Feng, W. Chen, "Growth intermediates for CVD graphene on Cu(111): carbon clusters and defective graphene", J. Am. Chem. Soc. **135**, 8409-8414 (2013).
10. J. Q. Zhong, X. Qin, J. L. Zhang, S. Kera, N. Ueno, A. T. S. Wee, J. Yang, W. Chen, "Energy level realignment in weakly interacting donor-acceptor binary molecular networks", ACS Nano **8**, 1699-1707 (2014).

11. D. Xiang, C. Han, J. L. Zhang, W. Chen, “Gap states assisted MoO_3 nanobelt photodetector with wide spectrum response”, Sci. Rep. **4**, 4891 (2014).

12. S. Zhong, J. Q. Zhong, H. Y. Mao, J. L. Zhang, J. D. Lin, W. Chen, “The role of gap states in the energy level alignment at the organic-organic heterojunction interfaces”, Phys. Chem. Chem. Phys. **14**, 14127-14141 (2012).

13. J. Q. Zhong, H. Y. Mao, R. Wang, J. D. Lin, Y. B. Zhao, J. L. Zhang, D. G. Ma, W. Chen, “Ionization potential dependent air exposure effect on the MoO3/organic interface energy level alignment”, Org. Electron. **13**, 2793-2800 (2012).

Table of Contents

Summary

The concept of using single molecules as key building blocks for logic gates, diodes, transistors and switches to perform the basic function of digital electronic device are well established over the past decades. To achieve this, three essential steps are required. First, the desired function should be encoded in a single molecule. Second, the molecules should be coupled to a support substrate and wired to a molecular matrix without suppressing their switching performance. Third, appropriate external stimuli should be applied to turn the functional molecules between on and off states. In this thesis, we use the low-temperature scanning tunneling microscope (LT-STM) to study the molecular self-assembly and single-molecule manipulation within self-assembled monolayers on graphite. Dipolar phthalocyanine molecules are selected as the functional molecules due to their permanent electric dipole moment. Directional and selective intermolecular interactions have been used to assemble them into single-component or binary supramolecular nanostructures with high degree of controllability and tunability. To minimize the substrate effect, atomically flat and chemically inert graphite are used as the substrate for single-molecule manipulation study.

We begin with an investigation of C_{60}: pentacene binary system on Ag(111) to demonstrate how to construct two-dimensional (2D) molecular nanostructure arrays on surfaces through self-assembly. A reversible switching of single-dipole molecule within the single-component vadanyl

phthalocyanine (VOPc) monolayer is then presented, and spatially resolved scanning tunneling spectroscopy is used to identify the electronic structures of VOPc with different dipole orientation. Finally, single-dipole molecule switching is extended to binary molecular networks formed by co-assembly of chloroaluminium phthalocyanine (ClAlPc) and perfluoropentacene (PFP) on graphite, density function theory calculations are carried out to reveal the reasonable switching pathway. The details are given below.

First, we demonstrate the fabrication of a variety of well-ordered C_{60} molecular arrays including C_{60} nanomesh networks, C_{60} pentamers, and C_{60} pairs on Ag(111) by controlling the annealing temperature for the C_{60}-pentacene binary molecular system. To evaluate the effect of molecule-substrate interfacial interactions on the 2D crystallization, the same self-assembly experiments of C_{60} on monolayer pentacene covered graphite substrate has also been carried out. As the interfacial interactions between C_{60} and graphite are weak, C_{60} on pentacene on graphite can be used as a good model system to understand the nature of C_{60}-pentacene intermolecular interactions by using in situ ultraviolet photoelectron spectroscopy (UPS). It is revealed that formation of different C_{60} arrays is ascribed to the subtle interplay between C_{60}-pentacene intermolecular interaction, C_{60}-Ag(111) and pentacene-Ag(111) interfacial interactions. These results suggest that controlling the self-assembly or 2D crystallization processes of binary molecular systems represents a versatile route to fabricating novel 2D

molecular architectures.

We then show the ability of STM to switch a single-dipole molecule VOPc between bistable configurations in self-assembled closely-packed monolayer on graphite. Through the combination of STM measurement and density functional theory (DFT) simulations, we assign these two bistable configurations as O-up and O-down configurations. By controlling the polarity of the pulse voltage applied to the tip, VOPc molecules can be switched between O-up and O-down configurations. Moreover, the spatially resolved scanning tunneling spectroscopy (STS) measurements allow the identification of the electric structures of VOPc with different dipole orientation. The combination of STM and STS enable the complementary investigation of the adsorption geometry and electronic properties of a single molecule at the surface.

For practical applications, incorporation of these molecular switches into more complex nano-architectures is needed. Hence, we investigate the reversible switching of another single-dipole molecule, ClAlPc, imbedded in 2D hydrogen-bonded ClAlPc:PFP molecular networks on graphite. By varying the binary molecular ratio, the interdipole distance of the molecular dipole dot arrays and the dipole densities can be easily tuned with atomic precision. Moreover, formation of multiple intermolecular hydrogen bonding can further enhance the structure stability of these molecular nanostructure arrays during device operation. By controlling the polarity of the pulse voltage applied to the

STM tip, ClAlPc molecules can be switched between Cl-up and Cl-down configurations without affecting the neighboring molecules. As corroborated by DFT calculations, we propose that the switching is achieved by "shuttling" the Cl atom between two sides of the ClAlPc molecular plane.

List of Tables

List of Figures

List of Abbreviations

LT-STM	Low-Temperature Scanning Tunneling Microscope
LODS	Local Density of States
$F_{16}CuPc$	Hexadecafluorophthalocyanine
DFT	Density Functional Theory
MnPc	Manganese Phthalocyanine
BuSMe	Butyl Methyl Sulphide
3D	Three-dimensional
SnPc	Tin Phthalocyanine
HOMO	Highest Occupied Molecular Orbital
LUMO	Lowest Unoccupied Molecular Orbital
SMM	Single-Molecule Magnets
$TbPc_2$	Double-Decker Bis(phthalocyaninato) Terbium (III) Complex
SOMO	Singly Occupied Molecular Orbital
PDOS	Partial Density of States
PTCDA	Perylene-3,4,9,10-Tetracarboxylic Dianhydride
1D	One-Dimensional
2D	Two-Dimensional
SCOF	Surface Covalent Organic Frameworks

Br_xTPP	Bromophenyl Porphyrin
PTCDI	Perylene Tetra-Carboxylic Di-Imide
MOCN	Metal-Organic Coordination Networks
DBA	Dehydrobenzo Annulene
TCB	1,2,4-Trichlorobenzene
6P	P-Sexiphenyl
PVBA	4-[Trans-2-(pyrid-4-yl-vinyl)] Benzoic Acid
ZnOEP	Zinc Octaethylporphyrin
VOPc	Vanadyl Phthalocyanine
ClAlPc	Chloroaluminium Phthalocyanine
PFP	Perfluoropentacene
IETS	Inelastic Electron Tunneling Spectroscopy
STS	Scanning Tunneling Spectroscopy
UHV	Ultra High Vacuum
UPS	Ultraviolet Photoelectron Spectroscopy
SECO	Secondary-Electron Cut-Off
HIB	Hole Injection Barrier
IP	Ionization Potential
IPES	Inverse Photoemission Spectroscopy
QCM	Quartz Crystal Microbalance

LEED	Low Energy Electron Diffraction
HOPG	Highly Oriented Pyrolytic Graphite
OPVs	Organic Photovoltaic Cells
VB	Valence Band
XPS	X-ray Photoelectron Spectroscopy
FeTPPCl	Iron Tetraphenylporphyrin Chloride
NEB	Nudged-Elastic- Band

Chapter 1: Introduction

In the early 1970s, the visionary concept of using individual molecules as active electronic component to construct the electronic circuit was sketched out by Arieh Aviram and Mark Rather.[1] Since then, molecular electronics has been considered as a revolutionary successor to conventional semiconducting electronics. Stimulated by this initial proposal, researchers around the world begin to explore the properties and opportunities of single molecules.[2-12] However, the real development of molecular electronics only started during the past two decade coupled with the explosion of the nanoscience and the availability of manipulation techniques at the single molecule scale.[13, 14] At the beginning, miniaturization and cost reduction were the main driving forces and provided the impetus to develop a variety of experimental platforms to probe the electronic transport phenomena at the single molecule level.[15-17] Tremendous advances have been achieved over the past several years. Elegant examples include the demonstration of simple molecular devices, such as molecular wires, two terminal molecular diodes and switches, and three terminal transistor-like devices; development of different approaches to fabricate and measure electron transport in molecular junctions; optimization of the theoretical methods for describing simple molecular systems; emergence of new characterization tools that help to bridge the gap between theoretical calculation and experimental data and so on. Though substantial progress has been made over the past decade, there are still some major issues

along the way. The molecule-electrode contact has a profound effect on the conductance of the molecule. Precise control of the contact geometry at the molecule-electrode interface has been a difficult challenge. The preferred material for electrode is gold or platinum, and sulphur, amine or a number of lone-pair species are typically used to attach the molecule. Another big problem involves the large fluctuations in the conductance measurement of single molecules. The random fulctuations between two or several discrete levels has been observed in metal-molecule-metal junctions. They are not a fundamental limit in device applications, but must be controlled. Current-induced instability and local heating also has substantial effects in the nanojunction. For theory, owing to the lack of atomic-scale details of most experiment, the treatment of the contact geometry is an important step for a fair comparision between theories and experiments. Further development to include realistic treatment of molecule-electrode interface is critical. Although it is tempting to use molecular electronics to mimic concepts that form the basis of silicon devices, these approaches haven't really made the most out of the molecules' potential. Molecular electronics would only "grow up" if it looked beyond the border of conventional electronics and simple transport models, and explored the intrinsic functionality of molecules.[18-22] Indeed, contemporary research in molecular electronics is already moving in this direction.

Molecules often possess unique properties that have no parallel in

conventional material. Rational design of molecules with specific functionality promise new hybrid devices with functions that cannot be achieved with equivalent solid-state devices. Novel applications include coupling the light with molecule for optoelectronic devices;[12, 23-25] exploring the electromechanical properties for molecular machines;[26-28] manipulating the electron's spin for memory devices or spintronic devices;[29-37] utilizing the unique recognition properties for molecular sensors.[38-40] The most appealing example of a functional molecule is formed by a molecular switch. The realization of molecular switches relies on three steps. First, the desired function should be encoded in a single molecule. Second, the molecules should be wired into circuits with atomic precision. Third, appropriate external stimuli should be applied to turn the functional molecules between on and off states.

Over the years, molecular switches on surfaces are intensely investigated.[41-73] A variety of external stimuli like light,[62, 69] electric field,[42, 56] temperature[70] and tunneling electrons[43-49, 58, 63, 65, 67, 68] can be used to activate these molecular switches between bistable[41-48] or even multiple states.[67, 68] Depending on properties of the molecules, they can be operated by changing conformations,[42-47, 54-57, 59-62, 67-71] charge states,[48-51, 53] spin states[64, 65] or even bond formation.[52] For such molecule to be used as electronic components, they should be coupled to a support substrate and wired to a molecular matrix without suppressing their switching performance. Self-assembly represents a

promising bottom up approach to integrate these molecules into circuits on surfaces.[74]

In this chapter, various molecular switches on surface are reviewed first. We begin by presenting the molecular switches triggered by various external stimuli which do not provide single molecule selectivity. Then, special focus is given to single molecule manipulation induced by low-temperature scanning tunneling microscope (LT-STM), which offers unique opportunities to operate individual switches on the atomic scale. In what follows, we give a brief introduction of the bottom-up molecular self-assembly on surfaces. Finally, the objective and scope of this thesis are addressed.

1.1 Molecular Switches on Surfaces

1.1.1 Non Selective Switching Triggered by Various External Stimuli

Molecular switches, which can be interconverted between bistable or even multiple states by external stimuli like light,[62, 69] electric field, [42,56] temperature,[70] electrons[43-49, 58, 63, 65, 67, 68] or even chemical modifications,[75, 76] have attracted much attention. Most of the switching processes are studied by LT-STM. In this case, both the local topography and electronic configurations can be probed before and after the switching. The atomic scale characterization can not only provide the fundamental understanding of the interaction between the molecule and the external stimuli, but also help to find a better way of engineering the functionality of the molecule from rational chemical design. In the following, we will introduce the various external

stimuli in more detail.

1.1.1.1 Light Induced Switching

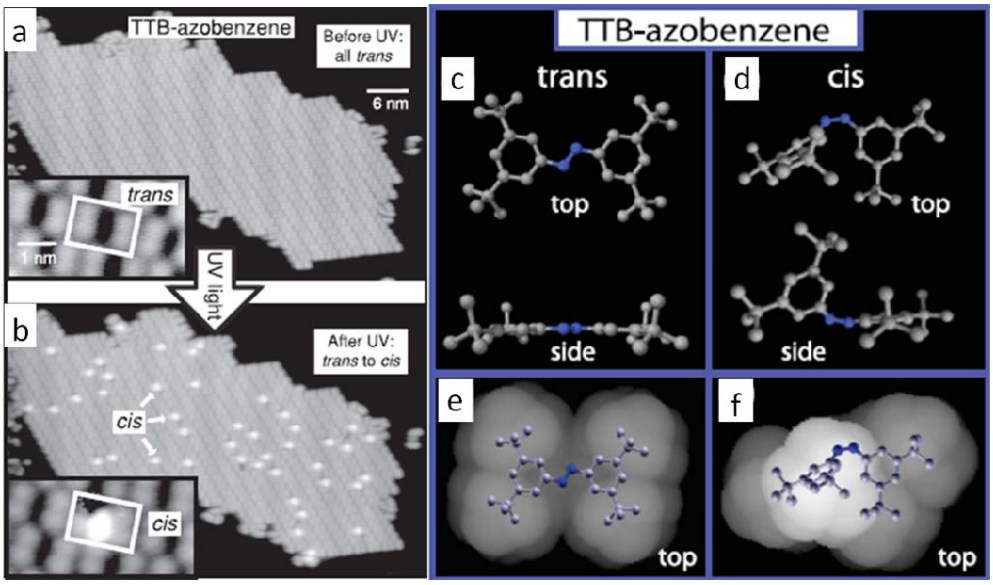

Figure 1.1 (a) Same island of TTB-azobenzene molecules before and (b) after a 3h exposure to 90 mW/cm^2 UV irradiation at 375 nm. (c) Calculated trans geometry. (d) Calculated cis geometry. (e) Calculated trans LDOS integrated from E_F to E_F-1eV, at an isosurface about 3 Å away from the nearest atoms. (f) Calculated cis LDOS isosurface. Reprinted from ref. 62, with permission from the American Physical Society, copyright 2007.

Photochromic systems can convert light energy into mechanical energy, thus they can be used as building blocks for the fabrication of prototypes of molecular devices that are based on photomechanical effect. Among photochromic molecules, azobenzenes have been extensively investigated for their photoisomerization.[56, 59, 62, 77, 78] They can reversibly transform from one isomeric state to another upon adsorption of light in gas and solution-phase. But this process can be quenched at a surface due to the molecule-surface coupling. By attaching four tert-butyl "leg" (TB: C_4H_9) to an azobenzene scaffold ($C_{12}H_{10}N_2$), Comstock et al. demonstrated the reversible light-induced mechanical switching between trans and cis states on Au(111).[62] The TB legs

lifted the azobenzene molecules from the substrate, thereby increasing molecular photomechanical activity by decreasing molecule-surface coupling. Figure 1.1a and 1.1b shows the same island of TTB-azobenzene (four TB legs) molecules on Au(111) before and after a 3h exposure to UV light. Before UV exposure the island is uniformly composed of the trans isomer, which displays four peripheral lobes. After UV exposure the emergence of new, bright protrusions can be seen in the island, which can be attributed to the cis isomer of TTB-azobenzene. The calculated geometry and local density of states (LDOS) isosurface intergrated from E_F to E_F-1eV for trans and cis azobenzenes are shown in Figure 1.1c-1.1f, which are in good agreement with the experimentally observed molecules. Many applications profiting from the conformational rearrangement of the molecule have been proposed, such as optical data storage devices, sensors and light-powered molecular machines.

1.1.1.2 Electric Field Induced Switching

Another way to induce molecular switching is to make use of the electric field. In the presence of an electric field, the potential energy surface related to the reaction can be deformed, thus leading to an effective lowering of the switching barrier. This effect depends on the presence and orientation of an intrinsic dipole moment, as well as the polarizability of the molecule.[42] Using the same azobenzene molecule as shown above, Alemani et al. showed an electric field induced reversible trans-cis isomerization by STM.[56] The isomerization experiments were performed by positioning the STM tip at a

fixed height above a molecular island with the feedback loop off and applying

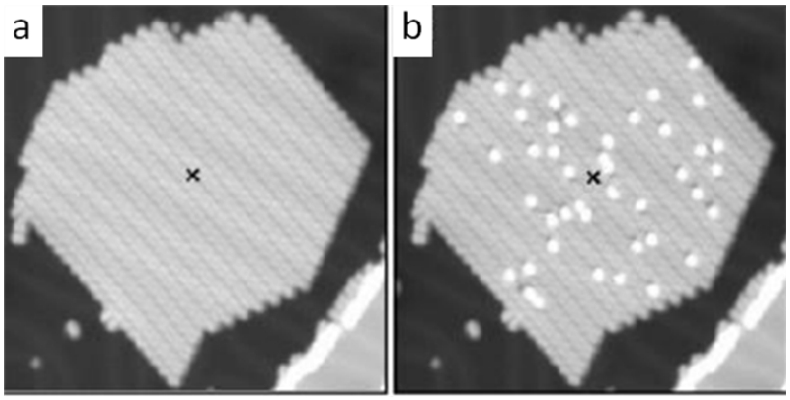

Figure 1.2 (a) Island of trans-TBA containing about 400 molecules (37 × 37 nm^2). Subsequent voltage pulses (20s, V_{sample} = 2 V, tip height = 6 Å) are applied at the position indicated by the cross. (b) STM image after nine pulses: 43 molecules have been switched to the cis form. Reprinted from ref. 56, with permission from the American Chemical Society, copyright 2006.

a pulse voltage V to the sample. The STM images before and after nine equivalent pulses are shown in Figure 1.2a and 1.2b. Many molecules have changed their appearance from the trans form to the cis form. They investigated the dependence of the voltage on the tip height and found that the threshold voltage increases when retracting the tip. The isomerization process occurs also at very large tip distances where no tunneling current is flowing. Moreover, it is also possible to isomerize molecules when the tip is positioned above the bare surface nearby the island. All these observations, together with the large extension over which switched molecules are observed, lead to the conclusion that the trans-cis isomerization is driven by the electric field in the STM junction. An intriguing finding by the comparison of the light induced and electric field induced switching is that the different external stimuli can be used to operate the very same molecule.

1.1.1.3 Temperature Induced Switching

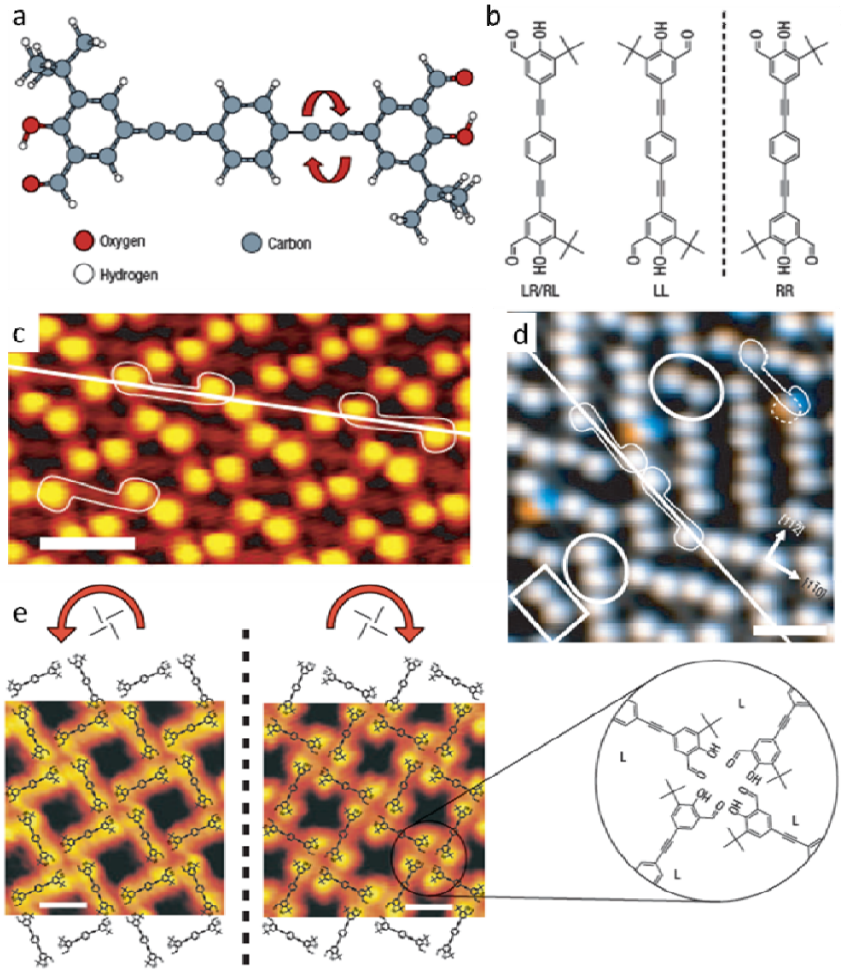

Figure 1.3 (a) Chemical structure of the investigated molecule. (b) Three distinct surface conformers, two of which are enantiomers. R and L indicate the position (right and left) of the t-butyl group with respect to the molecular backbone as seen from the centremost benzene ring. (c) Constant current STM image of the brick-wall adsorption structure attained under tip conditions primarily revealing the t-butyl groups. (d) Overlay of two STM images taken with a time separation of 168s (V_{sample} = 1.96 V, I = 0.4 nA, T_{sample} = 180 K, scale bar 2nm). Blue (orange) indicates the initial (final) positions of t-butyl groups that change position, whereas stationary groups appear grey. Two cis-trans and one trans-cis (right most in image) flips are shown. Outlines of three molecules are indicated as well as stationary cis (rectangle) and trans (circles) arrangements of endgroups. The indicated line follows the direction of the molecular backbones. Reprinted from ref. 70, with permission from Nature Publishing Group, copyright 2006.

In some molecular system, the energy barrier between the two molecular states is relatively low. In that case, it is possible to switch a molecule by

thermal excitation. Such temperature induced switching is, however, not very directional. Switching will occur in both directions unless there is a significant energy difference between the two isomers of the molecules. Weigelt et al. investigated a model system in which adsorbed molecules switched between enantiomeric forms as they underwent thermally induced conformational changes.[70] The chemical structure of the investigated molecule is shown in Figure 1.3a. Vapor deposition of this compound onto the inert herringbone reconstructed Au(111)-(22×√3) surface results in two coexisting adsorption phases. In the phase shown in Figure 1.3c, the molecules adsorb with their backbone parallel to the substrate and align into rows that are shifted relative to each other by half the repeat distance along the rows, analogous to the stacking in a brick wall. As shown in Figure 1.3b, three surface conformers exist: one achiral meso-form (LR/RL) and two chiral enantiomers (LL and RR). From time-lapse sequence of STM images, it is found that the bright protrusions ascribed to t-butyl groups occasionally change position from one side of the molecular backbone to the other. Such shifts are illustrated in Figure 1.3d by superimposing two time-separated STM images of the same position of the surface. This spontaneous flipping process implies that the molecules can change between different surface conformers, specifically from chiral (RR/LL) to achiral (RL/LR) or vice versa. The observed conformational changes have implications for the chiral ordering on surfaces. As shown by the coexisting second phase in Figure 1.3e, the molecules connect to form two

windmill-like arrangements with different chirality. Each chiral form of the tiling pattern consists of entirely one of the two chiral surface conformers (LL/RR). The homochiral assembly on surfaces is of interest for heterogeneous asymmetric catalysis.

1.1.1.4 Tunneling Electron Induced Switching

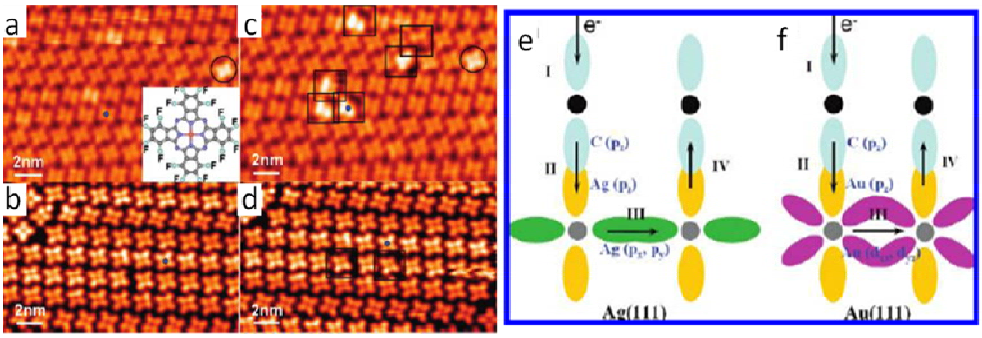

Figure 1.4 (a) STM images of $F_{16}CuPc$ molecules adsorbed on Ag(111) surface and (b) Au(111) surface before pulsing. (c) STM images of $F_{16}CuPc$ molecules on Ag(111) and (d) Au(111) after a pulse at -3.0 V and -3.2 V on top of the target molecule. The blue dot, rectangles, and circles represent pulsing position, reacted molecules, and bright molecules not induced by pulsing. (e) Schematic cartoons illustrating the electron transport process. Electron capture in π^* orbitals of molecules (step I), transfer from molecule to surface metal atoms (II), propagation in hybridized states of metal atoms (III), then back capture in π^* orbitals of another molecule (IV) on Ag(111) and (f) Au(111). Black and gray solid circles represent C atoms of molecules and metal atoms at the surface. Reprinted from ref. 91, with permission from the American Chemical Society, copyright 2009.

There has been a long effort in surface science for the understanding of the interaction between the electron and adsorbates on the surface. Different mechanisms can be involved, including desorption induced by electron transition,[79] resonance enhanced electron stimulated desorption,[80] desorption induced by multiple electron transition and dissociative electron attachment.[81, 82] But the surface phenomena are not limited to desorption. Using STM as an

electron source, various modifications of the adsorbates which cannot be obtained with conventional sources can be characterized by STM.[83-85] Surface phenomena such as desorption,[86] dissociation,[87] hopping,[88] rotation[89] and chemical reactions[90] can be observed as a consequence of electronic excitation or vibrational excitation. By injecting hot electrons from a STM tip, Chen et al. demonstrated the nonlocal chemical reactivity of one monolayer copper hexadecafluorophthalocyanine (F_{16}CuPc) adsorbed on two different substrates, Ag(111) and Au(111).[91]

Figure 1.4a and 1.4b shows the STM images of F_{16}CuPc molecules adsorbed on Ag(111) and Au(111) surface before pulsing. After applying a pulse on the target molecule on Ag(111), they found that one of the four ligands has disappeared. Such a chemical reaction is not limited to the molecule under the STM tip. As shown in Figure 1.4c (pulsed at -3.0 V tip bias, 3.5 nA, 50 ms), the reaction occurs on five molecules at different distances from the STM tip, too. This nonlocal chemical reaction can be observed as far as 12 nm from the STM tip in some cases. Similar nonlocal behavior was also observed for molecules on Au(111), where one ligand of the reacted molecules is shortened by the pulse (Figure 1.4d). They determined the threshold voltage for this nonlocal chemical reaction to be -1.9 V and -2.4 V for Ag(111) and Au(111) respectively. The relatively high energy suggests that the reaction proceeds via electronic excitations of the molecule. If the reaction is induced by tunneling electrons, the reaction rate R_0, the current I_0

and the reaction order n should obey the relation $R_0 = I_0^n$. By investigating the switching rate as a function of the tunneling current, they deduced that the reaction order is ~4 (~2) for Ag (Au) and interpreted the single-molecule reaction as a four-electron (two-electron) process for molecules on Ag(111) (Au(111)). They proposed that the observed shorter of ligand was caused by C-F bond dissociation. The mechanism is known as dissociative electron attachment,[92] in which electrons with specific energies can be captured into the antibonding π* orbitals of the molecule, and then transferred into the σ* orbital, causing bond breaking. To explain the nonlocal reactions, the mechanism of lateral hot-electron propagation is proposed. Density functional theory (DFT) calculations reveals that the mixing of molecular orbitals with metal surface states is the main channel facilitating the propagation of hot electrons, as shown in the schematic in Figure 1.4e and 1.4f. Electrons propagating in a metal surface can back-transfer into the π* orbitals of another molecule through the "bridge" formed between molecule and substrate, leading to another defluorination reaction.

1.1.1.5 Chemical Stimulus Induced Switching

Planar organometallic complexes with extended π-conjugation, for example, metalloprophyrins and metallophthalocyanines, have indispensable role in controlling a wide range of functionalities.[93-95] Their chemical properties can be varied by changing the metal ion in the center or by attaching different functional groups to the macrocycle. Moreover, the

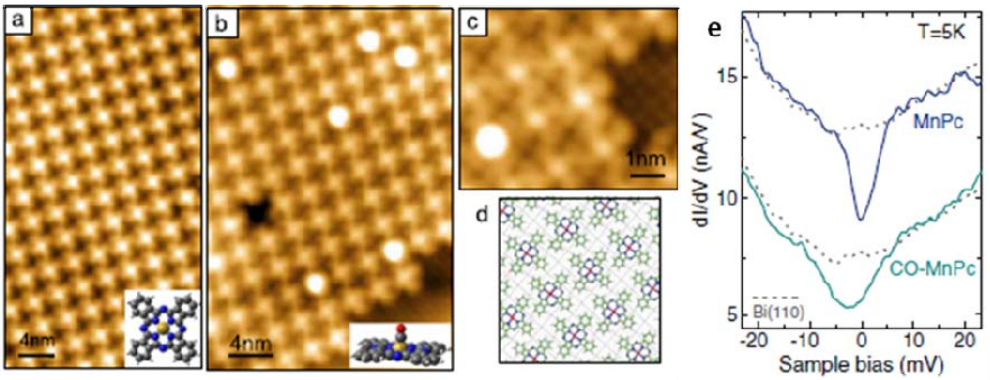

Figure 1.5 (a) STM image of a highly ordered MnPc island (V_{sample} = 250mV, I = 0.2 nA). (b) MnPc island after exposure to CO (V_{sample} = 180 mV, I = 0.2 nA). CO-coordianted molecules can be distinguished by different apparent heights. Inset images in (a) and (b) show schematic pictures of the chemical structure of MnPc and CO-MnPc. (c) High resolution STM image of bare and CO-ligated MnPc (V_{sample} = -250 mV, I = 0.1 nA). (d) Adsorption model of MnPc on Bi(110). (e) dI/dV spectra of MnPc and CO-coordianted MnPc in the bias range close to E_F, showing the zero bias anomaly. The dotted plots are the spectra measured on a bare Bi surface as a reference. Reprinted from ref. 76, with permission from the American Physical Society, copyright 2012.

coordinatively unsaturated character of the metal center can act as a local reactive site for the ligand attachment, which opens a unique possibility of controlling their properties by external chemical stimuli.[96-99] The coordination of gas molecules to the metal center usually causes measurable changes in molecule-substrate interaction,[96] color,[39] or even magnetic properties of the metal complex,[100] which make them as promising candidates for applications in gas sensors,[39] catalysis[101] and molecular spintronics.[75] Recently, Stróżecka et al. demonstrated a chemical control over the molecular spin of manganese phthalocyanine (MnPc) by coordination of CO molecule.[76] Figure 1.5a and 1.5b shows the densely packed MnPc islands on Bi(110) before and after CO exposure. Several molecules exhibiting larger apparent height in Figure 1.5b are identified as CO-ligated MnPc, where a single CO bonds directly to the

Mn ion. The corresponding high resolution image is shown in Figure 1.5c. The differential conductance (dI/dV) spectra measured close to the E_F on MnPc reveals a pronounced anomaly at zero bias, which is a fingerprint of the Kondo effect (Figure 1.5d). When similar spectra are measured on CO-MnPc molecules, the zero bias anomaly appears much broader, with a slightly different line shape. This indicates that the coordination to CO modifies the magnetic state of the molecule. DFT calculations reveals that the spin of the MnPc molecule is reduced from S=3/2 to S=1 upon adsorption. CO ligation further reduces the spin of the MnPc from S=1 to S=1/2. CO affects the magnetic state of MnPc in two ways. First, it increases the splitting of the d orbitals, hence leading to the low spin configuration; second, it reduces the coupling of the d orbitals to the substrate. They also demonstrated that this modification is reversible and can be controlled by selective removal of CO molecule using the STM tip.

A common feature of the above mentioned external stimuli is that they don't provide single molecule selectivity. Although the tunneling electrons from the STM tip have the possibility to manipulate single molecule, in the special case we choose, the lateral transport of the hot electron induces the nonlocal reactions. In next section, we will focus on the STM tip-assisted single molecule manipulation.

1.1.2 Selective Single Molecule Manipulation Studied by STM

Since its invention in the early 1980s by G. Binnig and H. Roher, STM

has been a powerful tool in real-space imaging of surface structures with atomic resolution, as well as in characterization of the electronic and vibrational structures of the surface adsorbates. Besides using the STM tip for a measurement, STM also offers the fascinating possibility of single molecule manipulation. Manipulation of molecules intends a controlled change in their position, switching between different conformations, electronic and chemical structures, or inducing chemical reactions.[84, 85] A variety of tip-molecule interactions can be used in a controlled manner to manipulate single molecules, such as electric field existing at the tip-sample junction, tunneling electrons, and tip-molecule interaction forces. In the following, we will first review various STM tip induced single molecule motion on surfaces. After that, special focus is given to STM tip manipulated single molecule switches.

1.1.2.1 Molecular Motion

Lateral Manipulation

An STM manipulation procedure to relocate a single molecule across a surface is known as the "lateral manipulation". This procedure involves approaching the tip toward a target molecule at its initial location to increase the tip-molecule interaction force, and then scanning the tip along a desired path until it reaches a predetermined destination. The molecule moves along with the tip, and when the tip retracts back to the normal imaging height, it is left behind on the surface. Based on the nature of the tip-molecule interactions, the manipulation can have three modes: pulling, pushing and sliding. In the

pulling mode, the molecule follows the tip due to an attractive tip-molecule interaction. In the pushing mode, a repulsive tip-molecule interaction drives the molecule to move in front of the tip. In the sliding mode, the atom is virtually bound to or trapped under the tip and it moves smoothly across the surface together with the tip. [102]

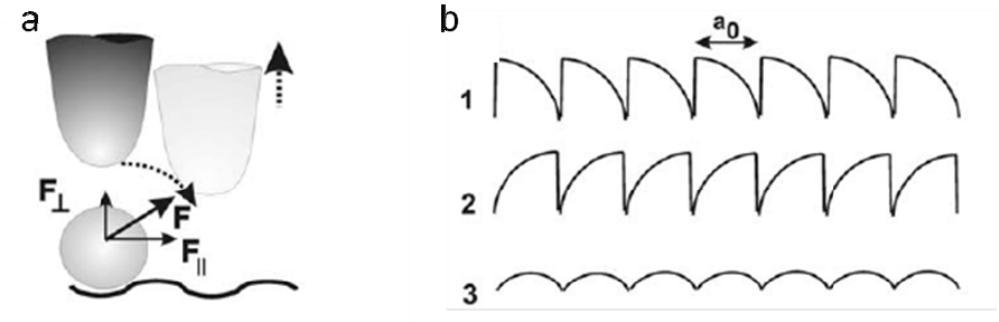

Figure 1.6 (a) Schematic drawing demonstrates the vertical and parallel force components involved in lateral manipulation. (b) STM tip-height manipulation curves correspond to (1) pulling, (2) pushing, and (c) sliding modes. Reprinted from ref. 102, with permission from the AIP Publishing LLC, copyright 2005.

During the lateral manipulation, the tip height signal (in constant-current mode) or the tunneling current signal (in constant-height mode) can be recorded as a function of the lateral tip position. These manipulation signals can give direct insight into the molecular motion. Figure 1.6a shows the schematic diagram of force components involved in a lateral manipulation process in constant current mode.[102] When $F_{||}$ overcomes the hopping barrier of the molecule, it can hop to the next adsorption site under the tip. Repeating this sequence produces a saw-tooth like tip-height curve, as shown in Figure 1.6b. The slopes are different during pushing or pulling, having an ascending or descending edge, respectively. In the sliding mode, the molecule smoothly

moves across the surface together with the tip, and the tip-height signal usually shows the contour of the surface atoms. Eigler and Schweizer first demonstrated this kind of lateral manipulation in 1990 by writing the "IBM" letters with Xe atoms on a Ni(110) surface.[103]

Vertical Manipulation

Vertical manipulation involves the transfer of a single molecule between the tip and the substrate. The transfer process can be realized by using an electric field between the tip and the sample, by making mechanical contact with the molecule or by exciting with inelastic tunneling electrons. The transfer mechanism can be explained using a double potential well model, as shown in Figure 1.7b.[85] At an imaging distance where the tip is roughly 6 Å above the sample, the manipulated molecule has two possible stable positions, one at the surface and one at the tip apex. Each position is represented by a potential well and the two potential wells are separated by a vacuum barrier in between. When an electric field is applied between the tip and the sample, the shape of the double potential well will change. The barrier between the two wells is reduced, depending on the bias polarity on the tip, and hence the molecule can be transferred from the surface to the tip or vice versa. In the mechanical contact regime, the tip height is reduced until the contact has been achieved. In this case, the two potential wells overlap and the molecule can be easily transferred between the tip and the surface.

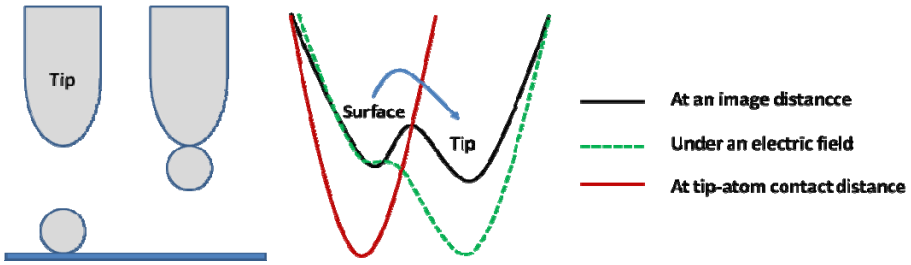

Figure 1.7 (a) A schematic drawing shows the vertical manipulation process. (b) The double-potential well model. The black (solid), dash and gray curves represent the shape of potentials at an image-height, under an electric field, and at the tip-molecule contact, respectively.

Bartels et al. demonstrated the electron-induced vertical manipulation of individual CO molecules on Cu(111).[86] A temporary attachment of a tunneling electron into the CO 2π* antibonding state leads to the breakup of the CO-Cu bond. The resultant excited CO molecule can jump either to the nearby Cu surface sites or toward the tip, and it can be transferred back to the surface using the same method. The vertical manipulation process can be used to functionalize the probe tip, which can both improve the tip sharpness and define the tip apex with determined chemical constitution. The application of functionalized tips has proven useful in non-contact atomic force microscopy. A CO functionalized AFM tip can be used to reveal the atoms and bonds within molecules and is even able to image the C-H bonds.[104]

Rotation and Rolling

For molecules to be used as components in molecular machines, methods that couple individual molecules to external energy sources and that selectively excite the motion of the molecule in a given direction are highly required.

Significant progress has been made in the construction of molecular motors powered by light,[105] chemical reactions[106] and tunneling electrons[107] from STM.

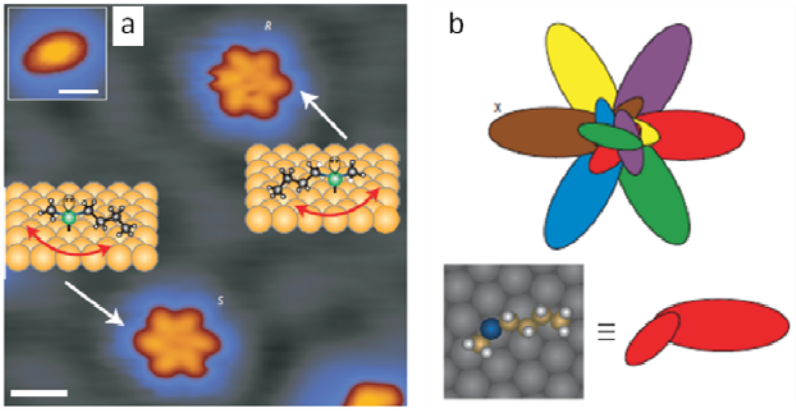

Figure 1.8 (a) A STM image of the two enantiomeric forms of BuSMe, R and S, adsorbed on a Cu(111) surface. The pinwheel appearance of the molecule arises from the rotation of the alkyl groups around the central sulphur atom. BuSMe is achiral in the gas phase, but becomes chiral when bound to a surface. The molecules in the main panel rotate because of the high tunneling current used to form the image. The inset shows a static BuSMe rotor imaged under non-perturbative conditions. Scale bars, 1nm. (Main panel: V_{tip} = 0.1 V, I = 300 pA, T = 7K; inset: V_{tip} = 0.07 V, I = 5 pA, T = 5 K.) (b) The direction of rotation of the BuSMe molecule by following its progression between six equivalent orientations on the Cu(111) surface (top). A model of the BuSMe molecule on the Cu(111) surface, with the sulphur atom shown in blue, and the representation used in the schematic. Reprinted from ref. 26, with permission from Nature Publishing Group, copyright 2011.

Tierney et al. reported that a butyl methyl sulphide molecule adsorbed on a copper surface can be operated as a single molecule electric motor.[26] Butyl methyl sulphide (BuSMe) is one of a family of thioether molecular rotors. As shown in Figure 1.8a, when adsorbed on the Cu(111) surface, thioethers rotate around the central sulphur-metal bond and appear hexagonal in shape because of the three-fold symmetry of the underlying hexagonal surface. The rotation of thioethers is driven electrically by tunneling electrons with high energy, by

excitation of a C-H vibration, which couples to the rotation of the molecule. Under non-perturbative conditions, the molecules stop rotating and appear as crescent-shaped protrusions, as shown in the inset in Figure 1.8a.

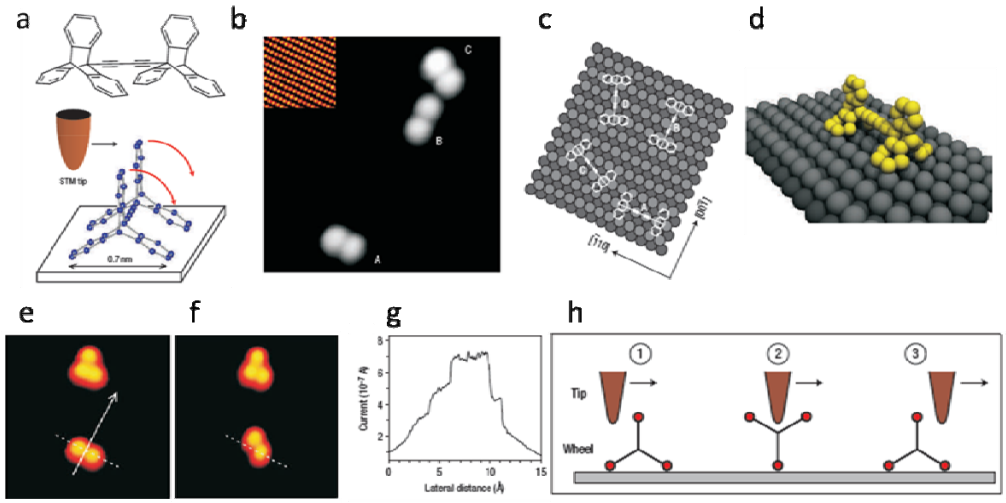

Figure 1.9 (a) Chemical structure of the wheel-dimer molecule ($C_{44}H_{24}$) and scheme of a manipulation using the STM tip to induce a rolling motion (arrows indicated the rotation of the wheels). (b) STM image of three wheel-dimer molecules adsorbed on Cu(110) (13 × 13 nm^2). The inset shows the substrate in atomic resolution (4 × 4 nm^2, V_{sample} = 0.1 V, I = 1 nA). (c) Schematic representation showing that four different orientations A-D can be distinguished. (d) Calculated molecular configuration of the wheel-dimer in orientation A, adsorbed parallel to the closed packed copper rows. (e) STM images before and (f) after manipulation. Arrows mark the pathway of the tip apex during the manipulation and dashed lines indicated the initial position of the wheel-dimer molecules (all images 9 × 9 nm^2). (g) Corresponding plots of current signals during the manipulation. (h) Scheme of the rolling mechanism. Step (1) is the tip approach towards the molecule, step (2) is a 120° rotation of a wheel around its molecular axle and in step (3) the tip reaches the other side of the molecule. It shows that, in principle, only one rotation of a wheel can be induced. Reprinted from ref. 28, with permission from Nature Publishing Group, copyright 2007.

The molecular motors are adsorbed flat on the surface. Its axis of rotation is therefore perpendicular to the surface and such a rotor cannot be mounted on a board to enable the motion of a molecular machine. For running of a molecular nanovehicle on a surface, the rolling of a molecular wheel across

the surface with its axis parallel to the surface is required. Grill et al. demonstrated the rolling of a single molecular wheel with STM tip.[28] The structure of the wheel-dimer molecule is shown in Figure 1.9a, where two triptycene wheels are connected by a C≡C–C≡C axle. When adsorbed on a metal surface, this molecule exhibits two intramolecular degrees of freedom: the independent rotation of each wheel around the central axle. For a rolling motion, the Cu(110) surface was chosen because it exhibits an anisotropic corrugation due to its close-packed rows of copper atoms along the [-110] direction. The wheel-dimer molecules can adsorb in various orientations (Figure 1.9b); in particular for the orientation A, the molecular axle is parallel to the close-packed copper row, as shown in Figure 1.9c and 1.9d. Figure 1.9e and 1.9f show respectively the STM images before and after the manipulation. It is found that one wheel moves and the other remains in its initial position. The manipulation signal has a hat-shaped signal, which exhibits one intense peak at the centre and smaller maxima on both sides (Figure 1.9g). This corresponds to a 120° rotation of the left wheel of the molecule, as shown in the scheme of the rolling mechanism in Figure 1.9h. The rolling mode can only be observed for molecules in orientation A on Cu(110); for manipulation of molecules in other orientations on Cu(110) or molecules in orientation A on Cu(100), no rolling signals has been recorded. Owing to the chemical structure of the wheel, a rolling motion occurs only if the molecule is manipulated perpendicular to its axle and along a surface direction of sufficient

corrugation.

1.1.2.2 Molecular Switching

With STM, various molecular switches supported on surfaces can be studied at the single molecule level. In this section, we review the STM induced single molecule switches operated by different mechanisms, including conformation switching, spin switching, charge switching and bond switching.

Conformation Switching

Most molecular switches operate by changing conformations.[42-47,54-57,59-62,67-71] A conformational switch is defined as a switchable molecule, which has isomers with a different three-dimensional (3D) structure. The switch may take place in the 3D molecular conformation, without a modification of the bond structure. This is called stereoisomerization.[108] Wang et al have demonstrated the control of a single molecular switch by pushing and pulling a Sn ion through an adsorbed tin phthalocyanine (SnPc) on Ag(111).[46] As shown in Figure 1.10a and 1.10b, SnPc can adopt two conformations on Ag(111). In one conformation the Sn atom points toward the vacuum; while in the other conformation, the Sn atom points toward the surface. Molecules directly adsorbed on the metal surface can be transformed irreversibly from the Sn-up to the Sn-down conformation by applying a negative sample voltage (Figure 1.10c and 1.10d). The reversible switching

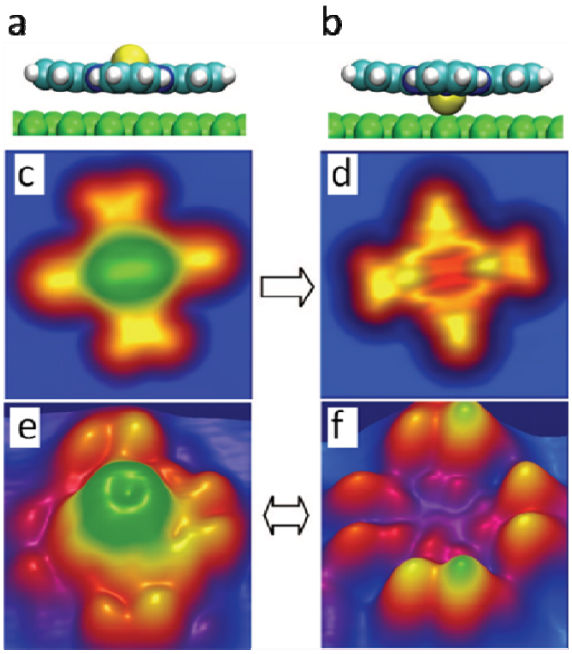

Figure 1.10 (a) Side views of Sn-up and (b) Sn-down molecules with fully relaxed adsorption geometry. (c) and (d) Pseudo-three-dimensional presentation of constant-current STM images of Sn-up (2.0 × 2.0 nm^2, V_{sample} = -0.2 V, I = 0.05 nA) and Sn-down (2.0 × 2.0 nm^2, V_{sample} = -0.05 V, I = 0.05 nA) molecules adsorbed on Ag(111). (e) and (f) STM images of Sn-up (2.0 × 2.0 nm^2, V_{sample} = -0.9 V, I = 0.2 nA) and Sn-down (2.0 × 2.0 nm^2, V_{sample} = -1.8 V, I = 0.2 nA) molecules adsorbed on a single SnPc layer. The single arrow between (c) and (d) illustrates the irreversible switching from Sn-up to Sn-down conformations, while the double arrow between (e) and (f) illustrates the reversible switching. Reprinted from ref. 46, with permission from the American Chemical Society, copyright 2009.

between Sn-up and Sn-down can only be achieved on the second layer SnPc, as shown in Figure 1.10e and 1.10f. Through the combination of the experimental observations and the calculated results, they proposed that the transition from Sn-up to Sn-down is achieved via hole attachment. The resonant tunneling out of the highest occupied molecular orbital (HOMO)-1 of Sn^{2+} creates a transiently oxidized Sn^{3+}, which is smaller than Sn^{2+}. The applied pulse voltage provides energy to move the Sn^{3+} further to the substrate surface. The most likely mechanism leading to the Sn-down to Sn-up

switching is the excitation of intramolecular vibrations. This switching is induced by the positive sample bias. The resonant transfer of tunneling electrons to the lowest unoccupied molecular orbital (LUMO)+1 gives rise to a negatively charged and thus transiently reduced molecule. Upon leaving the molecule the electron may deposit energy to vibrational degrees of freedom of the molecule and thus excite the switching process.

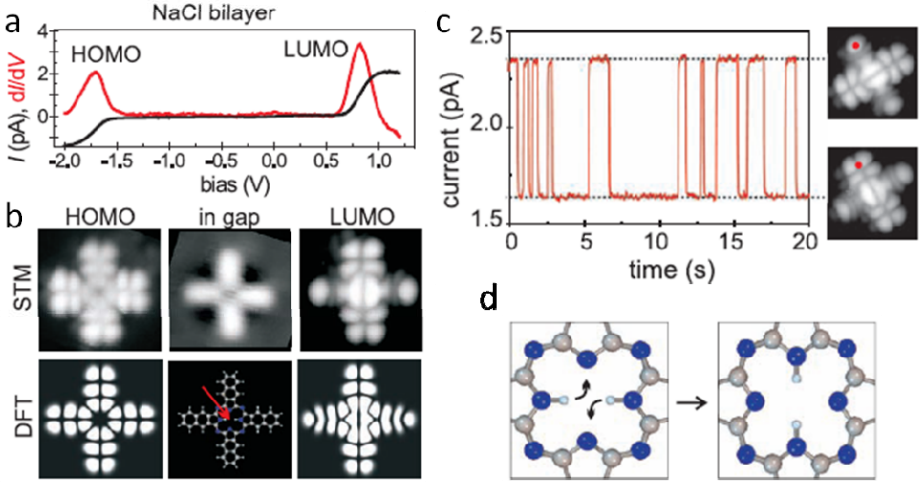

Figure 1.11 (a) Spectroscopy of naphthalocyanine on a NaCl bilayer on Cu(111) where the peaks correspond to tunneling into the LUMO (positive bias) and out of the HOMO (negative bias). (b) STM images at V_{sample} = -1.6 V, I = 1 pA (left) and V_{sample} = 0.65 V, I = 1pA, as well as at low bias (V_{sample} = 0.05 V, I = 1pA) compared with the calculated HOMO and LUMO of the free molecule. The lower center panel shows the structure model to scale where the arrow indicated the central hydrogen atoms that are along the horizontal arms. The STM images were obtained with a molecule terminated tip. Reprinted from ref. 43, with permission from the American Association for the Advancement of Science, copyright 2007.

The isomerization may also take place by a reshuffling of the intermolecular chemical bonds, which is referred to as structural isomerization. An elegant example of structural isomerization is the current-induced hydrogen tautomerization of naphthalocyanine molecule, which has been

demonstrated by Liljeroth et al.[43] Figure 1.11a shows the dI/dV spectra acquired on an isolated naphthalocyanine molecule adsorbed on NaCl(100) bilayer on Cu(111). The corresponding STM images and DFT simulated images of the HOMO, LUMO and in gap orbitals are shown in Figure 1.11b. It is found that the LUMO image allows for easy determination of the position of the inner hydrogens. The arms with hydrogens show a single-lobe structure at the end, as opposed to the nodal plane along the other two arms. The hydrogen taumerization can be induced by positioning the tip above the molecule and substantially increasing the bias above the LUMO resonance. The reaction can be directly monitored in the current signal. During the measurement, the tunneling current switches back and forth between two well defined levels, as shown in Figure 1.11c. When lower the bias and image the LUMO at resonance, they found that the two current levels correspond to a 90° rotation of the LUMO. This observation can be assigned to changes in the position of the imino hydrogens in the central cavity. The dependence of the switching rate on the current is linear. This indicates that the switching is caused by a one-electron process.

Spin Switching

A new field of molecular spintronics is emerging that combines the ideas and advantages of spintronics and molecular electronics.[37] A fundamental link between these two fields can be established by using molecular magnetic materials, in particular, single-molecule magnets (SMM).[31] SMM have been

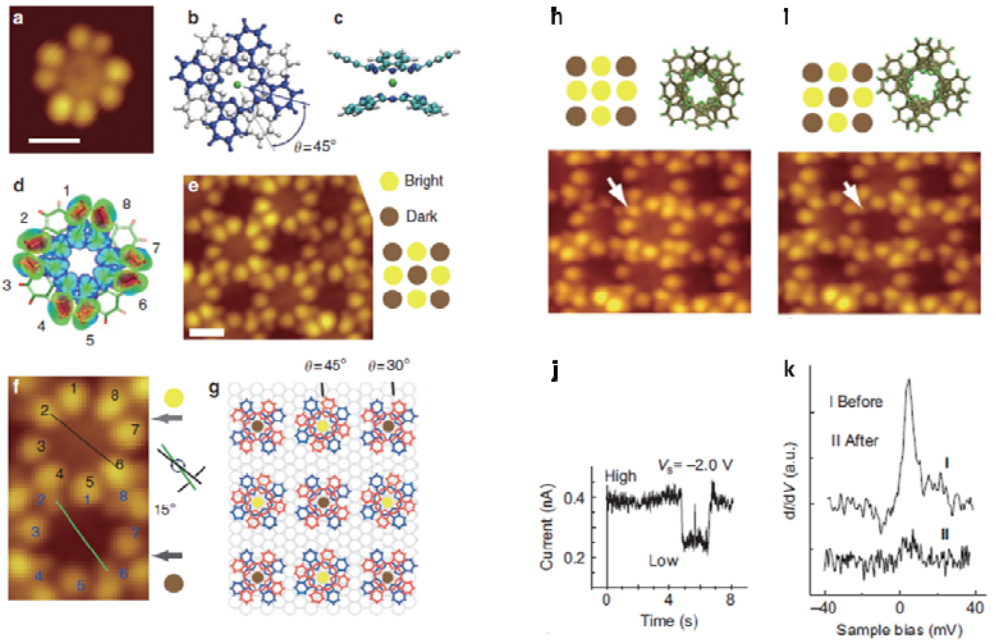

Figure 1.12 (a) STM image of an isolated molecule of $TbPc_2$ on Au(111). (b) A schematic model of the double-decker $TbPc_2$ molecule. The upper (lower) Pc is coloured in blue (silver). (c) Side view of the $TbPc_2$ molecule after structural optimization by using DFT calculations. (d) A simulated STM image of the $TbPc_2$ molecule by DFT calculations. (e) Film of $TbPc_2$. An alternating contrast pattern of nine molecules is shown on the right hand side with brighter molecules in yellow and darker molecules in brown. (STM images of a and e were obtained with V_{sample} = -0.8 V and I = 0.3 nA. Bars correspond to 1nm). (f) A magnified image of bright (upper) and dark (lower) molecules. The black (green) line connects lobes 2 and 6 of bright and dark molecules. The two lines are rotated 15° with respect to each other. (g) A tentative model of the adsorption configuration of $TbPc_2$ film, corresponding to the image in e. Bright (θ = 45°) and dark (θ = 30°) molecules form a pseudo-square lattice, and the red and blue Pc ligands correspond to vacuum- and substrate-side Pc ligands, respectively. (h) and (i) Conversion of the centre molecule from bright (θ = 45°) to dark (θ = 30°) by applying a current pulse. The target molecule is marked by an arrow. Change in the contrast and the top view of the centre molecule are schematically illustrated. (j) Current during a -2.0 V voltage pluse over a $TbPc_2$ molecule initially in the bright state. The tip remained fixed over a lobe position with the feedback loop open. Each jump in the current indicates the moment of rotation of the molecule and low state corresponds to the dark state. (e) Comparison of the Kondo peaks before I and after II the application of the pulse. Reprinted from ref. 113, with permission from Nature Publishing Group, copyright 2011.

intensively investigated for their rich quantum behavior, such as quantum tunneling of magnetization,[109] quantum phase interference,[110] Kondo effect[30]

and Zeeman splitting of the Coulomb-blockade peaks.[111] Due to the presence of large spin and high anisotropy barrier, SMM in a time-dependent magnetic field are shown to exhibit magnetic hysteresis loops.[112] This opens the exciting perspective of exploiting spins to store and process information, made even more appealing owing to their rich quantum behavior.

Using double-decker bis(phthalocyaninato) terbium (III) complex ($TbPc_2$) as a SMM, Komeda et al. showed that the molecular spin can be switched on and off by applying an electric current via a STM.[113] The switching is manifested through the disappearance and reappearance of the Kondo resonance. The Kondo effect arises from the coupling between a localized electron spin and a sea of conduction electrons. Figure 1.12a shows an STM image of an isolated $TbPc_2$ adsorbed on Au(111). Figure 1.12b and 1.12c are the schematic models of the top view and side view of $TbPc_2$. Two Pc ligands sandwich a Tb ion with an azimuthal rotational angle of 45°. Simulated STM image of the $TbPc_2$ molecule on Au(111) is shown in Figure 1.12d, and indicates that the eight protrusions in the STM images are from the upper Pc ligand. $TbPc_2$ in a monolayer film forms a checkerboard contrast pattern, as depicted on the right hand side of Figure 1.12e. The bright and dark molecules are shown in yellow and brown, respectively. Magnified image in Figure 1.12f reveals that upper Pc ligand of the bright and dark molecules are rotated by 15° with respect to each other. The bright and dark molecules can be switched between each other by injecting enough current via the STM tip. Figure 1.12h

and 1.12i show STM images, in which the centre molecule is converted from bright to dark by applying a pulse V_{sample} to the molecule. Rotation of a molecule can be monitored by the tunneling current change, as shown in Figure 1.12j; the high and low states of the tunneling current correspond to bright and dark state respectively. The log-log plot of the rotation rate versus the tunneling current yields a slope of ~1.09, which suggests that the current-induced rotation is an one-electron process. Figure 1.12k shows the analysis of tunneling conductance (dI/dV) on a $TbPc_2$ molecule. A clear Kondo resonance is observed when the tip is positioned over one of the lobes of the bright molecule. However, the Kondo feature disappears for the dark molecule. Moreover, when the tip is placed over the center of the bright or dark molecules, no Kondo feature can be observed. This indicates that an unpaired electron in a π orbital of the upper Pc ligand of the bright molecule is responsible for the appearance of the Kondo peak. DFT calculations shows that upon the rotation of the upper Pc ligand from 45°, the singly occupied molecular orbital (SOMO) will shift toward the Fermi energy. Hence, in the presence of the Au(111) surface, the SOMO became doubly occupied near θ = 30° due to charge transfer from the surface, quenching the molecular spin and the Kondo state. The controlled on and off switching of a molecular spin makes it possible to code information at the single-molecule level.

Charge Switching

Molecular charge switching requires bistability of the charge states of the molecule. This can be achieved if (i) the lifetime of the tunneling electron on the molecule is sufficiently long and (ii) there is a mechanism that stabilizes the extra charge on the molecule.[53, 72, 114] If the atom is directly adsorbed on a metal surface, the strong coupling between them will prevent the permanent charging of the atom. However, if the molecule is adsorbed on an ultrathin insulating film, the life time of the electron on the molecule can be considerably increased, which leads to the stable charging state.

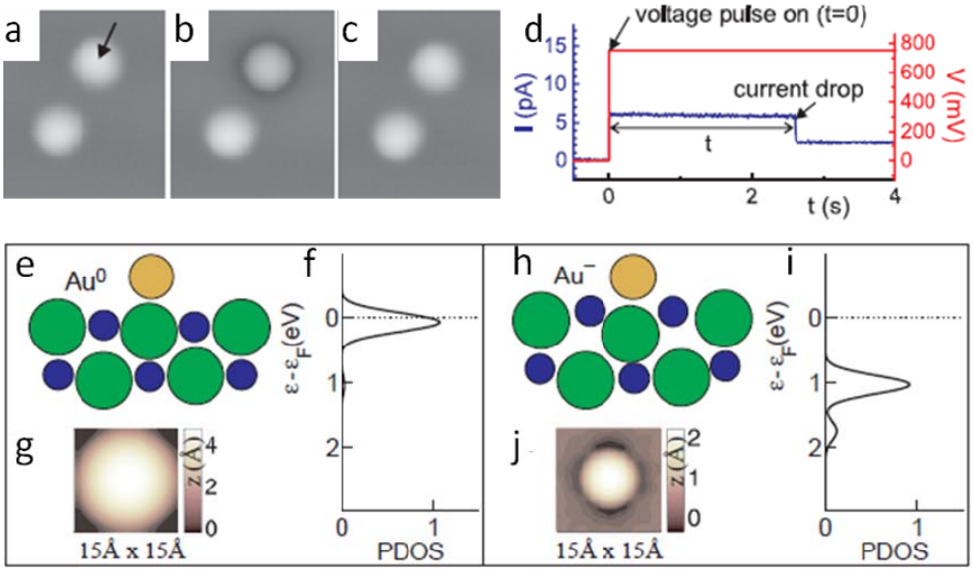

Figure 1.13 (a) STM image of Au adatom on NaCl/Cu(111). After recording the image (a), the STM tip was positioned above one of the Au adatom (arrow) and a positive voltage pluse was applied to the sample. After a time t, a sharp decrease in the tunneling current can be observed in (d). A subsequent STM image (b) shows that the manipulated Au adatom has a different appearance but did not change its position. By applying a negatibe voltage pulse, one can switch the manipulated adatom back to its initial state (c). (e)-(g) Calculated electronic and geometric properties of the neutral and (h)-(j) negatively charged Au adatom. The ion-core positions are represented by a sphere model (e and h), in which the spheres representing Au, Cl^-, and Na^+ are clolored gold, green, and blue, respectively. The calculated partial density of states (PDOS) of s-states at the Au adatom (f and i). the 6s-derived state is partially and fully

occupied in (f) and (j). STM images are simulated by contours of constant LDOS (g and j), where z = 0 Å corresponds to a distance of 6.4 Å from the topmost NaCl reference plane. Reprinted from ref. 53, with permission from the American Association for the Advancement of Science, copyright 2004.

Repp et al. showed that individual gold atoms on an ultrathin insulating NaCl film supported by a copper surface can exhibit two different charge states.[53] As shown in Figure 1.13a, individual Au atoms on NaCl(100)/Cu(111) are imaged as protrusions. By applying a positive 0.6 V to the sample and monitoring the current, a sharp decrease in the tunneling current can be observed (Figure 1.13d). Subsequent STM image in Figure 1.13b shows that the manipulated Au adatom has changed to a sombrero-like shape. By applying a negative voltage pulse to the sample, the Au adatom can be switched back to its initial state, as shown in Figure 1.13c. The two different states before and after manipulation are assigned to the neutral and negatively charged state, respectively. This assignment is further confirmed by the DFT calculations. As shown from Figure 1.13e-1.13j, for the Au^0 adatom, a weak bond is formed with a binding energy of 0.4 eV. It is adsorbed about 3.2 Å above the Cl^- ion and leaves the ionic positions within the NaCl film relatively unperturbed. However, the position of the Au^- adatom is 0.4 Å closer to the surface, and is stabilized by large ionic relaxations within the NaCl film. The Cl^- ion underneath the adatom is forced to move downward by 0.6 Å and the surrounding Na^+ ions to move upward by 0.6 Å. This relaxation pattern creates an attractive potential for the additional charge on the Au adatom. The additional charge is further stabilized by the screening charge in the metal

substrate and by the electronic polarization of the ionic layer. Statistical analysis of the switching behavior of Au adatoms suggests that the switching between two charge states is attributed to inelastic electron tunneling.

Bonding Switching

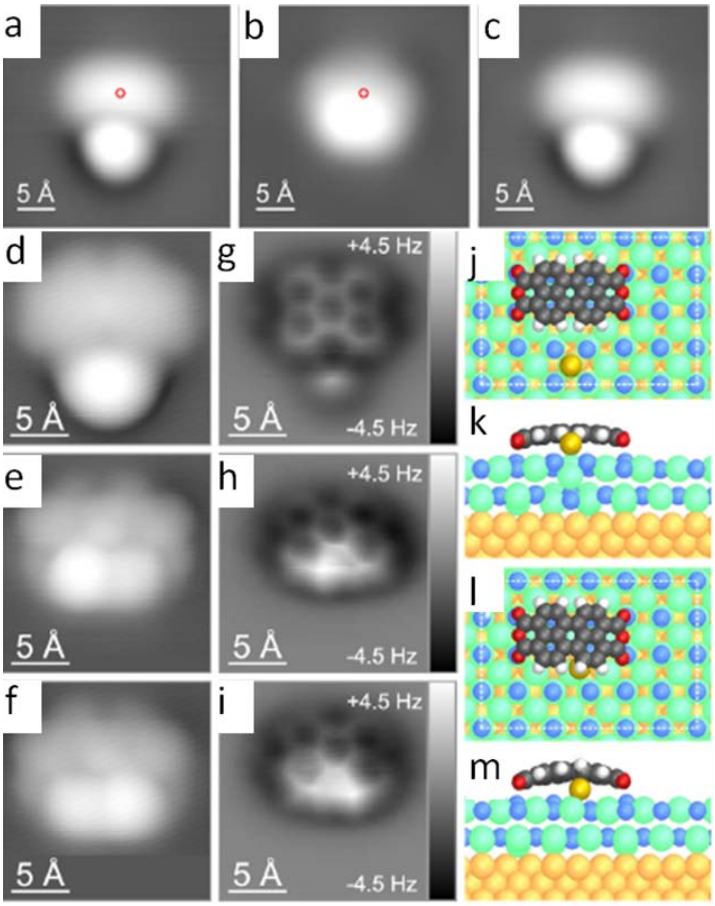

Figure 1.14 (a) Au- adatom in close proximity of a Au-PTCDA complex. With the tip at the position indicated by the (red) circle, the sample bias voltage V was ramped to -1.5 V. A sudden increase in the tunneling current I indicated a successful modification of the complex. (b) In the subsequent STM image, the adatom and the molecule no longer appeared separated. By ramping the voltage to +1.5 V, the complex was switched back to the initial state, as confirmed by the subsequent image (c). Imaging parameters: V_{sample} = 0.2 V, I = 5 pA. (d)-(f) STM images of Au-PTCDA in the nonbonded (a) and the bonded [(b), (c)] configuration (imaging parameters: V_{sample} = 0.2 V, I = 3 pA). The tip had been terminated with a CO molecule. (g)-(i) Corresponding constant-height AFM images (imaging parameter: amplitude A = 0.4 Å, frequency f = 23, 165 Hz and distance with respect to the STM set point above the substrate between +0.8 Å and +1.0 Å). (j)-(m) DFT-calculated geometries of the complex in the nonbonded [(j), (k)] and the bonded [(l), (m)] state. The

unit cell used for the calculations is indicated in (j) and (l), and the different atomic species are colored in gray (C), red (O), white (H), green (Cl), blue (Na), orange (Cu), and yellow (Au). Reprinted from ref. 52, with permission from the American Physical Society, copyright 2010.

Due to its capabilities to image and manipulate adsorbates on the atomic scale, STM is also possible for the basic chemical reaction studies, such as dissociation, diffusion, adsorption, desorption and bond-formation processes.[85] Complex mechanisms are involved when forming a bond between two adsorbed molecular fragments on a surface. To form a bond between them, the electronic wave functions of their reactive parts need to overlap significantly. Hence, they have to be in close proximity on the surface and their reactive parts must align properly. Mohn et al. have presented a molecular switch that is based on the reversible bond formation between a Au adatom and an organic admolecule [perylene-3,4,9,10-tetracarboxylic dianhydride (PTCDA)] on a thin NaCl film supported by a Cu substrate.[52] The reversible switching of a Au-PTCDA complex on NaCl(2ML)/Cu(111) is shown in Figure 1.14a-1.14c. At the beginning, a Au^- adatom is brought in close proximity of a $PTCDA^-$ adamolecule (Figure 1.14a). Then the sample bias is ramped to -1.5V. Subsequent STM image shows that the complex has been switched to a different state (Figure 1.14b). By ramping the bias voltage to +1.5V, the complex can be switched back to the initial state (Figure 1.14c). They referred to the different states of the complex as the nonbonded [Au-PTCDA(N)] and bonded [Au-PTCDA(B)]. To determine the atomic structure of the different configurations of Au-PTCDA, atomically resolved AFM molecular imaging

was used. As shown in Figure 1.14g-1.14i, the perylene core of the PTCDA is clearly resolved in the AFM images. For Au-PTCDA(N), the AFM image shows that the molecule and the Au adatom are clearly separated. While for the Au-PTCDA(B), the Au atom is no longer separated from the molecule and the brightness of the lower part of the atom-molecule complex is enhanced. A distinct enhancement of the brightness is observed above one of the two inner C sites at the lower edge of the molecule, and the two mirrored configurations can be clearly distinguished. The experimental results are corroborated by DFT calculations, as shown in the calculated atomic structures of the complex in Figure 1.14j and 1.14k. A more detailed calculation of the PDOS reveals that a covalent bond is formed between Au adatom and PTCDA for Au-PTCDA(B).

1.2 Molecular Self-assembly on Surfaces

In the above section, we introduce a variety of external stimuli and mechanisms that are responsible for the operation of molecular switches. However, for practical applications, incorporation of these molecular switches into more complex and rationally designed nanostructure is needed. Self-assembly represents a promising bottom up approach to fabricate well-defined molecular architectures at surfaces. In this section, we will give a brief introduction of various self-assembled molecular nanostructures on surfaces as well as the effect of molecule-substrate interfacial interactions and intermolecular interactions.

1.2.1 Introduction of Self-assembled Molecular Nanostructures on Surfaces

Supramolecular self-assembly, which is described as " the spontaneous association of either a few or many components resulting in the generation of either discrete oligomolecular supermolecules or of extended polymolecular assemblies such as molecular layers" ,[115] represents a promising bottom up approaches to fabricate well defined molecular architectures at surfaces. The ability to fabricate large area periodic molecular arrays opens up potential applications in the fields of organic[116, 117] and molecular electronics,[118-121] and biosensors.[122-124]

Various intermolecular interactions, including strong covalent bonding,[125-130] directional and selective non-covalent interactions such as hydrogen bonding [131-170] and metal-ligand coordination,[171-184] as well as weak van der Waals,[162, 185-197] dipole-dipole[198, 199] and donor-acceptor interactions[200-204] have been widely exploited for the assembly of molecules on surfaces. By rational design and selection of molecular building blocks, a large variety of molecular arrays with desired functionality can be realized, such as isolate molecules,[174, 177]clusters,[199] one-dimensional (1D) supramolecular nanogratings or chains,[128, 131, 132, 136, 142, 146, 147, 149, 153, 199] two-dimensional (2D) honeycomb networks, [133, 135, 138-140, 143, 144, 150, 152, 155, 161, 162, 165, 184-186, 188-194] rectangular coordination networks,[171, 172, 175, 176, 178-180, 183] kagomé networks,[160, 185, 190, 191, 195, 197, 205] tetragonal cavities,[157-159] nanomesh[200] as well as more

complex multi-component arrangements. [151, 166, 182, 196, 201-204, 206-209] Elegant examples are surface covalent organic frameworks (SCOF) including dimers, long linear chains and 2D networks formed by covalently bonded bromophenyl porphyrin (Br_xTPP) with one, two or four Br substituents on Au(111);[128] 2D open honeycomb network on Ag-passivated Si(111) substrates stabilized by triple hydrogen bonding between melamine and perylene tetra-carboxylic di-imide (PTCDI);[135] 2D rectangular metal-organic coordination networks (MOCNs) with tailored pore size and functionality by the modular assembly of polytopic organic carboxylate linker molecules and iron atoms on Cu(100) surface; [173, 190] 2D linear, honeycomb as well as kagomé porous networks of dehydrobenzo annulene (DBA) derivatives at the 1,2,4-trichlorobenzene (TCB)/graphite liquid-solid interface based on van der Waals interactions between interdigitating alkyl chains;[190] well-ordered organic donor/acceptor nanojunction arrays comprising p-sexiphenyl (6P) and C_{60} via self-assembly of C_{60} on the molecular nanotemplate of 6P nanostripes on Ag(111).[202]

1D or 2D highly periodic supramolecular assemblies can also be used as nanoscale templates. Surface nanotemplate-assisted molecular assembly represents another promising route toward the construction of addressable functional molecular architectures. An effective surface nanotemplate usually

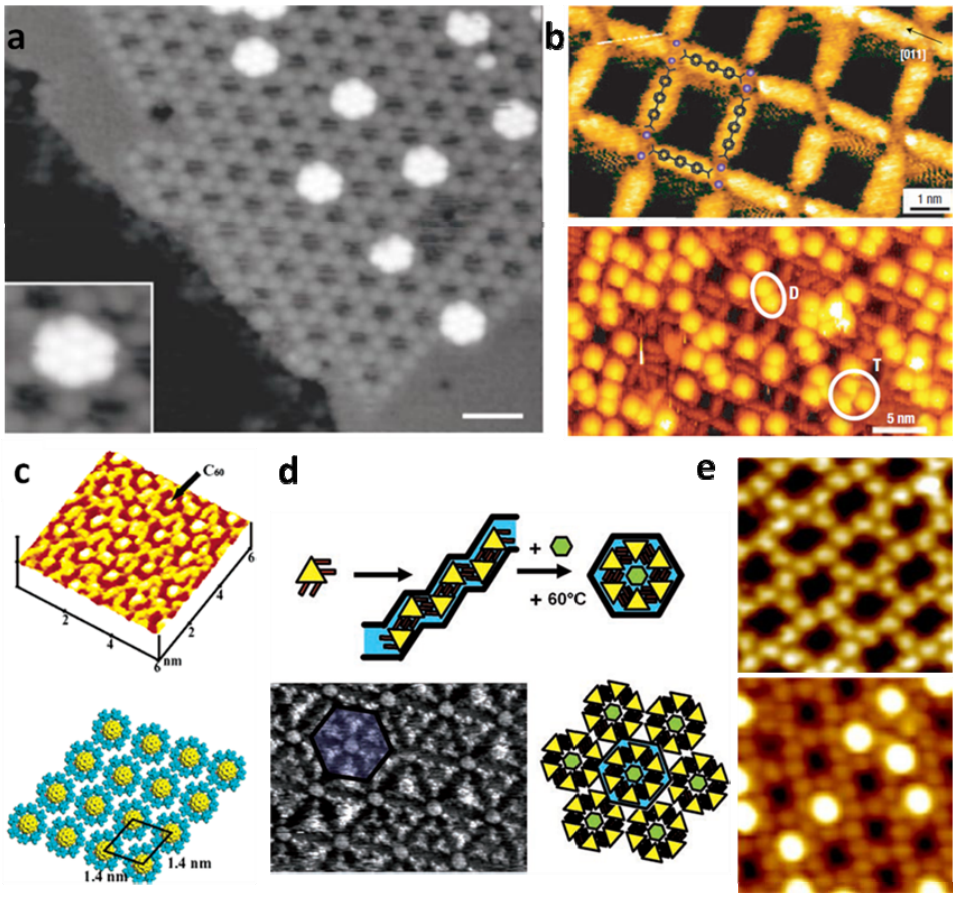

Figure 1.15 Various molecular networks on surfaces as well as the corresponding host-guest aggregates. (a) STM image (V_{sample} = -2 V, I = 0.1 nA) of C_{60} heptamers on a PTCDI-melamine network. Inset, high-resolution view showing an individual cluster. Scale bar,5 nm;[135] (b) High-resolution image of 2D reticulated Fe-TDA open network with rectangular nanocavities on Cu(100) substrate, positioning of molecular backbone and ligands are marked, Fe atoms are shown as blue spheres (up), scale bar 1nm; the cavities in Fe-TDA networks can host C_{60} monomers, dimmers or trimers, scale bar 5 nm;[173] (c) height-shaded surface plot of a high-resolution STM image (6 × 6 nm^2) of C_{60}/OBOCMC8 adlayer on Au(111) (top) and the proposed structural model (bottom);[206] (d) scheme of the rearrangement reaction illustrating dynamic constitutional diversity of the self-assembled entities formed by bifunctional molecules with a 2,4,6-tristyrylpyridine core(top), STM image (25.7 × 18.7 nm^2) after rearrangement induced by addition of hexabenzocoronene (bottom left) and scheme of the obtained hierarchical structure (bottom right);[189] (e) STM images (9 × 9 nm^2 for the upper panel) showing the preferential trapping of individual C_{60} molecules into the nanocavities of the C_{60} nanomesh.[200](a) Reprinted from ref. 134, with permission from Nature Publishing Group, Copyright 2003; (b) Reprinted from ref. 172, with permission from Nature Publishing Group, Copyright 2004; (c) Reprinted from ref. 205, with permission from American Chemical Society, Copyright 2006; (d) Reprinted from ref. 188, with permission from

WILEY-VCH Verlag GmbH & Co. KGaA, Copyright 2007; (e) Reprinted from ref. 199, with permission from American Chemical Society, Copyright 2008.

features prepatterned and well ordered preferential adsorption sites that can selectively accommodate guest adsorbates. Surface confined 2D molecular networks, especially those with void spaces, or the so called "2D porous networks", can serve as templates to selectively accommodate molecules to form molecular arrays with periodicity matching the underlying nanotemplates. Examples include C_{60} heptamers trapped within the pores of the honeycomb network stabilized by triple hydrogen bonding between PTCDI and melamine (Figure 1.15a);[135] C_{60} monomers, dimers or trimers trapped in 2D reticulated nanocavities of MOCNs with tunable size and topology as illustrated in Figure 1.15b;[173] C_{60} included in the adlayer of a calix[8] arene derivative ($C_{104}H_{128}O_{24}$) OBOCMC8 on the Au(111) surface (Figure 1.15c);[206] structural transformation of DBA molecular networks from a linear nonporous structure to a honeycomb porous network in response to the addition of guest coronene molecules as shown in Figure 1.15d;[188, 189] ordered 2D C_{60} arrays adsorbed atop the C_{60} nanomesh template (Figure 1.15e).[200]

By rational design and selection of molecular building blocks with desired functionalities, the ordered 2D molecular nanostructrues can have a broad range of applications. The 2D nanoporous networks[115, 210] with a tunable cavity size and periodicity can be used to immobilize and isolate the guest molecules in a repetitive and spatially ordered manner, which enables

addressing them *in-situ* at the single molecule scale. It is found that these nanopores could act as confined reaction vessels for the template synthesis of inorganic and organic nanoparticles.[211, 212] These extended 2D networks can even be homochiral on the entire surface, with potential applications in asymmetric heterogeneous catalysis and chiral separation.[213] Extended 2D open network structures can be fabricated via a number of different approaches. One example is the MOCNs. The incorporation of metal centers increases the functional properties of the nanostructures and facilitates their uses in heterogeneous catalysis,[214-221] molecular recognition and gas storage,[222-228] chemical separations,[214, 229] sensing[230] and molecular magnetism.[231-233] These self-assembled molecular nanostructures show the great potential in high density information storage, based on the successful demonstration of reversible switching of single dipole molecule between two different dipole configurations,[234-236] controlling the spin state of a single-molecule magnet,[31, 113, 237] trans-cis isomerization of the azobenzene molecules,[45, 62, 238] and so on.

1.2.2 Effect of Molecule-Substrate Interfacial Interactions and Intermolecular Interactions on Molecular Self-assembly on Surfaces

The controlled positioning and assembly of functional molecules into ordered structures on surfaces depends on the interplay of multiple interactions on different strengths and length scales.[210, 239-250] The arrangement of molecules on surfaces is governed by a combination of molecule-substrate

interactions and intermolecular interactions. A subtle balance of these interactions can lead to the formation of well-defined supramolecular architectures over macroscopic areas. Supported surfaces play a critical role in guiding the molecular self-assembly process. Depending on their reactivity and electronic properties, chemisorption or physisorption of the adsorbate molecule may occur.

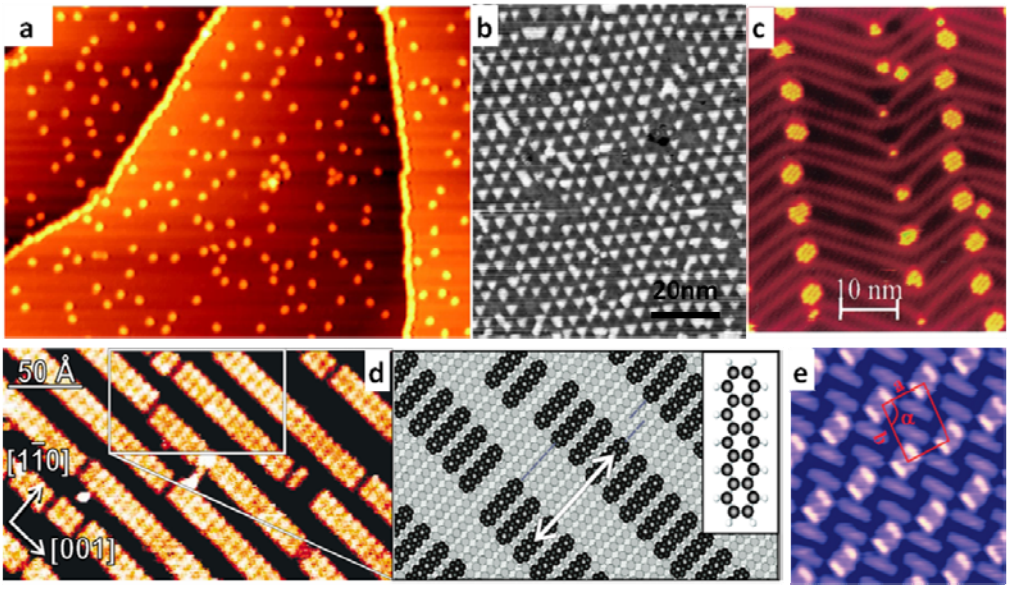

Figure 1.16 Molecular nanostructure arrays formed on metal surfaces. (a) STM image (65 × 100nm^2) of randomly distributed Ir(ppy)$_3$ molecules on Cu(111) obtained at 81K (V_{sample} = 0.6 V, I = 80 pA);[251] (b) STM image of a periodic array of Fe islands nucleated on the dislocation network of Cu bilayer on Pt(111) at 250 K, scale bar 20 nm;[252] (c) 0.1ML 1-nitronaphthalene (NN) adsorbed on a reconstructed Au(111) surface, scale bar 10nm;[253] (d) high-resolution STM image (V = 2 V, I = 0.5 nA) showing the molecular stripes of pentacene on the Cu(110) surface, the molecular stripes running along the [001] direction are separated by 28±2 Å (white arrow) as shown schematically at the right side together with a stick and ball model of pentacene, scale bar 50 Å; [254] (e) molecular resolved image of highly ordered pentacene:PTCDA 2D network with R-chirality on Ag(111) (8 × 8 nm^2).[255](a) Reprinted from ref. 251, with permission from American Physical Society, Copyright 2007; (b) Reprinted from ref. 252, with permission from Nature Publishing Group, Copyright 1998; (c) Reprinted from ref. 264, with permission from American Physical Society, Copyright 1999; (d) Reprinted from ref. 254, with permission from American Physical Society, Copyright

2001; (e) Reprinted from ref. 255, with permission from American Chemical Society, Copyright 2008.

For the case of adsorption on metal surfaces, molecular self-assembly can be mediated by the substrate in different ways, such as:

(i) Substrate mediated intermolecular electrostatic repulsion.[251, 256-260] Examples include the formation of highly dispersed superstructures of a dipolar iridium complex on Cu(111) stabilized by the strong and long-range repulsive intermolecular dipole-dipole interactions as shown in Figure 1.16a,[251] and the spontaneous formation of a superlattice of TTF molecules on Au(111) stabilized through the charge transfer induced electrostatic repulsion between molecules;[256]

(ii) Elastic deformation of the substrate induced long-range interactions between adsorbates.[252, 261-263] Examples include a periodic array of Fe islands nucleated on the strain relief pattern of a Cu bilayer on Pt(111) (Figure 1.16b);[252] C_{60} nanostructure arrays on the highly regular mesh of boron nitride on a Rh(111) single crystalline surface;[262]

(iii) Adsorption on the preferential binding sites of the substrate.[199, 253, 264-267] Examples are the use of surface reconstructions[199, 264] (see Figure 1.16c) or step bunching on vicinal surface,[253, 265-267] where the 2D islands preferentially nucleate at the higher binding energy sites;

(iv) 2D surface-state electrons mediated long-range oscillatory interactions between adsorbates.[254, 268-272] For example, the charge-density waves on Cu(110) can effectively modulate the substrate-adsorbate

interactions and hence result in the formation of unidirectional rows of pentacene on Cu(110)[254] (Figure 1.16d);

(v) Epitaxial interlocking of the molecule with the substrate.[255, 257-260] The relatively strong molecule-substrate interaction can constrain the molecules to adsorb in registry with the surface periodicity and locks them into specific adsorption sites, examples include the quasi-epitaxial interlocking of PTCDA and pentacene molecules with Ag(111) (Figure 1.16e).[255]

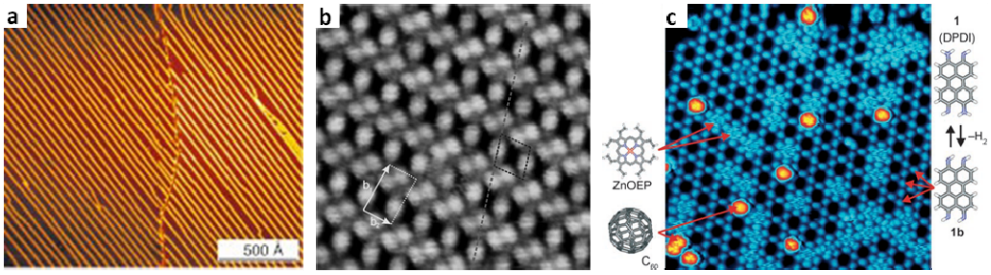

Figure 1.17 Hydrogen-bonded molecular nanostructures. (a) STM image showing the formation of a one-dimensional supramolecular PVBA nanograting on Ag(111) surface with a single domain extending over two terraces, scale bar 500 Å;[131] (b) higher resolution STM image (17.5 × 17.5 nm^2) showing the molecular arrangement of a parallelogram network formed by PTCDI and melamine on Au(111);[141] (c) STM image (30 × 30 nm^2,V = -1.7 V, I = 12 pA, T = 77 K) of C_{60} and ZnOEP molecules trapped in the pores of the dehydro-DPDI honeycomb network. The chemical structures are assigned to the molecular units by arrows.[150](a) Reprinted from ref. 130, with permission from WILEY-VCH Verlag GmbH & Co. KGaA, Copyright 2000; (b) Reprinted from ref. 140, with permission from WILEY-VCH Verlag GmbH & Co. KGaA, Copyright 2007; (c) Reprinted from ref. 149, with permission from WILEY-VCH Verlag GmbH & Co. KGaA, Copyright 2007.

Lateral intermolecular interactions also play an essential role in determining the supramolecular self-assembly processes on surfaces. The van der Waals force universally exists in every material system, but it is rather weak and non-directional. The creation of covalent bonded networks relies on the polymerization reactions of deposited molecules; they show higher

stability but are more difficult to control.[125-130] Directional and selective hydrogen bonds, which are intermediate strength (5-70 kJ/mol) relative to strong covalent bonding (>300 kJ/mol) and weak van der Waals forces (2-10 kJ/mol),[273, 274] represent a versatile and widely employed method to direct the assembly of molecular building blocks into supramolecular systems with appreciable thermal stability. The properties of the resulting supramolecular architectures can be tailored by modifying the functionality and structure of the molecular building blocks as well as the molecular ratio. A large number of different hydrogen-bonded single-component, binary or multicomponent supramolecular assemblies on surfaces have been realized. Elegant examples include the 1D supramolecular nanograting of 4-[trans-2-(pyrid-4-yl-vinyl)] benzoic acid (PVBA) on Ag(111);[131] 2D parallelogram network formed by PTCDI and melamine on Au(111);[141] C_{60} and zinc octaethylporphyrin (ZnOEP) molecules trapped in the pores of the dehydro-DPDI honeycomb network. [150]

1.3 Objective and Scope of This Thesis

Molecular switches on surfaces are intensely investigated because they are potential components in future molecule-based functional devices. External stimuli like light,[62, 69] electric field,[42,56] temperature,[70] and chemical stimulus[96-99] have been used in the past to induce switching in self-assembled monolayers, however, these stimuli do not provide single molecule selectivity. By contrast, STM tip can be used to perform the single molecule manipulation.

However, most of the studies are performed either individually or in a self-assembled single component monolayer. For the molecular switches to have practical applications, three essential steps are required. First, the desired function should be encoded in a single molecule. Second, the molecules should be coupled to a support substrate and wired into a rationally designed molecular matrix without suppressing their switching performance. Third, appropriate external stimuli should be applied to turn the functional molecules between on and off states with atomic precision.

Dipolar phthalocyanine molecules, which have been of great interest for controlling surface or interface properties in molecular electronic devices and tuning the energy level alignment at the interface for molecule-based devices, represent a very interesting example of a molecular switch. Its operating mechanism is based on a reversible dipole switching. As the nonplanar dipolar molecule possesses an out-of-plane electric dipole moment it adopts two distinct configurations on a surface, namely, dipole up and dipole down. Vanadyl phthalocyanine (VOPc) and chloroaluminium phthalocyanine (ClAlPc) are both nonplanar dipolar molecules, which carry electric-dipole moment of 2.27 D and 3.7 D respectively. It is therefore of interest to perform the single molecule switching on these systems. Such studies would enable us to better understand their switching mechanism and allow us to improve our control over the switching process.

Directional and selective intermolecular interactions, such as hydrogen

bonding, have been widely used to fabricate single-component, binary or multicomponent supramolecular assemblies on surfaces. By carefully selecting the molecular building blocks, the molecular switches can be isolated and immobilized in a repetitive and spatially ordered manner. Supporting surfaces also play a critical role during the single-molecule switching operation. For example, the strong interfacial coupling between the metal surface electrons and the molecule may cause the intrinsic switching properties of the molecule to disappear, or in other cases the lateral electron transport at metal surfaces may lead to nonlocal effects. To minimize the substrate effect, atomically flat and chemically inert graphite substrates are chosen for the single-molecule switching studies in this thesis.

Chapter 2 of the thesis provides an overview on the working principles of the surface analytical probes, namely STM and UPS. The experimental results are presented in Chapters 3 to 5. We begin with a investigation of C_{60}: pentacene binary system on Ag(111) to demonstrate how to construct 2D molecular nanostructure arrays on surfaces through self-assembly. In what follows, the reversible switching of single-dipole molecule within the single-component VOPc monolayer is presented, and spatially resolved scanning tunneling spectroscopy is used to identify the electronic structures of VOPc with different dipole orientation. Finally, single-dipole molecule switching is extended to binary molecular networks formed by co-assembly of ClAlPc and perfluoropentacene (PFP) on graphite, density functional theory

calculations are carried out to reveal the reasonable switching pathway.

Chapter 2: Experimental Methods

2.1 Scanning Tunneling Microscopy

In the early 1980s, Binnig, Rohrer, Gerber and Weibel at the IBM Rüschlikon laboratory succeeded in the development of STM through the successful combination of vacuum tunneling and scanning capability.[275] The first log I-s characteristics showing an exponential dependence of the tunnel current I on the tip-surface separations were obtained by using a tungsten tip and a platinum sample on 16 March, 1981. This date has subsequently been identified with the birth of the STM. However, the real breakthrough of STM came with the first atomic resolution image of the Si(111) 7 × 7 surface obtained in autumn 1982. The atomic resolution capability of STM directly in real space made STM different compared with all other surface science tools and the study of surfaces has been greatly advanced. STM has marked the beginning of a novel field of Ångström unit scale research and technology. Besides the real-space imaging, STM is also capable of resolving local electronic structure at an atomic scale as well as manipulating single atoms or molecules with atomic precision.[85, 276-280] In the following sections, I will briefly introduce the fundamental physics in STM, basic physical principles of STM as well as the applications.

2.1.1 Theoretical Treatment of 1D Tunneling

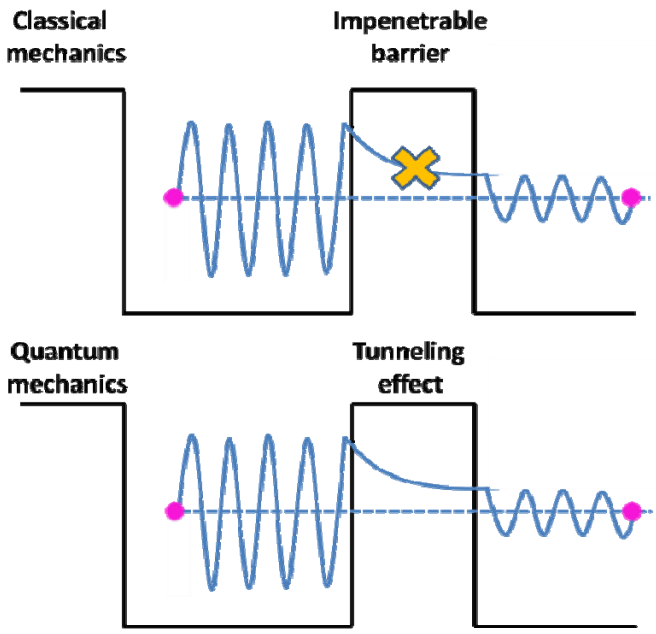

Figure 2.1 The difference between classical theory and quantum theory. In classical mechanics, a particle cannot pass through a potential barrier. In quantum mechanics, a particle has a non-zero probability of tunneling through a potential barrier.

In this section, elementary theories of tunneling through a 1D potential barrier are presented, which will provide us with an understanding of the basic physics of STM.[281] In classical mechanics, an electron in a potential $U(z)$ is described by

$$\frac{p^2}{2m}+U(z)=E \tag{2.1}$$

where m is electron mass, and E is the energy. In regions where $E>U(z)$, the electron has a non-zero momentum $p=\left[2m(E-U)\right]^{1/2}$. On the other hand, the electron cannot penetrate into any region with $E<U(z)$. In quantum mechanics, the electron is described by a wavefunction $\psi(z)$, which satisfies the Schrödinger equation,

$$-\frac{\hbar^2}{2m}\frac{d^2}{dz^2}\psi(z)+U(z)\psi(z)=E\psi(z) \tag{2.2}$$

Consider the case of a rectangular potential barrier, as shown in Figure 2.1, in the classically allowed region, $E>U$, equation 2.2 has solutions

$$\psi(z)=\psi(0)e^{\pm ikz} \tag{2.3}$$

where $k=\frac{\sqrt{2m(E-U)}}{\hbar}$ (2.4)

is the wave vector. In the classically forbidden region, equation 2.2 has a solution

$$\psi(z)=\psi(0)e^{-\kappa z} \tag{2.5}$$

Where $k=\frac{\sqrt{2m(U-E)}}{\hbar}$ (2.6)

is the decay constant. It describes an electron penetrating through the barrier into the +z direction. The probability density of observing an electron near a point z is proportional to $|\psi(0)|^2 e^{-2\kappa z}$, which has a non-zero value in the barrier region, thus has a non-zero probability penetrating a barrier.

Starting from this elementary model, we can explain some basic features of the tunneling between STM tip and sample. We consider a simplified 1D potential energy diagram for the system consisting of the tip (left electrode) and the sample (right electrode), which are separated by a small vacuum gap.[282] Here, the tip is considered to be a metal with a constant density of states; while the sample contains a distribution of surface states as shown in Figure 2.2. When the tip and the sample are far away from each other, their

vacuum levels are aligned and their Fermi levels lie below the vacuum level

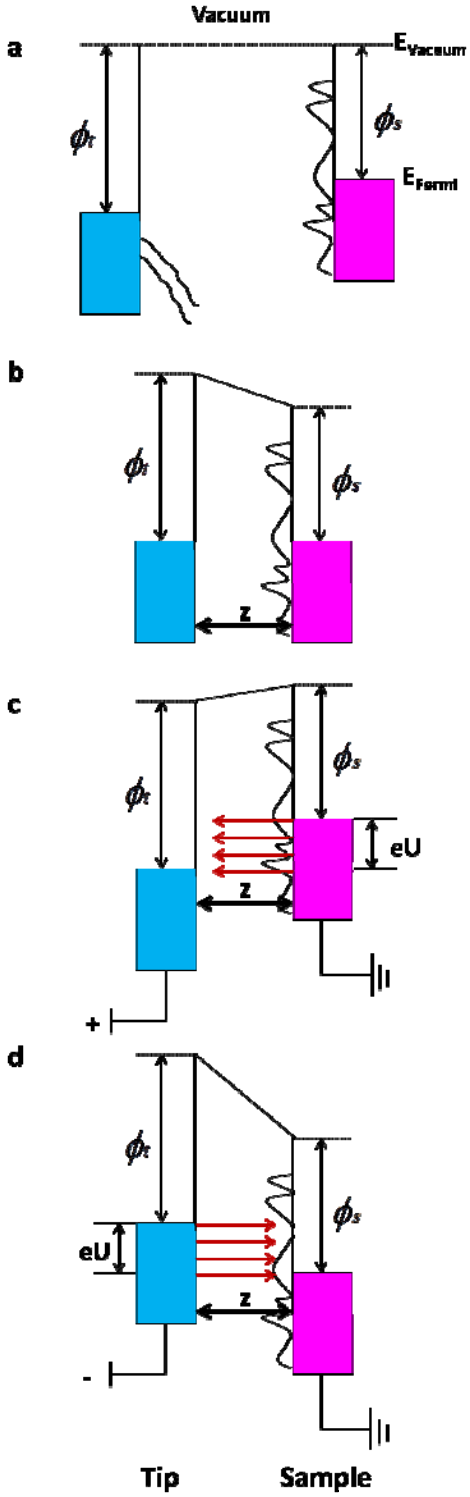

Figure 2.2 Schematic drawing of the energy level diagram for electron tunneling through a simplified 1D barrier. (a) Independent tip and sample system. (b) Tip and sample in thermodynamic equilibrium with a small vacuum gap in between. (c) Tunneling process at positive tip bias. (d) Tunneling process at negative tip bias.

by their work functions ϕ_t and ϕ_s respectively (Figure 2.2a). The quantum mechanical wavefunctions of the tip and the sample decay exponentially into the vacuum according to equation 2.5 with a decay constant described in equation 2.6. When the tip is brought to within 10 Å (usually 4 ~ 7 Å) of the surface under investigation without any actual physical contact, there will be a very small overlap of the wavefunctions of the tip apex and the surface. In this case, the sample and the tip are in thermodynamic equilibrium and their Fermi levels must be equal, as illustrated in Figure 2.2b. When a bias voltage U is applied to the tip (which is our case), the main consequence is a rigid shift the energy levels of the tip downward or upward by an amount $|eU|$, depending on whether the polarity is positive or negative. For the positive tip bias, the net tunneling current arises from electrons that tunnel from the occupied states of the sample into the unoccupied states of the tip (Figure 2.2c), whereas at negative tip bias, electrons tunnel from the occupied states of the tip into the unoccupied states of the sample (Figure 2.2d). Hence, the bias polarity determines whether unoccupied or occupied sample electronic states are probed. Since the states with the highest energy have the longest decay length into vacuum, most of the tunneling current arises from electrons lying near the Fermi level of the negative-biased electrode. The tunneling current between the tip and the sample can be described by the equation:[282]

$$I = \int_0^{eU} \rho_s(r,E)\rho_t(r,\pm eU \mp E)\exp\left(-\frac{2\sqrt{2m}z}{\hbar}\sqrt{\phi+\frac{eU}{2}-E}\right)dE \qquad (2.7)$$

where ρ_s and ρ_t are the density of states of the sample and the tip respectively as a function of position r and energy E with respective to the Fermi level E_F. From this equation, we can see that for any given lateral position of the tip above the sample, the tunneling current (I) is determined by the tip-sample separation z, the applied voltage (U) and the electronic structure of the tip and the sample. Thus the tunneling current is a convolution of the surface topography and electronic structure of both the tip and the sample.

2.1.2 Physical Principles of STM Instrumentations

In the following, we will focus on the STM design, instrumentation and various modes of operations. Figure 2.3 shows the essential elements of a STM.[281] A probe tip, usually made of tungsten (W) or platinum-iridium (Pt-Ir) alloy, is attached to a piezodrive, which consists of three mutually perpendicular piezoelectric transducers: x piezo, y piezo, and z piezo. Being driven by the coarse positioner first and z piezo subsequently, the tip and the sample can be brought to within a fraction of nanometer (typically 4 ~ 10 Å). Upon applying a voltage, a piezoelectric transducer expands or contracts. By applying a bias voltage to the tip, a tunneling current between the tip and the sample can be induced. The tunneling current is converted to a voltage by the current amplifier which is then compared with a reference current value. The difference is integrated to drive the z piezo. The phase of the amplifier is chosen to provide a negative feedback: if the absolute value of the tunneling current is larger than the reference value, then the voltage applied to the z

piezo tends to withdraw the tip from the sample surface, otherwise, the feedback loop will instruct the tip to approach the sample surface. By applying a sawtooth voltage on the x piezo and a voltage ramp to the y piezo, the tip can

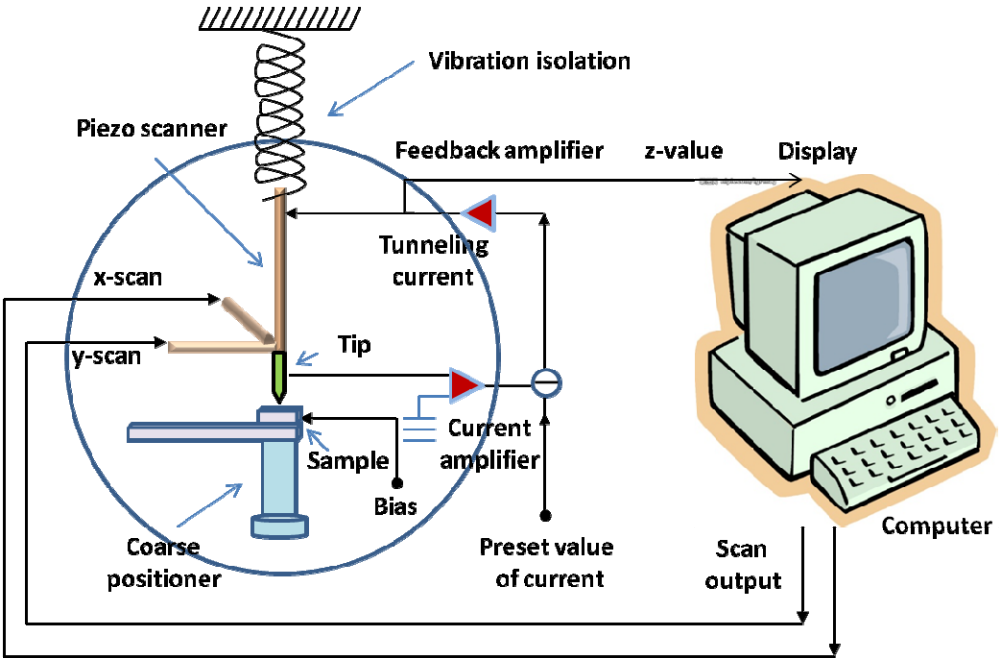

Figure 2.3 The scanning tunneling microscope in a nutshell. The scanning waveforms, applying on the x and y piezos, make the tip raster scan on the sample surface. A bias voltage is applied between the sample and the tip to induce a tunneling current. The z piezo is controlled by a feedback system to maintain the tunneling current constant. The voltage on the z piezo represents the local height of the topography. To ensure stable operation, vibration isolation is essential.

scan on the xy plane. As the tip scans over the xy plane, a 2D array of z position, which represents a contour plot of the equal tunneling-current surface, is obtained, displayed and stored in the computer system. Since tunneling current depends on the tip-sample distance z as well as the local density of states of the sample, a 2D image containing both the topography and electronic information can be obtained by recording the tip height z as a function of the tip position x and y. To achieve atomic resolution, a stability of

the tip-to-sample spacing at the level of 0.1 pm is required. This required stability can only be achieved by combination of an effective isolation system and a rigid design of the STM instrument.

There are two modes for STM imaging, constant current mode and constant height mode, as shown in Figure 2.4. As already described above, in the constant current mode, a feedback is used to adjust the height of the tip during scanning, so that the tunneling current between tip and sample is kept constant. The height z adjustment is performed by applying voltage U_z to the z piezo while the lateral tip position (x,y) is determined by the corresponding voltages U_x and U_y applied to the x piezo and y piezo. Therefore, the recorded signal $U_z(U_x,U_y)$ can be translated into the 'topography' z(x,y) which also includes the contribution from the electronic states of the sample. The constant current mode is the most widely used mode of STM operation, however,

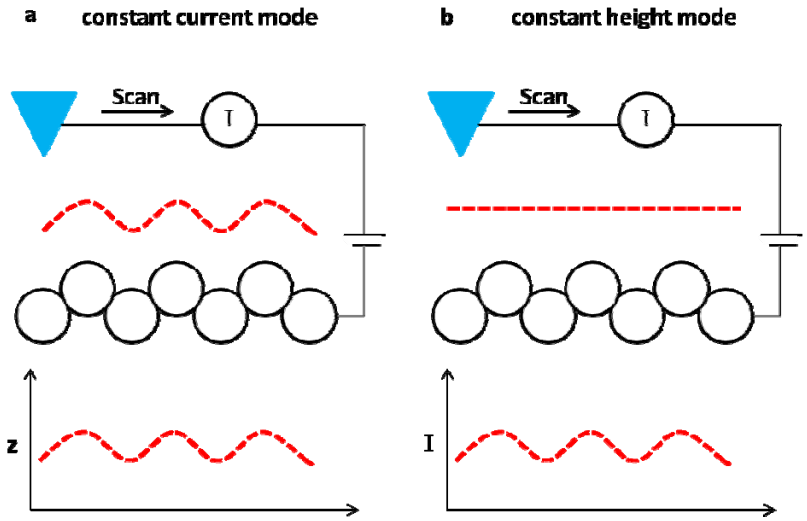

Figure 2.4(a) Schematic illustrations of the constant current mode of STM operation and (b) constant height mode.

a drawback is that the finite response time of the feedback loop limits the scan speed and data acquisition time considerably. In the constant height mode, the tip is scanned across the surface while maintaining the original tip-sample separation at the start of the scan. The feedback can be switched off completely and the modulation of the tunneling current with the full sensitivity of the exponential dependence of the current on tip-sample spacing then reflects the atomic scale 'topography' information with a convolution of the sample electronic structure. This constant height mode can be used to collect STM images at real-time video rates, however, its application is limited to surfaces that are nearly atomically flat over the imaged surface regions, since there is a possibility of the tip crashing into the surface asperities.

2.1.3 Tunneling Through Adsorbates

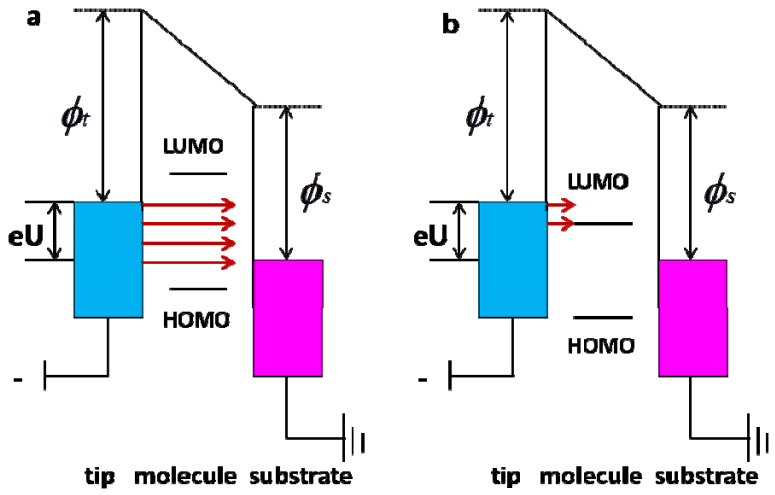

Figure 2.5 Two typical tunneling processes in the adsorbate/substrate system. (a) Electrons directly tunnel from the tip to the substrate as there are no available unoccupied electronic states within the energy window eU_{bias}. (b) Electrons first tunnel from the tip to the adsorbate and then to the substrate because there are some unoccupied electronic states of the adsorbate within the energy window eU_{bias}.

Besides the imaging of clean surfaces, STM can also be used to characterize the adsorbate-covered surfaces.[283] These adsorbates can be atoms or molecules, when they are directly adsorbed on a conductive surface. The discrete levels of the atoms or molecules can be broadened, shifted and mixed because of the interaction with the electronic continuum of the substrate. When a voltage U is applied to the tip (with the sample grounded, which is our case), only those states lying between E_F and E_F + eU contribute to the tunneling current. The sign and magnitude of the applied voltage, then, determine which states can contribute to the resulting topography images.

Figure 2.5 represents two typical tunneling processes that could happen when atoms or molecules adsorbed on a surface. Here, we only show the case where the tip is negatively biased. If there are no available unoccupied states of the adsorbates within the energy window eU, which means that the Fermi level of the tip is aligned in the gap of the adsorbates, electrons will directly tunnel from the tip to the sample (Figure 2.5a).[284] On the other hand, if there are some available unoccupied electronic states within the energy window, the electron will first tunnel from the tip to the unoccupied states of the adsorbates and then to the substrate (Figure 2.5b).[280] Moreover, by tuning the tip bias to different energy, voltage-dependent STM imaging can be achieved. This method often provides a quick and simple way to assess whether there are any interesting differences between different bias voltages.

During the STM imaging, two tunneling processes can occur, elastic tunneling and inelastic tunneling.[83, 285] If the energy of the electron is conserved in the tunneling process, that is to say, the electron energy is equal in the initial and final states, it is said that the electron has tunneled elastically. In contrast, if the electron has gained or lost energy due to interaction with elementary excitation such as phonons, magnons or plasmons, the tunneling process is called inelastic.

2.1.4 Scanning Tunneling Spectroscopy

The spectroscopic capability of STM combined with its high spatial resolution is perhaps the most important feature of STM and has been applied widely.[282] The simplest way of obtaining spectroscopic information of the surface is recording the voltage-dependent STM images. This relies on the fact that at a particular chosen bias voltage, only the electronic states between the Fermi levels of the tip and the sample can contribute to the tunneling current, as already mentioned above. However, the limitation of this procedure is that the constant current STM images generally reveal both geometric and electronic structure information which cannot easily be separated. Therefore, additional experimental techniques have been introduced to extract the electronic structure information more clearly, preferably independent of the surface geometric structure. This is achieved by measuring the differential tunneling conductance (dI/dU). From equation 2.7, we know that the tunneling

current is a function of the sample electronic states involved in the tunneling process. Taking the derivative of equation 2.7, we get:

$$\frac{dI}{dU} \propto \rho_s(r, eU) \tag{2.8}$$

Therefore, structure in dI/dU as a function of U can be attributed to structure of the density of states of the sample.

During the scanning tunneling spectroscopy (STS) measurement, the tip-sample distance is kept constant by switching off the constant current feedback loop.[281] A high-frequency sinusoidal modulation voltage is superimposed on the constant d.c. bias voltage applied between tip and sample. By recording the tunneling current modulation, which is in-phase with the applied bias voltage modulation, by means of a lock-in amplifier, an atomically resolved spectroscopic signal dI/dU can be obtained. The measurements of local dI/dU curves at constant tip-sample separation can be extended to every pixel in an image, which is referred to as dI/dU mapping. It uses a sample-and-hold amplifier to alternately gate the feedback loop on and off. During the time of active feedback, a constant stabilization voltage U is applied to the tip and the tip height is adjusted to maintain a constant tunneling current. When the feedback loop is deactivated, the applied tip voltage is linearly ramped between two preselected values and the dI/dU curve is measured at a fixed tip height. Afterwards, the applied bias voltage is set back to the chosen stabilization voltage U and the feedback system is reactivated. By acquiring the dI/dU curves rapidly while scanning the tip at low speed, a

constant current topography and spatially resolved spectroscopic signal dI/dU can be obtained simultaneously.

2.1.5 Computational Simulation of STM Images

The calculations were performed using DFT implemented in the Vienna *Ab Initio* Simulation Package (VASP) within the generalized gradient approximation plus DFT-D2 van der Waals (vdW) correction. The exchange-correlation functional of Perdew-Burke-Ernzerhof and the projector-augmented wave methods were used. The plane-wave basis cutoff energy was set to 500eV. The criteria of convergence for energy and force were set to 10^{-5} eV and 0.02 eV/Å. A (3×3×1) k-point grid was used. STM images were simulated using the Tersoff and Hamann approximation. Adsorption configurations of VOPc molecules on graphene were studied using DFT calculations. A slab with a 40 Å vacumm layer was used.

2.1.6 Multi-chamber LT-STM System

Our LT-STM system is a custom-built multichamber ultra high vacuum (UHV) system with a base pressure of about 10^{-10} mbar, housing an Omicron LT-STM interfaced to a Nanonis controller.[203, 286, 287] The UHV environment is utilized to avoid the sample surface contamination, and this is achieved through the combination of rotary pump, turbomolecular pump and ion pump. Figure 2.6 shows the photography of our LT-STM system, which consists of a load-lock chamber, a preparation chamber and a LT-STM analysis chamber

separated by gate valves. The transfer arm allows *in-situ* transfer between the

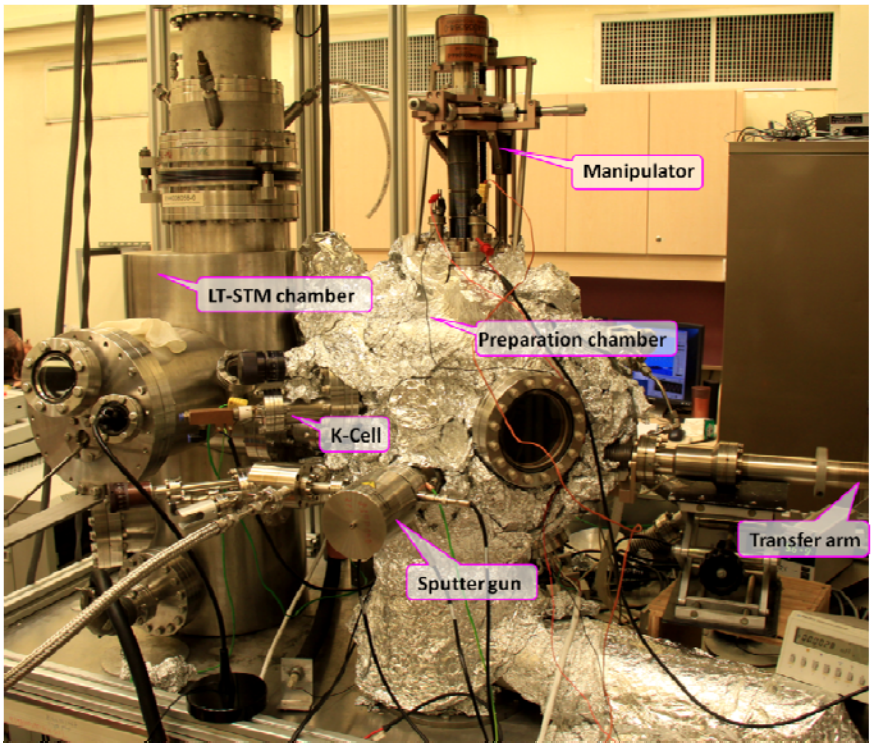

Figure 2.6 Photograph of multi-chamber UHV system used for LT-STM experiment.

load-lock, preparation chamber and the LT-STM chamber. The preparation chamber is equipped with a manipulator, a sputter gun and several Knudsen cells. The manipulator is used to fix the sample to desired positions for sample cleaning (sputtering) and molecular deposition. It can also be used for sample degassing and post-annealing process, depending on the sample properties, either direct heating or filament heating can be applied. The STM chamber is cooled by a cryostat filling with liquid nitrogen or liquid helium, which can cool the sample down to 77K or 4K. The low temperature environment minimizes thermal diffusion of molecules on the surface which can both improve the image quality and reduce the thermal broadening of electron energy states during STS measurement. All STM images in this thesis are

recorded in constant current mode with a chemically etched tungsten tip at liquid nitrogen temperature (77K) with the bias voltage applied to the tip.

2.2 Ultraviolet Photoelectron Spectroscopy

2.2.1 Basic Principles of Ultraviolet Photoelectron Spectroscopy

As mentioned in Chapter 1, the arrangement of molecules on surfaces is governed by a combination of molecule-substrate interactions and intermolecular interactions. Ultraviolet photoelectron spectroscopy (UPS) is the most established tool to investigate the interface electronic properties and hence it can be used to evaluate the nature of molecule-substrate interfacial interactions and intermolecular interactions.[288] A typical experiment setup for UPS measurement is schematically shown in Figure 2.7,

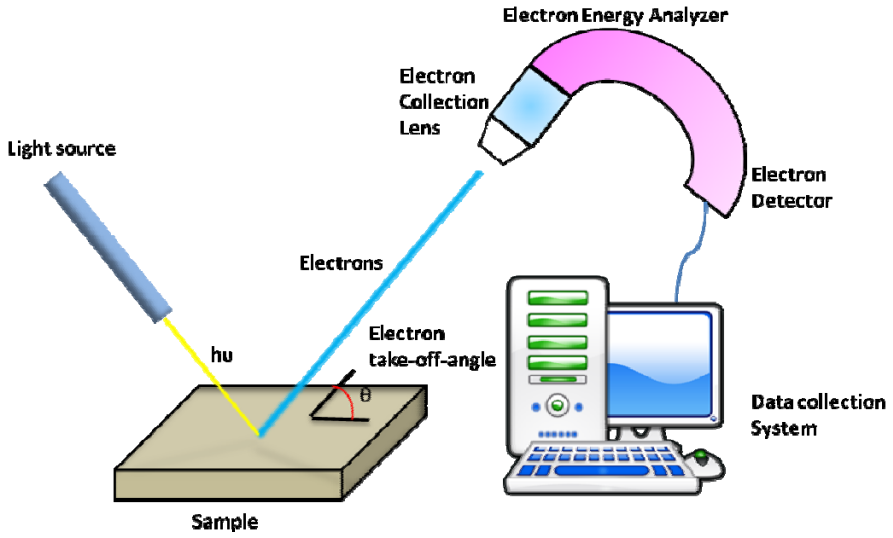

Figure 2.7 A typical experimental setup for UPS measurements, including a light source, an electron energy analyzer and a data collection system.

including a light source, an electron energy analyzer and a data collection system. In general, UPS utilizes ultraviolet light sources (e.g., rare gas discharge, monochromatized synchrotron radiation) to excite photoelectrons

from the shallow valence states, therefore serving as a probe for the valence bands of solids. For the UPS studies, the kinetic energy of photoelectrons is in the range of some eV to several ten's eV, resulting in high surface sensitivity of this technique, as the inelastic mean free path of such electron is below 1nm.[289]

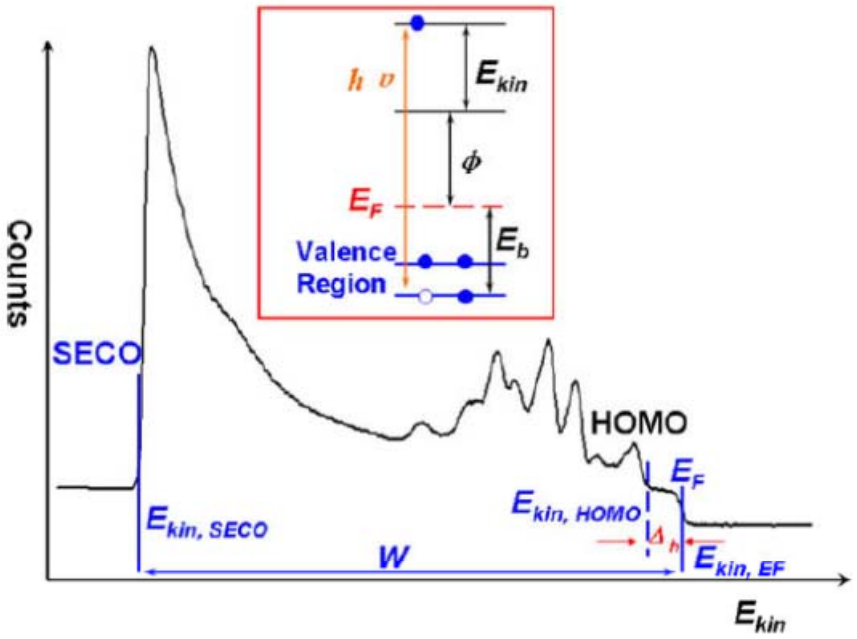

Figure 2.8 Example of a typical PES spectrum showing the various energy levels. The inset displays the schematic of photoelectron emission process in a PES experiment. Reprinted from ref. 291, with permission from Elsevier, copyright 2009.

The kinetic energy of the photoelectron directly after emission from the sample is

$$E'_{kin} = h\upsilon - E_B - \phi_{sample} \qquad (2.9)$$

where the $h\upsilon$ is the energy of the photon irradiation, E_B is the electron binding energy relative to the substrate Fermi level E_F, and ϕ_{sample} is the sample work function.[290] The kinetic energy of the emitted photoelectron is measured by a spectrometer. However, in most cases, the work function of the

spectrometer ϕ_{spec} is different from ϕ_{sample}. Hence, the kinetic energy of the electron measured by the spectrometer will be

$$E_{kin} = h\upsilon - E_B - \phi_{spec} = E'_{kin} - \left(\phi_{spec} - \phi_{sample}\right) \quad (2.10)$$

For a given experimental setup ϕ_{spec} is a constant, and therefore the binding energy of the electrons of the sample can be measured. By keeping $h\upsilon$ fixed and sweeping the measured kinetic energy, the energy distribution curve is obtained. Figure 2.8 shows a typical UPS spectrum, which can be divided into the low kinetic energy secondary-electron region and the high kinetic energy valence band region.[291] These secondary electrons stem from inelastically scattered (within the sample) photoelectrons. The electrons at the secondary-electron cut-off (SECO) are able to leave the sample in the limit of $E'_{kin} = 0$, however, all electrons with $E'_{kin} < \phi_{spec} - \phi_{sample}$ would not be able to enter the spectrometer. In order to overcome this potential barrier and enable the measurement of the SECO, a negative potential of a few volts is applied to the sample, rigidly shifting all energy levels upwards relative to the spectrometer. Now the spectrum is measured with a kinetic energy higher by the amount of the applied negative potential. From the spectrum, we can obtain the sample work function

$$\phi_{sample} = h\upsilon - w = h\upsilon - \left(E_{kin,\,E_F} - E_{kin,\,SECO}\right) \quad (2.11)$$

where $E_{kin,\,E_F}$ and $E_{kin,\,SECO}$ are the kinetic energy of the sample Fermi level and the SECO respectively, and w is the width of the spectrum. The hole injection barrier (HIB) and the ionization potential energy (IP) can also be

determined from the spectrum. The HIB is commonly defined as the energy difference between E_F and HOMO,

$$HIB = E_{kin,\,E_F} - E_{kin,\,HOMO} \tag{2.12}$$

where $E_{kin,\,HOMO}$ is the linear extrapolation of the high-kinetic energy onset of the HOMO peak, as shown in Figure 2.8. The IP of the organic material is the energy difference between the HOMO and the vacuum level, it can be derived from the following equation:

$$IP = h\upsilon - \left(E_{kin,\,HOMO} - E_{kin,\,SECO}\right) \tag{2.13}$$

The information of the unoccupied states can be obtained from the inverse photoemission spectroscopy (IPES), or simply estimated from the transport band gap to the HOMO.

2.2.2 Multi-chamber UPS System

The UPS experiments were carried out in a custom-built multi-chamber UHV system.[292, 293] Figure 2.9 shows the setup of our UPS system, it consists of load-lock chamber, preparation chamber, chemical reaction chamber and the analysis chamber separated by gate valves. The transfer arm allows *in-situ* transfer between different chambers. The preparation chamber is equipped with a manipulator, a quartz crystal microbalance (QCM) and several Knudsen cells. Sample degassing, molecular deposition and post-annealing can be performed in this chamber. The chemical reaction chamber is mounted with a sputter gun, a manipulator and a variable leak valve. In this chamber, the reaction of organic thin films on the sample surface with various gases at

different temperatures can be carried out. The analysis chamber is installed with a UV-lamp, a twin anode X-ray gun, a low energy electron diffraction (LEED) and an Omicron EA125 electron energy analyzer. The UPS measurement is done in the analysis chamber using He I (21.1 eV) as the excitation source. The vacuum level is measured through the linear extrapolation of SECO with -5 V sample bias. The binding energy is referred to the Fermi level of a sputter-cleaned gold foil.

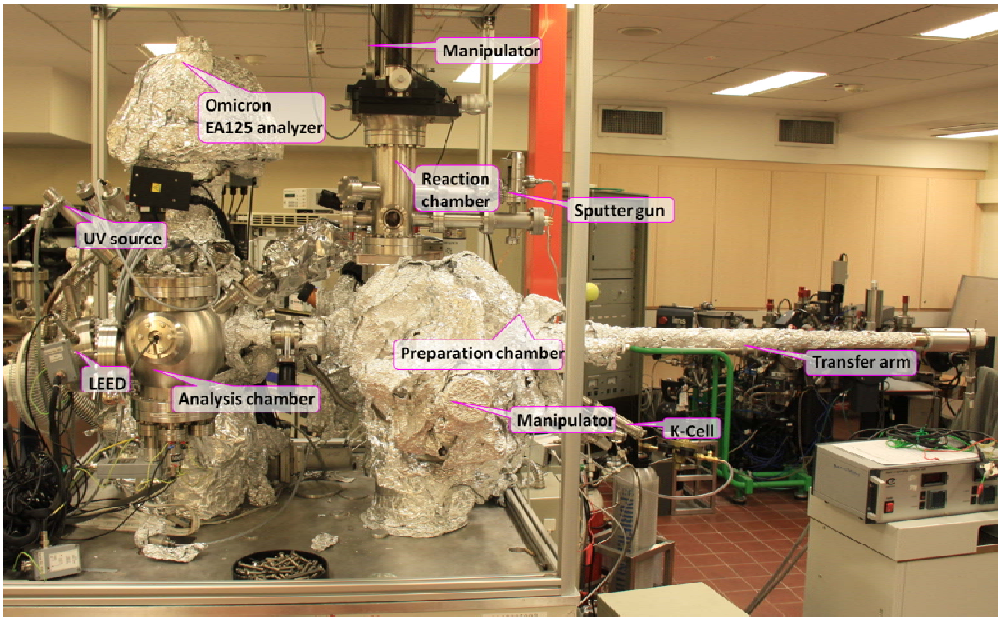

Figure 2.9 Photography of multi-chamber UHV system used for UPS measurement.

2.3 Sample Preparation

2.3.1 Substrate Preparation

The substrates used in this thesis are single crystal Ag(111) and highly oriented pyrolytic graphite (HOPG). A clean Ag(111) surface with large terraces was obtained by a few cycles of Ar^+ sputtering and subsequent annealing at 800K. In order to get a clean HOPG substrate, a freshly cleaved

HOPG was thoroughly degassed in the UHV chamber at around 800K overnight.

2.3.2 Basic Properties of the Molecules

A molecule is an electrically neutral group of two or more atoms held together by chemical bonds. The chemical and physical properties of an molecule is to a great extent determined by the molecular orbitals. We know that atomic orbitals describe the wave-like behavior of the electrons in an atom. Molecular orbitals are the linear combination of atomic orbitals. When atomic orbitals interact, the resulting molecular orbitals can be of three types: bonding, antibonding and nonbonding. The bonding molecular orbitals has lower energy than the atomic orbitals that combine to produce them whereas the bonding molecular orbitals has higher energy. Nonbonding molecular orbitals have the same energy as the atomic orbitals of one of the atoms in the molecule. There will be a range of filled and empty orbitals in the molecule. However, in the molecular interaction, special attention is paid to the frontier orbitals. One is the highest occupied molecular orbital (HOMO) and another is the lowest unoccupied molecular orbital (LUMO).

The HOMO and LUMO orbitals are most important in determining the chemical reactivity of molecules. It can also determine the charge transfer direction between two different molecules. If we use a reference orbital, the molecules can be classified into donor type and acceptor type. For the donor, the HOMO is higher in energy than that of a reference orbital. For the acceptor,

the LUMO is lower in energy than that of a reference orbital. However, the classification of the donor and acceptor type is not absolute. This is because the driving force for an electron transfer is related to the difference in energy between the orbitals not the absolute energy.

The molecules used in this thesis include pentacene, C_{60}, VOPc, PFP and ClAlPc. Molecules were thermally evaporated from Knudsen cells onto the clean substrate kept at room temperature. Deposition rate was monitored by a QCM first and further calibrated by counting the adsorbed molecule coverage in large-scale STM images. Prior to deposition, all the molecular sources were purified by gradient vacuum sublimation. For the fabrication of binary molecular networks, different molecules were sequentially deposited from separated Knudsen cells onto the substrates. All the sample annealing processes were performed with the filament heating.

Chapter 3: LT-STM/UPS Investigation of Two-Dimensional Crystallization of C_{60}:Pentacence Binary System

3.1 Introduction

As already discussed in Chapter 1, the controlled assembly and positioning of functional molecules into ordered 2D molecular architectures on solid surfaces represents a promising bottom up approach for the realization of molecule-based miniaturized devices in the field of organic,[294] molecular electronics[17] and biosensors.[295] In recent years, the concepts of supramolecular chemistry have been extensively exploited to engineer molecules into well-ordered 2D supramolecular architectures stabilized by non-covalent intermolecular interactions (such as van der Waals forces, hydrogen-bonding and metal-ligand interactions),[135, 153, 154, 159, 160, 167, 173, 201, 210, 239, 240, 242, 243, 296-309] and robust covalent chemical bond formation.[128, 310] In particular, this endeavour has led to the creation of surface porous nanotemplates which provide ordered preferential adsorption sites to selectively accommodate guest molecules, thereby resulting in the formation of well-ordered guest molecular arrays.[135, 154, 173, 300] The periodicity or symmetry of the resulting guest molecular arrays can be further tuned by modifying the geometry and intermolecular interactions of the "building blocks" of the porous nanotemplates. Another strategy is to manipulate the intermixed phase of binary or multi-component molecular systems that are largely governed by the interplay between intermolecular and

molecule-substrate interactions.[153, 201, 301-306] A great variety of novel supramolecular assemblies including 1D molecular chains and 2D arrays with tunable periodicity have been achieved by carefully controlling the intermixed molecule ratio. An elegant example is the assembly of tunable 1D C_{60} molecular chain arrays by manipulating the binary molecular systems of C_{60}:α-Sexithiophene[201] and C_{60}:*p*-Sexiphenyl.[305, 306]

Understanding and hence the controlling of the nanostructure formation at the organic donor-acceptor heterojunction interfaces are also crucial for organic photovoltaic cells (OPVs).[311-317] The formation of interdigitized nanostructures could significantly enhance exciton dissociation at the donor-acceptor heterojunction interfaces, hence achieving better power conversion efficiency. Intensive research efforts have been devoted to the understanding of the interface nanostructure formation mechanism, as well as the development of various interface engineering approaches to effectively control the interface nanostructure formation.[311-317] The self-assembly or 2D crystallization of organic donor-acceptor binary molecular system on single crystal substrate could represent an ideal model system to provide the atomic scale understanding of the interface nanostructure formation mechanism through the manipulation of intermolecular and molecule-substrate interface interactions at different strength and length scales.[315, 316]

In this chapter, we study the fabrication of highly ordered C_{60} 2D

molecular arrays including C_{60} nanomesh networks, C_{60} pentamer and C_{60} pair arrays by simply controlling the post-annealing temperature of the binary molecular system of C_{60} and pentacene on Ag(111). The 2D crystallization processes on Ag(111) were monitored by *in-situ* LT-STM, and compared with the same system on inert graphite surface. The interfacial charge transfer and energy level alignment between C_{60} and pentacene films were evaluated by *in-situ* UPS.

3.2 LT-STM Study of C_{60}:Pentacence Binary System on Ag(111)

The molecular structures of C_{60} and pentacene are shown in Figure 3.1a. We firstly self-assembled a highly periodic pentacene superstructure on Ag(111) by room temperature deposition of 0.7 ML pentacene on Ag(111) (1ML pentacene corresponds to a close-packed monolayer pentacene on Ag(111)) and subsequent annealing at 380 K for 30 min. Figure 3.1c and 3.1d show a representative large scale (50×50 nm^2) and molecularly-resolved (7×7 nm^2) STM images of the pentacene array, respectively, in which individual pentacene molecules can be clearly identified as characteristic rod-like features. All the pentacene molecules lie flat with their π plane parallel to the Ag(111) surface. A rectangular unit cell is highlighted on the image with $a_1 = 2.90 \pm 0.02$ nm and $b_1 = 1.03 \pm 0.02$ nm. We propose a model involving loosely packed pentacene units with a "brick-wall" structure, as shown in the schematic drawing of Figure 3.1b.[307] This pentacene arrangement is similar to the structure recently observed by Dougherty *et al.*[318]

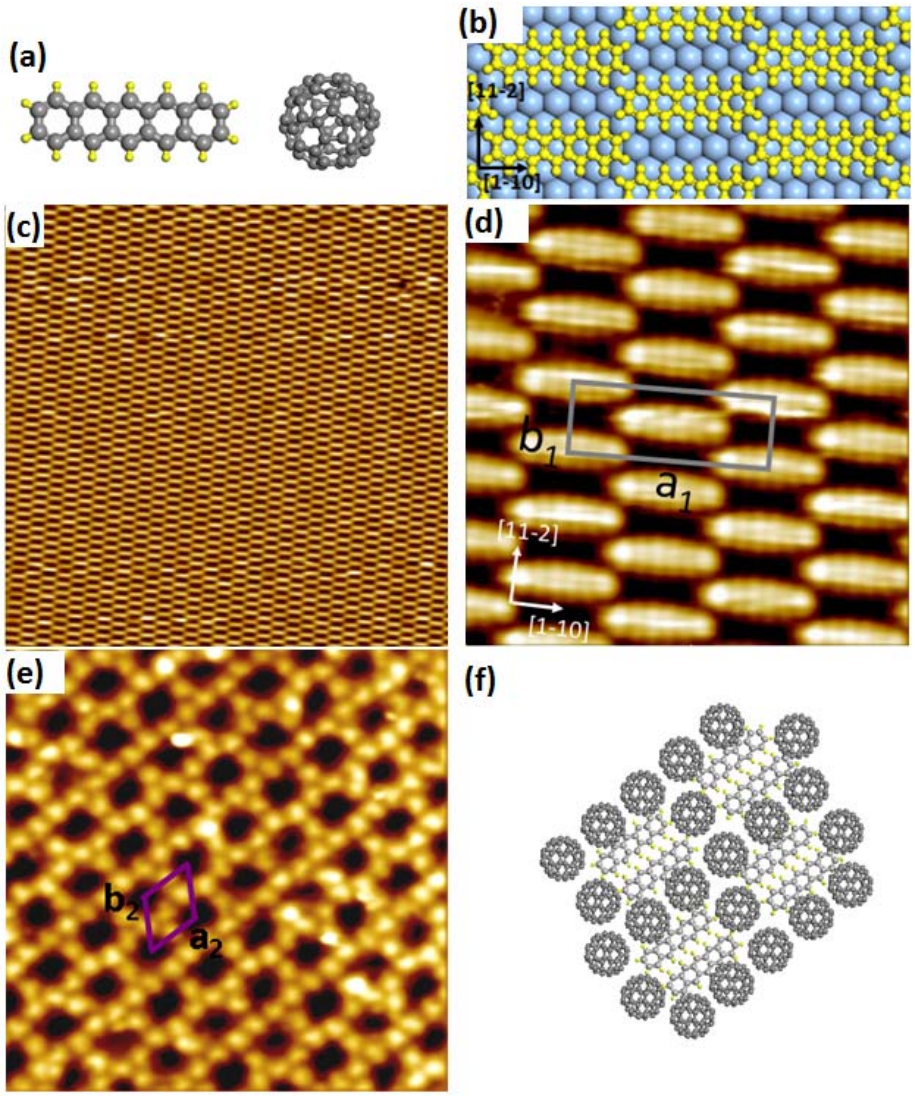

Figure 3.1 (a) Molecular structures of pentacene and C_{60}. (b) Schematic model for the packing structure of the "brick-wall" pentacene superstructure on Ag(111). (c) Large scale STM image (50 × 50 nm^2, V_{tip} = -0.9 V) of the "brick-wall" pentacene superstructure on Ag(111). (d) The corresponding molecularly-resolved STM image (7 × 7 nm^2, V_{tip} = -0.9 V). (e) STM image (20 × 20 nm^2, V_{tip} = -1.5 V) and (f) the corresponding proposed model of 2D C_{60} nanocavity network after the room temperature deposition of 0.7 ML C_{60} onto the pentacene covered Ag(111) and followed by subsequent annealing at 360K.

Room temperature deposition of about 0.7 ML C_{60} onto this ordered pentacene superstructure resulted in the formation of rather disordered C_{60} structures, in contrast to the hexagonally close packed (hcp) C_{60} monolayer on clean Ag(111). A regular extended 2D nanomesh structure with an ordered

nanocavity array, referred to as **network 1,** was formed when the sample was annealed at 360 K for 30 min, as shown in Figure 3.1e. The ordered nanocavities are defined by a regular arrangement of C_{60} molecules and have a unit cell of $a_2 = 2.62 \pm 0.02$ nm, $b_2 = 2.10 \pm 0.02$ nm, and $\alpha_2 = 60^o \pm 2^o$. Figure 3.1f shows a schematic model proposed for the formation of the ordered network as we previously reported.[28] It involves the C_{60} adsorption-induced structural rearrangement of pentacene into pentacene pair arrays, accompanied by the decoration of C_{60} aside the pentacene pairs.[307] We have previously demonstrated that the ordered 2D **network 1** serves as an effective template for selective inclusion of guest C_{60} molecules at the cavity sites.[307]

Annealing this C_{60}:Pentacene binary molecular system at 370 K for 80 min leads to the structural transformation from the long range ordered nanomesh structure (**network 1**) to the assemblies involving the coexistence of two different types of C_{60} superstructures, as highlighted by domain 1 and 2 in Figure 3.2a. Figure 3.2b shows the molecularly-resolved STM image of the ordered 2D array in domain 1, referred to as **network 2**. **Network 2** is constituted by an ordered packing of C_{60} molecular pairs. The C_{60}-C_{60} distance within the pair is 1.0 nm, close to the van der Waals length in C_{60} solids,[319] whereas the inter-pair distance along the packing direction is 1.72 nm. As such, the regular arrangement of C_{60} molecular pairs gives rise to a nanocavity array with the unit cell of $a_3 = 1.98 \pm 0.02$ nm, $b_3 = 1.72 \pm 0.02$ nm, and $\alpha_3 = 70^o \pm 2^o$. We propose a model for the **network 2** as shown in Figure 3.2c, involving the

thermal annealing induced rearrangement of C_{60} and pentacene on Ag(111) into a superstructure comprising of C_{60} pairs interlinked through a single pentacene molecule. As compared with the nanomesh structure (**network 1**) in Figure 3.1e, the size of the nanocavity in **network 2** is decreased, suggesting the possibility to fabricate 2D nanomesh templates with tunable nanocavity size to selectively accommodate guest molecules with different molecular dimension.

Figure 3.2d displays the high-resolution STM image for the coexisting C_{60} superstructure in domain 2 (Figure 3.2a). The C_{60} molecules are arranged into ordered trapezoid-shaped assemblies composing five C_{60} molecules, henceforth referred to as the C_{60} pentamer array. The unit cell of the C_{60} pentamer array is highlighted in Figure 3.2d with $a_4 = 2.31 \pm 0.02$ nm, $b_4 = 2.73 \pm 0.02$ nm, and $\alpha_4 = 70^o \pm 2^o$. The intermolecular distance within one C_{60} pentamer is around 1 nm, close to the van der Waals distance of C_{60} molecules, indicating that the van der Waals interaction plays an important role in stabilizing this C_{60} pentamer superstructure. As such, a proposed model for the C_{60} pentamer array is shown in Figure 3.2e. At this stage, the occupancy percentage of the C_{60} pentamer array is estimated to be 40%, as judged from large-scale STM images. When the sample was annealed at 410 K for 30 min, the C_{60} pair **network 2** was completely disappeared and the surface was then dominated by the C_{60} pentamer array, as shown by the large area STM image in Figure 3.2f.

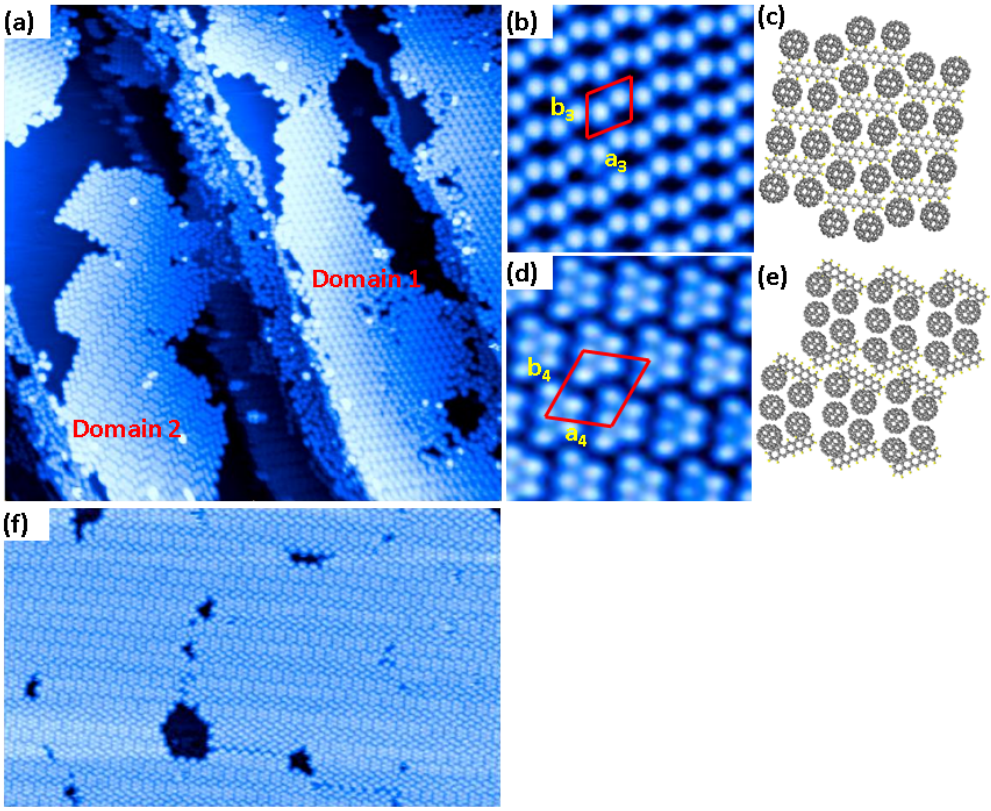

Figure 3.2 (a) Large scale STM image (100 × 100 nm^2, V_{tip} = -2.1 V) for C_{60}:pentacene binary system after annealing at 370K for 80 min, the observed two different domains (1 and 2) are highlighted. (b) Close up STM image (10 × 10 nm^2, V_{tip} = -2.1 V) and (c) the corresponding proposed model of 2D C_{60} pair network in domain 1. (d) Close up STM image (10 × 10 nm^2, V_{tip} = -2.0 V) and (e) the corresponding proposed model of the C_{60} pentamer arrays in domain 2. (f) STM image (60 × 100 nm^2, V_{tip} = -2.1 V) of the C_{60}:pentacene binary system after annealing at 410K for 30 min.

Interestingly, we can observe the insertion of C_{60} pairs between C_{60} pentamers in some area of STM images as shown in Figure 3.2f. Figure 3.3a displays a large scale STM image in another region after annealing at 410K. In addition to the C_{60} pentamer array (up-right corner) and the C_{60} pentamer array with the insertion of C_{60} pair (Figure 3.3b), a locally ordered C_{60} pair superstructure adopting a herringbone arrangement can be observed, as shown by the corresponding high resolution image in Figure 3.3c. The unit cell of the C_{60} pair array is highlighted in Figure 3.3c with a_5

= 2.31 ± 0.02 nm, b_5 = 2.72 ± 0.02 nm, and α_5 = 88° ± 2°. Similar to the above-mentioned models, we propose a schematic model in Figure 3.3d involving the rearrangement of the pentacenes molecules on Ag(111) to accommodate the C_{60} pairs. However, due to the difficulty of the direct imaging of pentacene molecules in these C_{60} superstructures, we are not able to provide conclusive experimental evidence for our proposed models. Theoretical calculations are needed to confirm our proposed models.

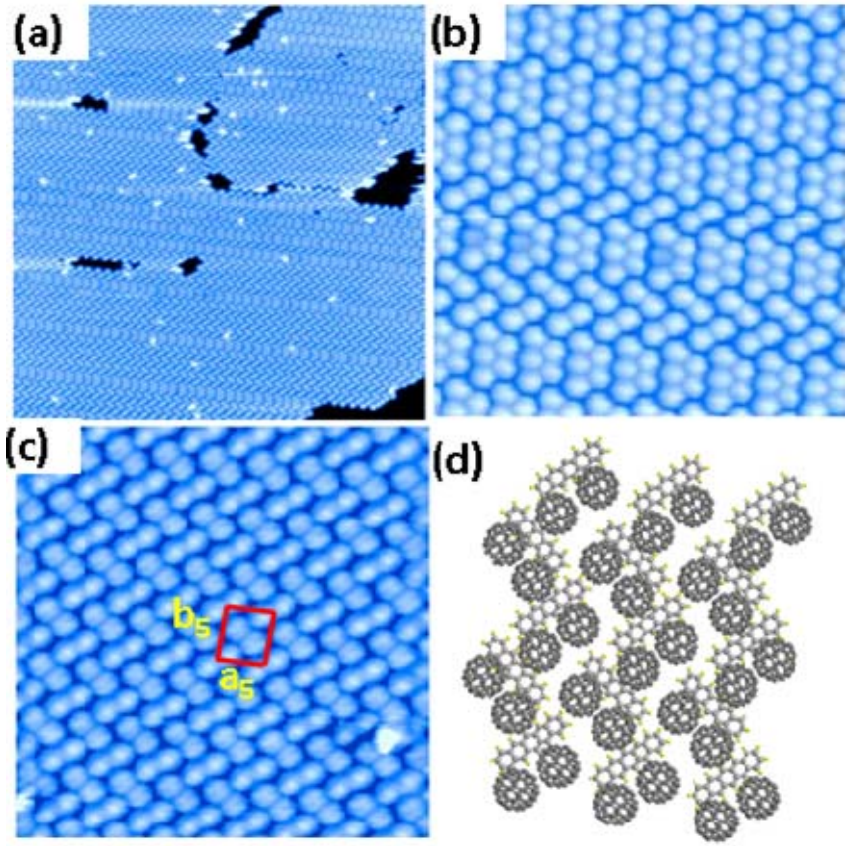

Figure 3.3 (a) Large scale STM image (100 × 100 nm^2, V_{tip} = -2.0 V) for C_{60}:pentacene binary system after annealing at 410K for 30 min. (b) The corresponding close up STM image (20 × 20 nm^2, V_{tip} = -2.0 V) shows the insertion of C_{60} pairs between C_{60} pentamers. (c) STM image (20 × 20nm^2, V_{tip} = -2.0 V) and (d) the corresponding model of a locally ordered herringbone C_{60} pair structure.

It is well known that the self-assembly of ordered molecular structures on

metal surfaces is generally controlled by the subtle balance between the intermolecular interactions and molecule-metal interaction at the different strength and length scale.[167, 210, 240, 242, 243, 297, 298] The intermolecular interaction between acceptor-type C_{60} and donor-type pentacene molecules can involve π-π interaction (curvature π-plane in C_{60} and planar π-plane in pentacene), and weak donor-acceptor charge transfer interaction. STM images at the defect sites (not shown here) reveal that the arrangement of pentacene superstructures was significantly modified by the inclusion of C_{60}. The re-arranged pentacene structures can provide an effective "skeleton" to guide the formation of the characteristic ordered C_{60} array. The intermolecular distance within the C_{60} pairs and pentamers is 1 nm, close to the van der Waals interaction distance of C_{60}.[319] This indicates that the C_{60}-C_{60} van der Waals interaction stabilizes the structure within basic "blocks" for different C_{60} arrays. In addition to the intermolecular interactions, the interaction between C_{60} or pentacene molecules and the Ag(111) surface should be considered. Previous studies have shown that the energy of the molecule-metal interfacial interaction involving electronic coupling between molecules and metal surface can be several times larger than that of the intermolecular van der Waals interactions.[320, 321] Therefore, the strong molecule-Ag(111) interactions arising from the effective coupling between the d-bands in Ag and molecular π-orbitals (pentacene and C_{60}) play a key role in interlocking the long-range ordered C_{60} molecular arrays on Ag(111). As such, we propose that the

delicate interplay between the intermolecular (C_{60}-pentacene and C_{60}-C_{60}, pentacene-pentacene) interactions and molecule-Ag(111) interaction stabilizes the ordered C_{60} molecular arrays. Such interplay between different interactions can be subtly modified by carefully choosing appropriate annealing temperatures, resulting in various well-ordered 2D C_{60} molecular arrays in our experiment.

3.3 LT-STM Study of C_{60}:Pentacence Binary System on HOPG

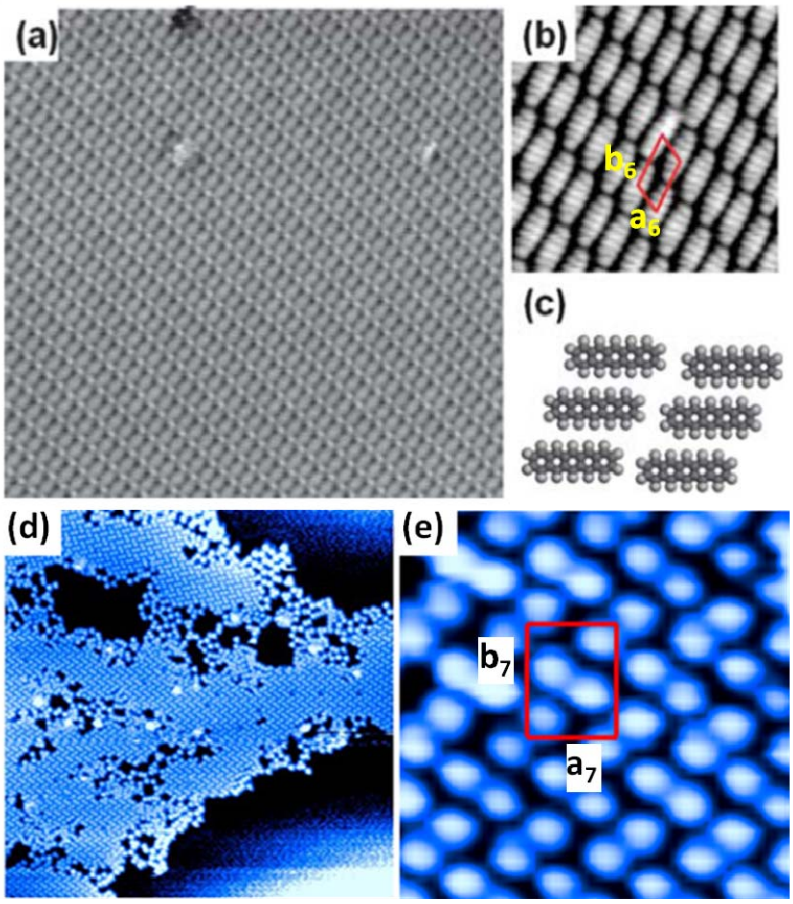

Figure 3.4 (a) Large scale STM image for lying down pentacene monolayer on HOPG surface (30 × 30 nm^2, V_{tip} = -2.0 V). (b) Corresponding detailed 8 × 8 nm^2 image (V_{tip} = -1.6 V). (c) Schematic drawing for the proposed molecular packing structure of lying down pentacene on HOPG. (d) Large scale STM image (100 × 100 nm^2, V_{tip} = -2.3 V) of C_{60} on monolayer pentacene covered HOPG. (e) The corresponding close up STM image (10 × 10 nm^2,V_{tip} = 2.3V) of the locally ordered herringbone C_{60} pair structure. Reprinted from ref. 345, with permission from the Royal Society of Chemistry, copyright 2008.

To evaluate the effect of molecule-substrate interfacial interactions on the 2D crystallization of C_{60}:pentacene binary system, we carried out the same self-assembly experiments of C_{60} on monolayer pentacene covered HOPG substrate. In contrast to the strong interfacial interaction between C_{60} (pentacene) and Ag(111), the C_{60}-HOPG and pentacene-HOPG interfacial interactions are mainly dominated by the relatively weak van der Waals forces or π-π interactions. Figure 3.4a shows a large scale STM image of a well-ordered pentacene monolayer on HOPG.[345] The corresponding molecular-resolved STM image is shown in Figure 3.4b, where the rod-like bright feature represents a single pentacene molecule. All pentacene molecules lie flat on HOPG with their extend π-plane parallel to the substrate. The unit cell is highlighted in Figure 3.4b with $a_6 = 0.89 \pm 0.02$ nm, $b_6 = 1.63 \pm 0.02$ nm, and $\alpha_6 = 60^o \pm 2^o$. The schematic drawing in Figure 3.4c shows the proposed molecular packing structure of monolayer pentacene on HOPG. Figure 3.4d shows the large scale STM image after room temperature deposition of 0.7 ML C_{60} on monolayer pentacene. It is found that short-range ordered C_{60} pair array assembled into irregularly shaped island. As shown by the corresponding high resolution STM image in Figure 3.4e, such C_{60} pair array adopts a very similar structure with the one on Ag(111) (Figure 3.3c). The unit cell of $a_7 = 2.45 \pm 0.02$ nm, $b_7 = 2.70 \pm 0.02$ nm, and $\alpha_7 = 90^o \pm 2^o$ is highlighted in Figure 3.4e. It is worth noting that the C_{60} pair array is the only observed superstructures on HOPG even after annealing at different temperatures. This

clearly reveals that molecule-substrate interfacial interactions strongly affect the self-assembly processes of the C_{60}:pentacene binary system.

3.4 UPS Study of C_{60}:Pentacence Intermolecular Interactions

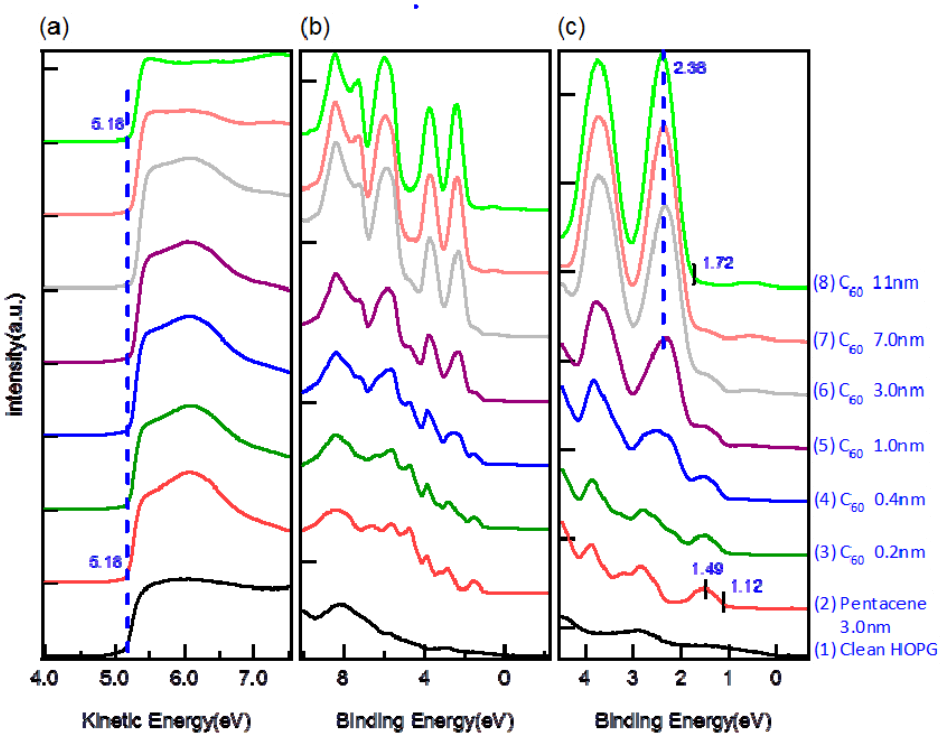

Figure 3.5 Evolution of UPS spectra at (a) low kinetic energy region, (b) and (c) low binding energy region near the Fermi level during the sequential deposition of C_{60} on 3nm pentacene covered HOPG. All binding energy are referred to the substrate Fermi level.

As the interfacial interactions between C_{60} (pentacene) and HOPG are weak, C_{60} on pentacene film on HOPG can be used as a good model system to understand the nature of C_{60}-pentacene intermolecular interactions, in particular, the strength of the donor-acceptor charge transfer interaction, by using *in-situ* UPS experiments. Figure 3.5 shows the evolution of thickness dependent UPS valence band (VB) spectra at the low-binding energy region (Figure 3.5b and 3.5c), and at the low-kinetic energy region (SECO measured with -5V sample bias, Figure 3.5a) during the deposition of C_{60} on 3 nm

pentacene film on HOPG at RT. Clearly, the vacuum level (as determined through the linear extrapolation of the low-kinetic energy onset in Figure 3.5a) is almost aligned at the C_{60}/pentacene interface during C_{60} deposition, suggesting that there is a negligible or at most very weak charge transfer occurring at the C_{60}/pentacene donor-acceptor heterojunction interface.[322, 323] This can be further confirmed by the evolution of the thickness dependent VB spectra in Figure 3.5b and 3.5c. Spectrum 2 in Figure 3.5b and 3.5c shows the typical VB structure of a pentacene thin film, with the HOMO peak centered at the binding energy of 1.49 ± 0.02 eV, and the HOMO leading edge at 1.12 ± 0.02 eV. Sequential deposition of C_{60} top layer leads to the appearance of a C_{60}–related HOMO peak centered at 2.38 ± 0.02 eV and the HOMO leading edge at 1.72 ± 0.02 eV (Figure 3.5c). As shown in Figure 3.5c, we did not observe any apparent binding energy shift of both pentacene- and C_{60}-related HOMO peaks during the sequential deposition of C_{60}. This suggests that the degree of the charge transfer at the C_{60}:pentacene interface is negligible or very small, and hence the interface is dominated by the π-π interaction (between the curvature π-plane in C_{60} and the planar π-plane in pentacene).

Figure 3.6 shows the schematic energy level alignment diagram at the C_{60}/pentacene interface, where the position of LUMO is estimated by taking account of the HOMO-LUMO gap measured by UPS and IPES.[324] The diagram clearly reflects the nature of vacuum level alignment and the flat band condition at this interface.

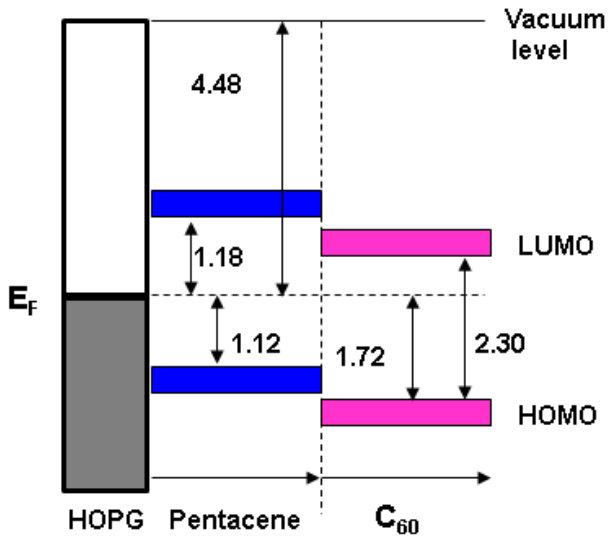

Figure 3.6 Schematic diagram of the energy level alignment at the C_{60}/pentacene heterojunction interface.

3.5 Summary

In this chapter, we demonstrate the fabrication of a variety of well-ordered C_{60} molecular arrays including C_{60} nanomesh networks, C_{60} pentamers and C_{60} pairs on Ag(111) by controlling the annealing temperatures for the C_{60}-pentacene (donor-acceptor) binary molecular system. The formation of different C_{60} molecular arrays is ascribed to the subtle interplay between C_{60}-pentacene intermolecular interaction, C_{60}-Ag(111), and pentacene-Ag(111) interfacial interactions. This result suggests that controlling the self-assembly or 2D crystallization processes of binary molecular (especially donor-acceptor) systems represents a versatile route to fabricating novel 2D molecular architectures. Such detailed study could also help better understanding of the nanostructure formation mechanism at the organic donor-acceptor heterojunction interfaces for their application in organic solar cells.

Chapter 4: Single Molecule Tunneling Spectroscopy Investigation of Reversibly Switched Dipolar Vanadyl Phthalocyanine on Graphite

4.1 Introduction

In the previous chapter, we demonstrate the fabrication of various C_{60} nanostructure arrays through self-assembly. To further extend their applications in molecular nanodevices, it is necessary to introduce desired functionality into these self-assembled molecular nanostructure arrays. By rational design of molecules with molecular centers featuring key functionalities such as dipole moment or magnetic moment and peripheral atoms for intermolecular hydrogen bonding, the fabrication of long-range-ordered molecular nanostructure arrays with desired functionalities over the macroscopic area can be achieved. The most appealing example of a functional molecule is formed by a molecular switch. Understanding and controlling molecular switches on surfaces are not only of fundamental importance, but also essential for construction of molecule-based electronic devices. A prerequisite for the realization of a molecular switch is the ability to manipulate a single molecule between bistable[41-53, 56, 59, 62-66] or even multiple states.[67, 68, 325] As mentioned in Chapter 1, various external stimuli such as electric field,[42, 56] tunneling electrons,[41, 43-49, 63, 65, 67, 68] light[62, 69] and temperature[70] have been used to trigger the single molecule switching. Regarding the intrinsic properties of the molecules, the molecular switches can be realized in different ways, for example, shifting the atom position of

non-planar molecules, cycling the trans-cis isomerization of azobenzene molecules,[44, 45, 56, 59, 62, 69, 71] flipping the orientation of dipole molecules,[55] manipulating the chirality of enantiomers,[63, 70, 73] controlling the charge states,[48-51, 53] spin states,[64, 65] electronic states of molecules,[66] and modifying the bonding formation.[52, 326]

The VOPc molecule, which possesses a permanent electric dipole moment, represents a very interesting example of a molecular switch. As a nonplanar dipolar molecule, it adopts two distinct configurations on a surface, namely dipole up and dipole down, so its operating mechanism is based on a reversible dipole switching. Support surface also plays a critical role during the single-molecule switching operation. For example, the strong interfacial coupling between the metal surface electrons and the molecule may cause the intrinsic switching properties of the molecules to disappear, or in other cases the lateral electron transport at metal surfaces may lead to nonlocal effects. To minimize the substrate effect, atomically flat and chemically inert graphite is chosen as the substrate to study single molecule switching.

STM has been proved to be a powerful tool for the investigation of single molecular switches on surfaces due to its capability of imaging, manipulating and characterizing of molecules at the atomic-scale. As a complementary technique, STS allows the investigation of molecular electronic structures on a single-molecule scale.[46, 48, 64, 73, 327, 328] Electronic properties of different molecular moieties in a self-assembled nanostructure or even different parts of

a single molecule can be revealed by STS.[328]

In this chapter, we demonstrate the ability of STM to switch of a single VOPc molecule between bistable configurations in self-assembled closely-packed monolayer on graphite. Through the combination of STM measurements and DFT simulations, we assign these two bistable configurations as O-up and O-down configurations. By controlling the polarity of the pulse voltage applied to the tip, VOPc molecules can be switched between O-up and O-down configurations. The switching is confined to the specifically addressed molecules without affecting the adjacent molecules. STS measurements show that the electronic structures of the molecules are sensitive to the dipole orientation.

4.2 Self-Assembled Monolayer and Bilayer VOPc on HOPG

As shown in the schematic in Figure 4.1a, VOPc is a non-planar dipolar molecule. The V-O bond is out-of-plane and the VOPc molecule carries an electric-dipole moment of 2.27 D.[329] Well-ordered VOPc monolayer can be formed by depositing 1ML VOPc on HOPG at RT and subsequent annealing at 380 K for 50 min, as shown in the large scale STM image in Figure 4.1b. The corresponding high resolution image in Figure 4.1c reveals the four-lobe feature of VOPc molecule with a central bright protrusion.[330] In particular, all VOPc molecules adopt the O-up configuration with the molecular π-plane parallel to the graphite surface. The square unit cell of the unidirectionally aligned molecular dipole array of 1.47×1.47 nm^2 is highlighted in Figure 4.1c

and 4.1d.

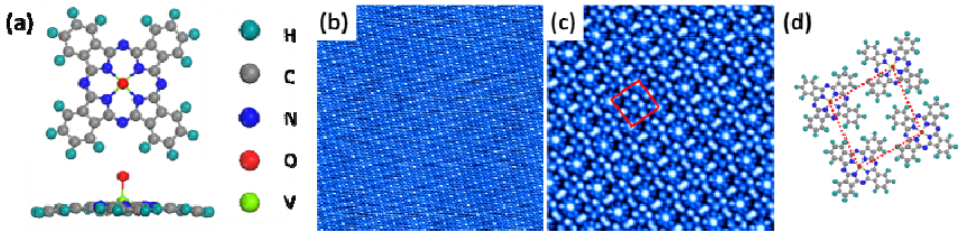

Figure 4.1 (a) Top view and side view of VOPc molecular structure. (b) Large scale (50 × 50 nm^2, V_{tip} = 2.5 V) and (c) corresponding high resolution (10 × 10 nm^2, V_{tip} = 2.5 V) STM images of 1ML VOPc on HOPG. (d) Schematic packing structure of VOPc on HOPG.

Increasing the coverage to 1.5 ML can result in the formation of 2nd layer VOPc molecules. As shown in Figure 4.2 a, the 2nd layer VOPc molecules adopt a four-lobe feature without the center bright protrusion. This indicates that the 2nd layer VOPc adsorb with an O-down configuration. The lateral profile in Figure 4.2b corresponds to the red line in Figure 4.2a. It reveals a height difference of ~0.3nm between the 2nd layer and single layer films, which corresponds to the out-of plane lattice spacing of planar phthalocyanine monolayers with flat-lying configuration.

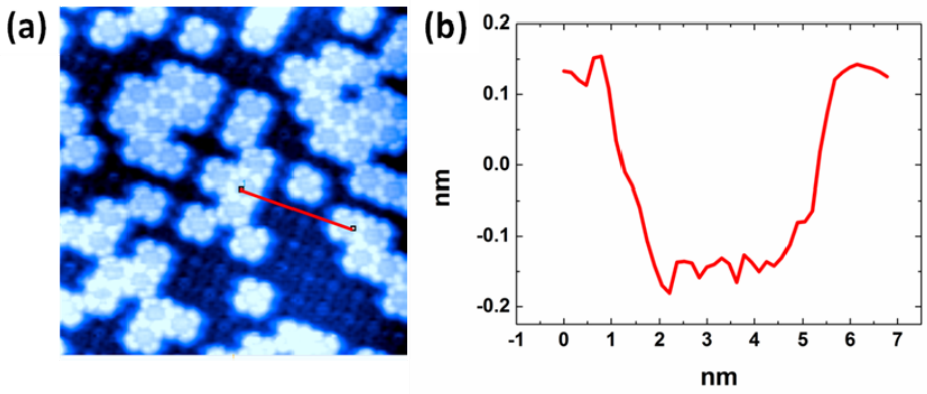

Figure 4.2 (a) STM image of bilayer VOPc on HOPG (20 × 20 nm^2, V_{tip} = -2.598 V). (b) The corresponding line profile between the first layer and second layer.

DFT calculations were also carried out to simulate the O-up and O-down

configurations. In STM simulation, VOPc molecules on single layer graphene were studied and a (1×1) supercell was chosen according to the experimental results. Figure 4.3a-c show the top view, side view of the optimized structures and simulated STM images for O-up configuration on graphene; while Figure 4.3d-f are for the O-down configuration. Both of them are in good agreement with the experimental data.

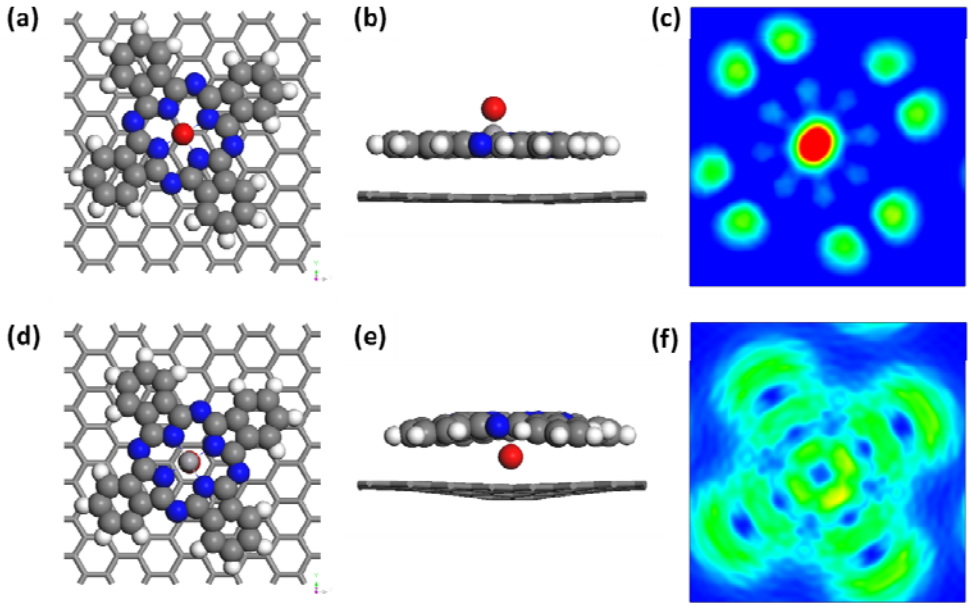

Figure 4.3 (a) Top and (b) side views of the optimized structure and (c) simulated STM image of the O-up configuration. (d) Top and (e) side views of the optimized structure and (f) simulated STM image of the O-down configuration. Simulated STM images are calculated for occupied bands, with the energy range (2.5 eV) in consistent with the experimental bias voltage applied to the tip.

4.3 Single Molecule Switching within Self-Assembled VOPc Monolayer on HOPG

Single molecule switching can be realized in this closely-packed monolayer. To switch a molecule, a voltage pulse was applied to the center of VOPc with opened feedback loop. A sequence of STM induced molecular

switching from O-up to O-down configuration is presented in Figure 4.4.

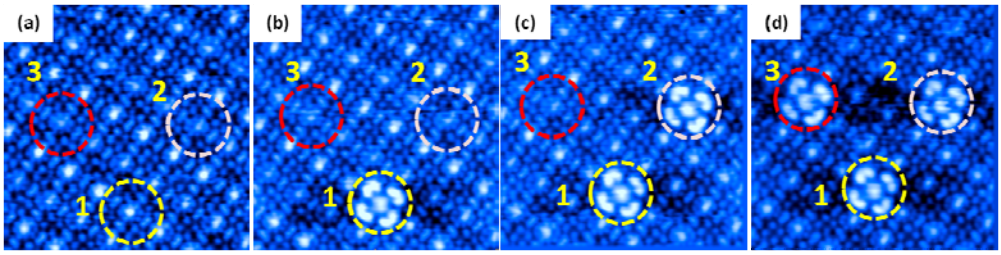

Figure 4.4 A sequence of STM images showing the controlled switching of VOPc molecules from O-up configuration to O-down orientation.(10 × 10 nm^2, V_{tip} = 2.0 V, I_{set} = 100 pA). The molecule indicated by the yellow circle (molecule 1) was switched from O-up (a) to O-down (b) by a positive voltage (+4 V, 5 ms), and then molecule 2 and 3 in the pink and red circle were switched to O-down configuration one by one.

During the pulsing processes, the tip was held at a fixed height above the target molecule by setting V_{tip} = 2.0 V, I_{set} = 100 pA. Initially, the molecule 1 indicated by the yellow circle with the O-up configuration (Figure 4.4a) was switched to a O-down configuration (Figure 4.4b) by applying a positive voltage pulse to the tip (+4 V, 5 ms). The image was then scanned subsequently to confirm the successful switch. Using the same method, molecule 2 and 3 indicated by the pink and red circle were switched to O-down configurations sequentially. It is worth noting that the single molecule switching within the close-packed monolayer is very controllable and localized to the specifically addressed molecules. Careful inspection of the STM images reveals that the neighboring VOPc molecules remain unaffected; at the same time, the in-plane molecular orientation of the switched molecules keeps the same. These observations suggest that the dipole switching process is unlikely to be caused by the molecular flipping.

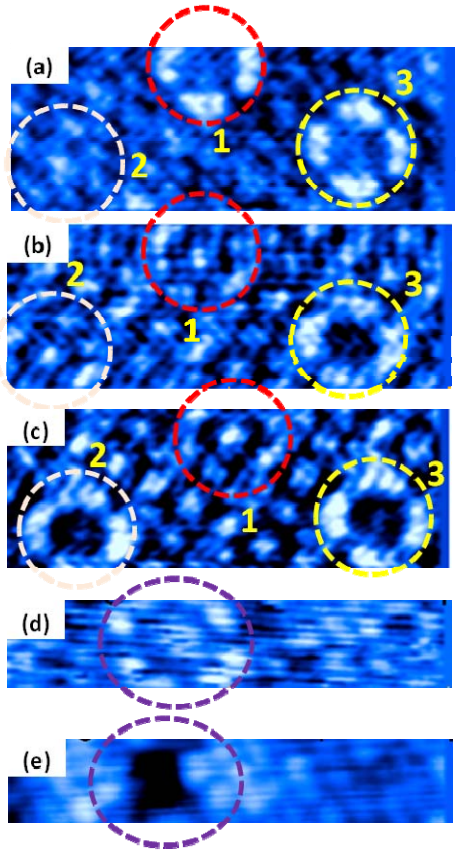

Figure 4.5 (a)–(c) Series of STM image showing the reversible switching between the O-up and O-down configurations (8 × 3 nm^2, V_{tip} = 2.5 V, I_{set} = 100 pA). The molecule indicated by the red circle (molecule 1) was switched from O-down (Figure 4.5a) to O-up configuration (Figure 4.5b) by applying a negative voltage pulse to the tip (-3 V, 5 ms); while molecule 2 indicated by the pink circle was switched from O-up (Figure 4.5b) to O-down configuration (Figure 4.5c) by applying a positive pulse (+4 V, 5 ms). (d)-(e) Desorption of one VOPc molecule from the surface after applying a negative pulse -3 V to the tip (1.2 × 6 nm^2, V_{tip} = 2.5 V, I_{set} = 100 pA).

The reversible switching from O-down to O-up configuration can also be achieved when the bias voltage was inverted. As shown in a series of STM image of Figure 4.5a-c, the molecule 1 denoted by the red circle in Figure 4.5a was switched from O-down to O-up configuration (Figure 4.5b) by applying a negative voltage pulse to the tip (-3 V, 5 ms). Next, the molecule 2 denoted by the pink circle in Figure 4.5b was pulsed by a positive voltage (+4 V, 5 ms), and switched to O-down configuration (Figure 4.5c). Molecule 3 adopted the

O-down configuration during the switching processes and can be used as a marker. The switching from O-down to O-up configuration was less reproducible, as the molecule often desorbed from the surface at higher negative voltage. This low success rate of the reverse process has also been observed in other molecular switches.[41, 73] The STM images in Figure 4.5d-e demonstrate that the VOPc molecule indicated by the purple circle has been desorbed from the surface after applying a negative pulse of -3 V above the molecule.

To understand the mechanism of the dipole orientation switching of the VOPc molecules, we investigated the reaction yield as a function of the pulse voltage. The reaction yield is defined as the number of switching events per injecting electrons.[234] During the statistical analysis of the reaction yield, the tip position was set to V_{tip} = 2.5 V, I_{set} = 100 pA and the pulse voltage was varied from 2 V to 4 V. The threshold voltage for molecular switching from O-up to O-down configuration was 3.5 V; while the reverse switching required a negative voltage around -3 V. We have also analyzed the dependence of switching rate on the tunneling current, which can help to elucidate whether the switching process is triggered by the electric field or inelastically tunneled electrons.

The switching rate was defined as $-[\ln(N/N_0)]/t$, where N_0 refers to the number of O-up molecules applied with positive voltage pulse, N is the number of molecules remaining in the O-up state after the pulse, and t is the

period of the voltage pulse.[234] During the switching rate measurement, the tip was centered above the O-up molecules and a pulse voltage of 4 V was applied to the tip for 5 ms. We note that this pulse voltage is higher than the threshold voltage. If providing with higher tunneling current (>100 pA), the success probability of the switching process is close to 100%. The utilization of 4 V as a pulse voltage can ensure that the switching rate we measured here is only influenced by the tunneling current.

Tunneling current (pA)	**10**	**30**	**40**	**50**	**100**
Switching rate (s^{-1})	**6.25**	**10.25**	**61.07**	**219.72**	**599.14**

Table 4.1 Switching rate as a function of tunneling current (V_{pulse} = 4 V, 5 ms; V_{tip} = 2.5 V).

Table 4.1 shows the measured switching rates at different tunneling current I_{set} with a constant V_{tip} of 2.5 V. By simply increasing the tunneling current from 10 pA to 100 pA, the switching rate increased more than one order of magnitude. We have also recorded the relative tip position corresponding to various tunneling current. It is found that under the same bias voltage of 2.5 V, the relative tip position only changed by 0.077 nm by increasing the I_{set} from 10 pA to 100 pA. This modification of the relative distance between tip and the underlying molecule is too small to have an influence on the electric field between them. Therefore, we conclude that the molecular switching event is

not induced by the electric field. We proposed that the observed reversible switching is most likely triggered by the inelastic electron tunneling process. These tunneling electrons can transfer energy to the molecule to excite the switching process[46] and the possible channel may involve the "shuttling" of O atom between two sides of VOPc molecular plane.

4.4 STS Measurements of VOPc with Different Dipole Orientations

STM images only provide the geometry contrast of the two different configurations. Differences in the electronic structures between the O-up and O-down states can further be verified by STS. The advantage of STS compared with X-ray photoelectron spectroscopy (XPS)[331] and UPS[323, 329] is that it allows the investigation of local density of states of a single molecule or even different parts within a single molecule.[327, 328] In the following, the electronic properties of the two configurations were probed with STS.

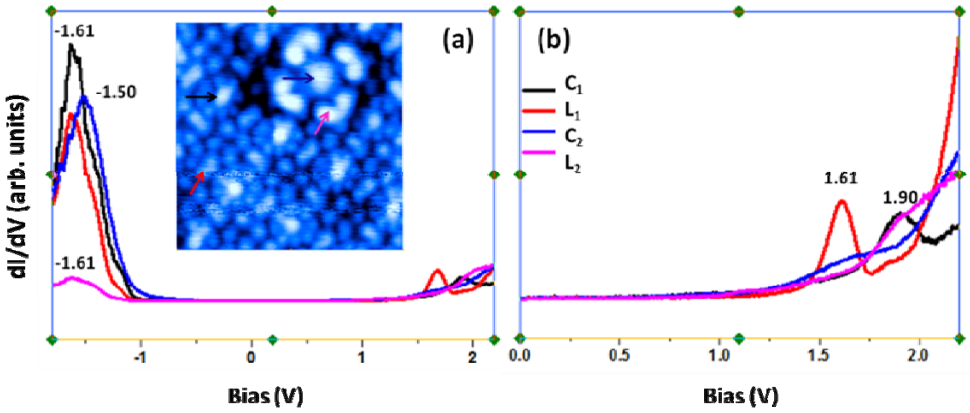

Figure 4.6 (a) dI/dV spectra of both occupied and unoccupied states, taken on O-up and O-down molecules at the key locations indicated by the arrows in the inset (5 × 5 nm^2, V_{tip} = 2 V). (b) dI/dV spectra of the occupied states acquired on O-up and O-down molecules at different locations.

Figure 4.6a shows the typical dI/dV spectra taken at the representative

locations on the O-up and O-down molecules. These locations are indicated by the arrows in the inset, where C_1, L_1 and C_2, L_2 represent the center and lobe of the O-up and O-down molecules respectively. Both occupied and unoccupied states have been obtained. All the dI/dV spectra are average of about 10 curves, where each curve is an average of 40 scans.[331] The shape and position of the spectra are highly reproducible. The spectra from both configurations show a characteristic energy gap of about 2.4 V, deduced from the onset of the electronic states (LUMO and HOMO).[329] We note that for O-up molecules, DOS measured on both center (C_1) and lobe site (L_1) shows a peak at -1.61 V. As our bias voltage is applied to the tip, this peak is ascribed to tunneling into an empty state of the O-up molecule. The case is different for O-down molecules, as revealed by spectra C_2 and L_2 in Figure 4.6a. There is a small shift (0.11 V) of the peak position for the local DOS measured at the center and the lobe of the O-down molecules. The sensitivity of electronic structures to different configurations for molecular adsorption can be demonstrated more clearly through the occupied states of the molecules. Figure 4.6b shows a set of spectra where only the occupied states of the molecules are presented. DOS measured on the center and lobe of the O-up molecule show sharp peaks at 1.90 V and 1.61 V respectively. Whereas for O-down adsorbed molecules, only less pronounced shoulders are observed. A weak but real rise in intensity near 1.6 V and 1.9 V has been detected on the center and lobe of O-down molecule. The dI/dV reflects the DOS for

adsorbate.[332-336] The weak intensity of the band close to the Fermi level can be attributed to increased distance between the molecular π plane and the substrate, which may have influence on the tunneling probability. The orbital-mediated tunneling[281, 337-340] spectra of O-up and O-down configurations are distinctly different and allow these two configurations to be clearly identified.

4.5 Summary

In summary, we have demonstrated that VOPc molecules in a closed-packed monolayer on graphite can be reversibly switched between O-up and O-down configurations. The switching is proposed to be triggered by the inelastically tunneled electrons, which provide energy for the O-atom shuttling between two sides of VOPc molecular plane. The electronic structures of the VOPc with oppositely aligned dipole can be identified by spatially resolved STS. The combination of STM and STS enable the complementary investigations of the adsorption geometry and electronic properties of a single molecule at the surface.

Chapter 5: Reversible Switching of a Single-Dipole Molecule Imbedded in Two Dimensional Hydrogen-Bonded Binary Molecular Networks

5.1 Introduction

In Chapter 4, we demonstrate the single-dipole molecule switching of VOPc within self-assembled VOPc monolayer. We propose that the observed reversible switching is most likely triggered by the inelastic electron tunneling process and the possible channel may involve the "shuttling" of O atom between two sides of VOPc molecular plane. However, we cannot rule out the possibility of the switching via flipping of the molecular plane. Furthermore, up to now, most of the studies of molecular switches were performed either individually or in a self-assembled single-component monolayer. Incorporation of these molecular switches into more complex and rationally designed nanoarchitectures is needed for practical applications. To achieve this, single-molecular switches should be interconnected with other molecules via intermolecular interactions to form desired long-range ordered nanostructures over macroscopic area; at the same time, the molecular functionality responsible for molecular switching must remain intact during the self-assembly process. Self-assembly of binary molecular systems on inert graphite surface via the formation of multiple intermolecular hydrogen bonding represents a versatile approach to fabricating ordered and robust molecular nanostructure arrays. [166, 204, 308] By varying the binary molecular ratio, the interdipole distance of the molecular dipole dot arrays and hence the

dipole densities can be easily tuned with atomic precision.[341] Moreover, the formation of the multiple intermolecular hydrogen bonding can further enhance the structure stability of these molecular nanostructure arrays during the device operation.

In order to test switching channel of the dipole molecule as well as demonstrate the feasibility of manipulating the molecular switches in more complex structures, we use *in-situ* LT-STM to demonstrate for the first time reversible switching of single-dipole molecule ClAlPc imbedded in 2D hydrogen-bonded binary molecular networks formed by co-assembly of ClAlPc and PFP on graphite. By controlling the polarity of the pulse voltage applied to the STM tip, ClAlPc molecules can be switched between dipole-up and dipole-down configurations without affecting the neighboring molecules. As corroborated by DFT calculations, we propose that the switching is achieved by "shuttling" the Cl atom between two sides of the ClAlPc molecular plane.

5.2 Reversible Switching of ClAlPc within PFP:ClAlPc Binary Molecular Networks

Figure 5.1 shows the molecular structures of PFP and ClAlPc molecules. A highly ordered hexagonal binary network was formed after coadsorption of PFP and ClAlPc with a PFP:ClAlPc ratio of 1:2 on HOPG followed by annealing at 370K for 40 min (Figure 5.2a). This hexagonal molecular array is proposed to be stabilized via the formation of multiple intermolecular

C-H···F-C hydrogen bonding between the periphery F atom on PFP and H atoms of neighboring ClAlPc molecules. [273, 308, 341] Figure 5.2b and 5.2c displays the corresponding high-resolution STM images, where the rod-like feature represents a single PFP molecule and the four-lobe feature with a central protrusion represents a single ClAlPc. Careful inspection of the STM image reveals that two ClAlPc molecules are surrounded by

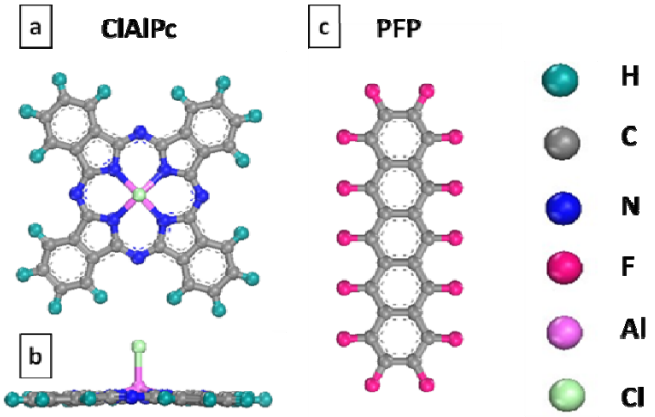

Figure 5.1 (a) Top view and (b) side view of ClAlPc molecular structure. (c) Molecular structure of PFP molecule.

four PFP molecules, forming an oblique unit cell with $a_1 = 2.50$ nm, $b_1 = 2.80$ nm with an included angle $\alpha = 82^{o}$. The corresponding schematic molecular superstructure is given in Figure 5.2d with the dipole density of 2.86×10^{13} dipoles/cm^2. Both PFP and ClAlPc lie flat on HOPG with their conjugated π-plane oriented parallel to the HOPG surface due to interfacial π-π interactions. The bright central protrusion in individual ClAlPc can be assigned to the Cl atom resided on the flat-lying ClAlPc with a Cl-up configuration. [234, 341] As can be seen clearly in Figure 5.2, the directional interfacial π-π interactions can lead to that almost all the ClAlPc molecules

adopting the Cl-up configuration, consistent with previous reports. [234, 329, 341]

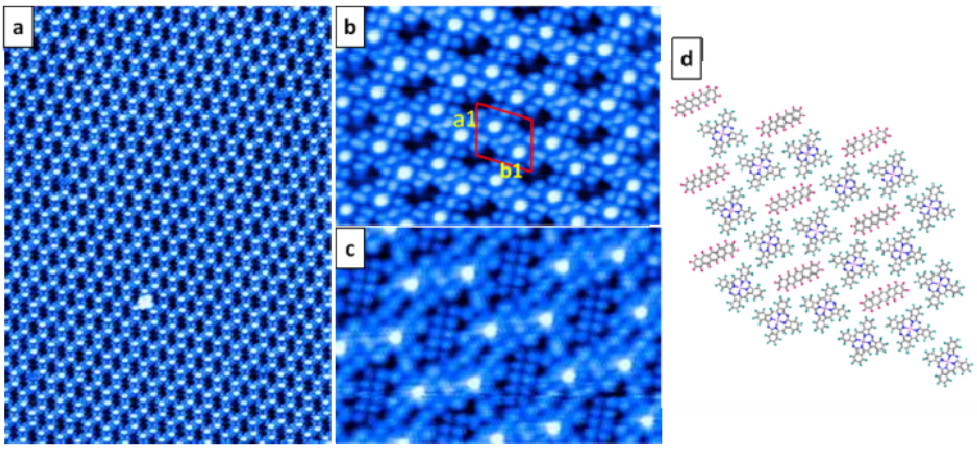

Figure 5.2 (a) STM image (45 × 60 nm^2, V_{tip} = 2.2 V) of long-range ordered hexagonal binary molecular network formed by PFP and ClAlPc with molecular ratio 1:2 on HOPG. Corresponding high resolution STM images of the hexagonal structure: (b) (15 × 10 nm^2, V_{tip} = 1.9 V) and (c) (9 × 6 nm^2, V_{tip} = 2.5 V). (d) Schematic packing structure for the hexagonal network.

Single-molecule switching can be realized in this binary network by positioning the STM tip above the target molecule and subsequently applying a voltage pulse. The image was then scanned subsequently to confirm the successful switch. By controlling the polarity of the voltage applied to the tip, we can switch the ClAlPc molecule between Cl-up and Cl-down configurations reversibly. During the pulsing process, the tip was held at 2.0 V and 100 pA (with the feedback loop off) to fix the tip above the target molecule. ClAlPc molecules can be switched to the desired configurations as clearly shown by the sequential STM images in Figure 5.3a-d. The bistable states of ClAlPc molecule can be discriminated from the molecularly resolved STM images, where the four-lobe feature with a central bright protrusion represents a ClAlPc molecule with Cl-up configuration and the four-lobe feature with a homogeneous brightness is attributed to a Cl-down

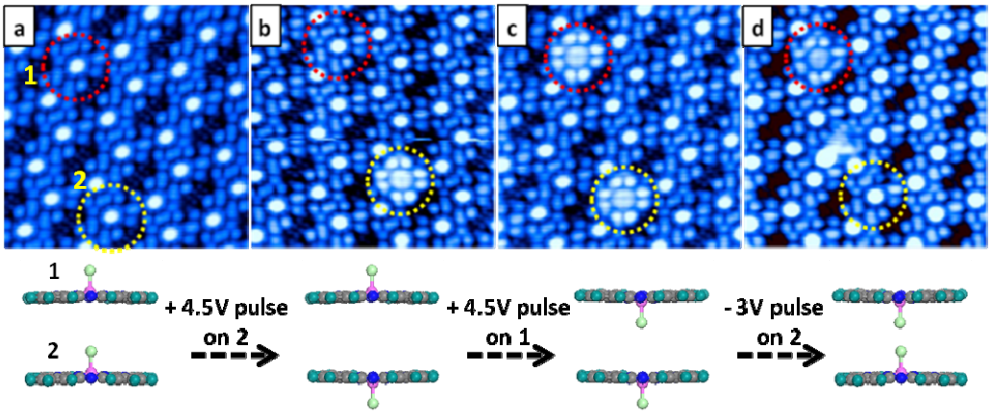

Figure 5.3 (a-d) Sequential STM images showing the reversible switching between the Cl-up and the Cl-down configurations. (10×10 nm^2; $V_{tip} = 2.0$ V, $I_{set} = 100$pA). Molecule indicated by the red circle (molecule 1) was switched from Cl-up (b) to Cl-down (c) by a positive voltage (+4.5 V, 5 ms), and the molecule indicated by the yellow circle (molecule 2) was switched from the Cl-up configuration (a) to the Cl-down configuration (b) by a positive voltage pulse and back to the Cl-up configuration (d) by applying a negative pulse (-3 V, 5 ms). Corresponding schematics demonstrating the switching of molecules 1 and 2 are shown below each STM image.

configuration. Initially, the molecule in the Cl-up configuration (Figure 5.3a), as indicated by a yellow circle, was switched to a down configuration (Figure 5.3b) by applying a positive voltage pulse (4.5 v, 5 ms) to the tip. Subsequently, another molecule in the Cl-up configuration, now denoted by a red circle, was switched to the Cl-down configuration (Figure 5.3c) by applying the same positive voltage pulse. It is worth noting that only the ClAlPc molecule under the STM was switched with the neighboring ClAlPc molecules unaffected, revealing a true single-dipole molecule switching. In addition, the hydrogen-bonded binary molecular network remained unperturbed, confirming the good structural stability of the dipole molecules imbedded in the hydrogen-bonded molecular network. Such dipole molecule switching is highly reversible. The molecule, as denoted by a yellow circle,

which was previously switched from the Cl-up to the Cl-down configuration (Figure 5.3a and 5.3b), can now be switched back to the Cl-up configuration again after applying a negative voltage pulse (-3 V, 5 ms), as evidenced in Figure 5.3d. Again, the negative voltage pulse did not affect the surrounding molecules and the molecular networks. Careful inspection of the STM image reveals that the in-plane orientation of the ClAlPc molecule also remains the same during the switching process.

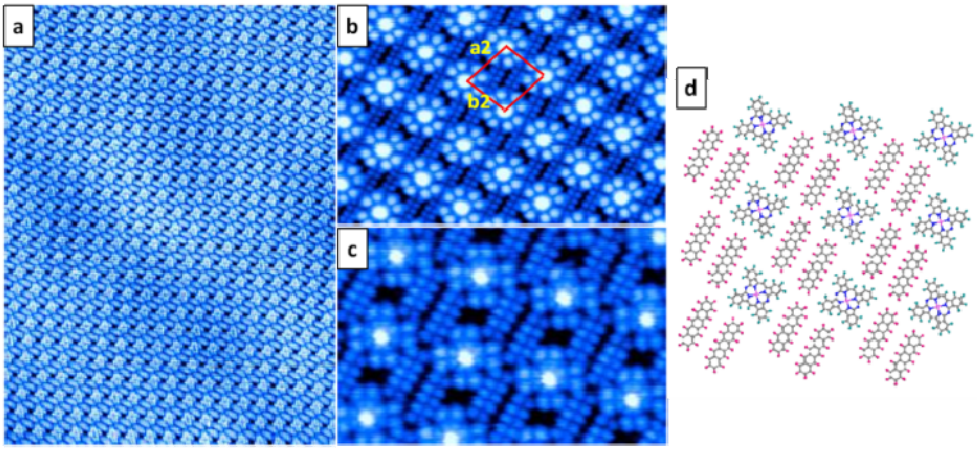

Figure 5.4 (a) STM image (45 × 60 nm^2, V_{tip} = 2.0 V) of long-range ordered "square" binary molecular network formed by PFP and ClAlPc with a binary molecular ratio 2:1 on HOPG. (b) High-resolution STM images of the "square" structure: (15 × 10 nm^2, V_{tip} = 2.5 V) and (c) (9 × 6 nm^2, V_{tip} =2.5 V). (d) Schematic packing structure for the "square" network.

In order to study the influence of the surrounding molecular frame on the single-molecule switches we construct a different binary molecular network by varying the relative molecular ratio. Increasing the molecular ratio of PFP:ClAlPc to 2:1 gave rise to formation of another intriguing binary molecular network. Figure 5.4a shows a highly ordered "square" network after deposition of PFP and ClAlPc on HOPG, followed by annealing at 370K for 30 min. High-resolution STM images (Figure 5.4b, 5.4c) reveal that each PFP

doublet is surrounded by four ClAlPc molecules, forming an oblique unit cell with a_2 = 2.50 nm,b_2 = 2.25 nm, with an included angle of 84°. Both ClAlPc and PFP lie flat on HOPG and almost all the ClAlPc molecules are aligned in the Cl-up configuration. Now, all the ClAlPc molecules are well separated by neighboring PFP molecules, which enables addressing them at single-molecule scale. The schematic of the packing structure is illustrated in Figure 5.4d with the dipole density decreased to 1.78×10^{13} dipoles/cm^2.

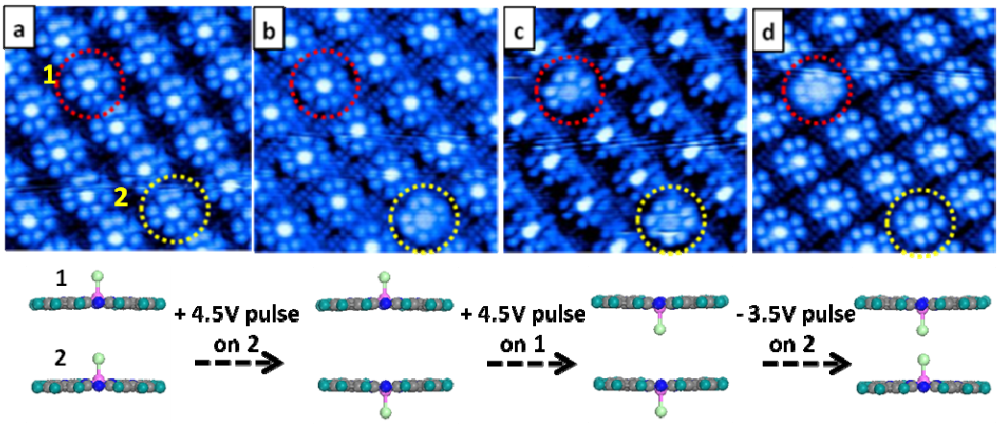

Figure 5.5 (a-d) Sequential STM images showing the reversible switching between the Cl-up and the Cl-down configurations (10 × 10 nm^2; V_{tip} = 2.1, 2.0, 2.0, 2.2 V; I_{set} = 100 pA). Molecule indicated by the red circle (molecule 1) was switched from Cl-up (b) to Cl-down (c) by a positive voltage (+4.5 V, 5 ms), and molecule indicated by the yellow circle (molecule 2) was switched from the Cl-up configuration (a) to the Cl-down configuration (b) by a positive voltage pulse and back to the Cl-up configuration (d) by applying a negative pulse (-3.5 V, 5 ms). Corresponding schematics demonstrating the switching of molecules 1 and 2 are shown below each STM image.

Switching between the Cl-up and Cl-down configurations can also be realized in this "square" network, as shown in Figure 5.5a-d. The molecule indicated by the red circle can be switched from the initial Cl-up configuration (Figure 5.5a, 5.5b) to the Cl-down configuration (Figure 5.5c, 5.5d) by positioning the tip above the target molecule and applying a positive voltage

pulse (4.5 V, 5 ms). The molecule indicated by the yellow circle shows a reversible switching from the Cl-up (Figure 5.5a) to the Cl-down configuration (Figure 5.5b and 5.5c) then back to the Cl-up configuration (Figure 5.5d). The switching direction can be controlled by the polarity of the pulse voltage, with parameters of 4.5 V, 5 ms for Cl-up to Cl-down configurations and -3.5 V, 5 ms for Cl-down to Cl-up configurations, respectively. Similar to the case of PFP:ClAlPc with a ratio of 1:2, both the adjacent molecular network and the in-plane orientation of the switched molecule remain unchanged.

5.3 Reaction Yield of the Single ClAlPc Molecule Switching

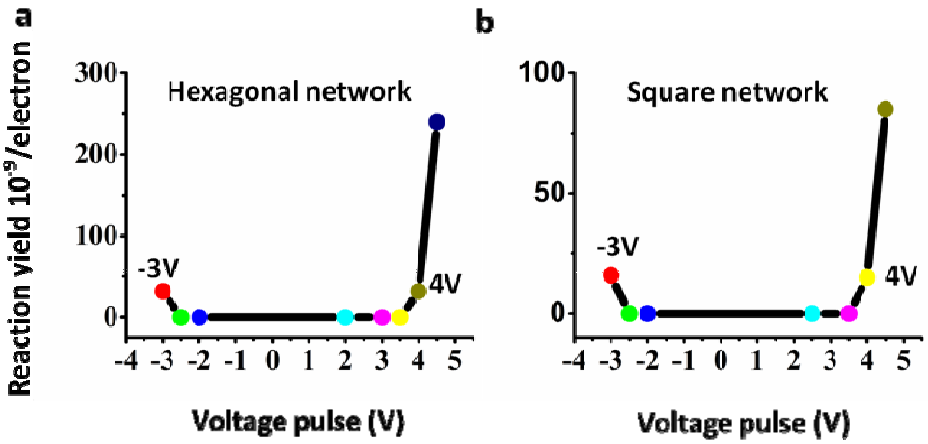

Figure 5.6 Reaction yield as a function of voltage pulse (V_{tip} = 2.5 V, I_{set} = 100 pA, feedback loop off). (a) Plot for the ClAlPc imbedded in the hexagonal network and (b) "square" network. Threshold voltage for switching from the Cl-up to the Cl-down configuration (positive voltage pulse) or the Cl-down to the Cl-up configuration (negative voltage pulse) can be extracted from the plot.

To understand the mechanism of the dipole switching of the ClAlPc molecule imbedded in these hydrogen-bonded binary molecular networks, we statistically analyzed the dependence of the reaction yield on the voltage pulse.

In our experiments, the reaction yield is defined as the number of switching events per injected electron. Figure 5.6 shows the reaction yield as a function of voltage pulse for the hexagonal network (Figure 5.6a) and the "square" network (Figure 5.6b). Switching from the Cl-up to the Cl-down configuration was induced by positive voltage pulse, and we determined the threshold voltage for both the hexagonal and the "square" network to be 4 V. For the reverse switching from the Cl-down to the Cl-up configuration, a negative voltage pulse is used and the corresponding energy onset is around -3 V for both systems. The arrangement of ClAlPc molecule in these two networks results in different number of intermolecular hydrogen bonds; however, the threshold voltage for both systems is the same. This suggests that during the switching process the whole molecular plane remain intact, and the only thing that can change is the location of the Cl atom.

On the basis of previous work for the dipole switching for ClAlPc[234] or other dipole phthalocyanine molecules, [236] two possible mechanisms can be proposed for the reversible switching of individual ClAlPc molecule between two configurations, including the flipping of the dipole molecule or the "shuttling" of the Cl atom between two sides of the ClAlPc molecular plane. In our experiment, the molecular networks are stabilized by the intermolecular C-F…H-C hydrogen bonding between PFP and ClAlPc. The reversible dipole switching observed for ClAlPc molecules exclusively affects the addressed molecule and leaves the neighboring molecular network and in-plane

orientation of the switched molecule unaffected. Although the arrangement and hence the number of hydrogen bonds of ClAlPc imbedded in the hexagonal and "square" networks is different, the threshold voltage for these two systems are the same. All these observations suggest that the dipole switching process is unlikely to be caused by the molecular flipping. Very recently, Gopakumar, T. G et al. investigated a very similar dipole molecule of iron tetraphenylporphyrin chloride (FeTPPCl) adsorbed on Au(111) using LT-STM. [342] They proposed that the two contrasts (bright central protrusion and the dimmed center in FeTPPCl) are due to Cl atom transferred between the Fe center of a selected molecule and the STM tip.[35] In our experiments and a previous report we successfully demonstrated a consecutive switching of a number of ClAlPc molecules (>10 molecules) from the Cl-up to the Cl-down configurations, followed by the reversed switching from the Cl-down to the Cl-up configurations. If the ClAlPc is switched via the Cl-atom transferring between the STM tip and the ClAlPc molecule, the STM tip has to be decorated with a few Cl atoms during this consecutive switching process and hence to greatly affect the following molecular switching process as well as the STM imaging contrast. In our experiments, we can achieve the consecutive switching of different ClAlPc molecules under the exact same switching condition. At the same time, we did not observe any distinct change in the STM imaging contrast during the consecutive molecular switching process. As such, we believe that the reversible ClAlPc switching in our experiments is not

via the Cl-atom transfer mechanism.

5.4 Minimum-Energy Path Revealed by DFT Calculations

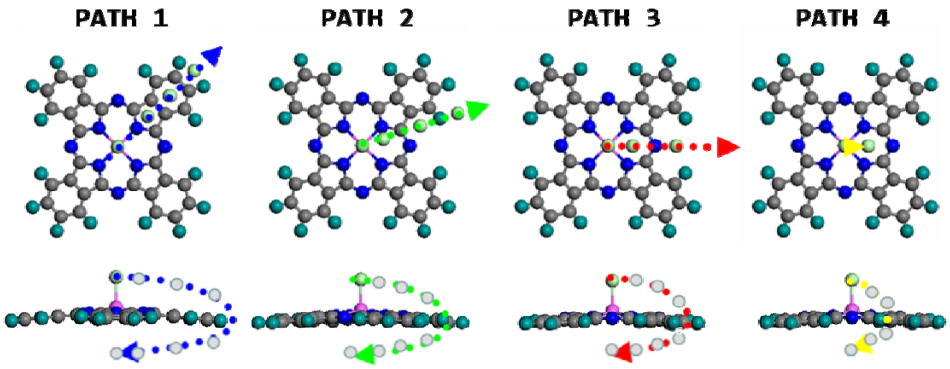

Figure 5.7 (a) Schematic molecular models showing the possible pathways for Cl-atom shuttling from the upper side to the lower side of ClAlPc molecular plane.

On the basis of the experimental results, we propose the "shuttling" of Cl atom between two sides of the ClAlPc molecular plane with the phthalocyanine intact as a possible mechanism to explain how the reversible switching is induced. To reveal the reasonable pathway for Cl-atom shuttling between two sides of the ClAlPc molecular plane, we performed first-principles calculations based on DFT and the nudged-elastic- band (NEB) algorithm was employed to find the minimum-energy path of Cl atom. Four possible paths were proposed by considering the symmetry of the ClAlPc molecule. As shown in Figure 5.7, PATHs 1, 2 and 3 sketch the paths of the Cl atom, where it first moves above the molecular plane along the Al-N1 direction, Al-H1 direction or Al-N2 direction (N1, N2 are the nearest and second nearest N atoms from the center Al atom, and H1 is the nearest H atom from the center), then bypasses the edge of the ClAlPc molecule and finally

bonds to Al atom from another side of the molecular plane; whereas PATH 4 describes the case that the Cl atom "tunnels" through the phthalocyanine core directly to another side of the molecular plane.

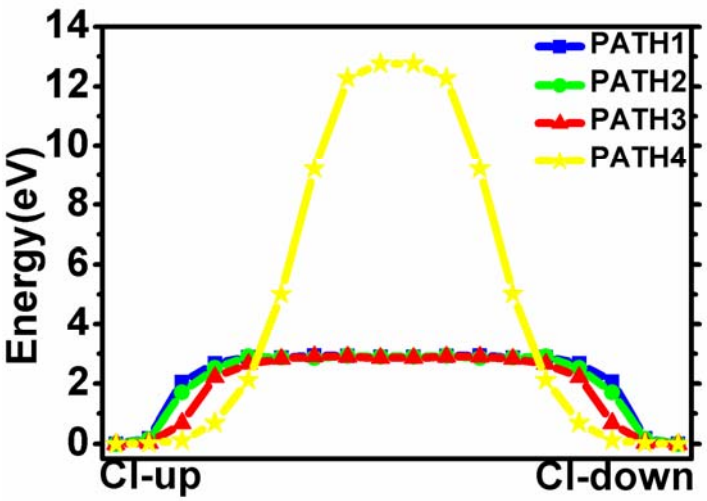

Figure 5.8 Calculated minimum-energy paths for Cl-atom shuttling between two sides of the molecular plane along PATH 1, PATH 2, PATH 3 and PATH 4.

Figure 5.8 shows the calculated minimum-energy paths for these four channels. Along the x axis are 16 intermediate configuration images of a NBE calculation process. The energy barriers for a single switching are found to be 2.93eV (PATH 1), 2.92eV (PATH 2), 2.89eV (PATH 3) and 12.75 eV (PATH 4). By combining the experimentally observed threshold voltage (4 V for Cl-up to Cl-down switching or -3 V for the reversed case) and the calculated results we propose a possible pathway for Cl-atom shuttling between two sides: the inelastically tunneled electrons first induce partial breaking of the Cl-Al bond, the released Cl atom moves from the molecular center to the edge of the molecule following the minimum energy path, then switches to the another side of the molecular plane, and finally bonds with the Al atom. In addition,

due to the lowest calculated energy barrier of PATH 3 and its smaller steric hindrance compared with other pathways, we suggest that Cl atom moving along the Al-N2 direction is the most reasonable pathway. In the experiment, we apply a voltage of 4 V (-3 V) to the tip, which provides ample energy to overcome the energy barrier to move the Cl atom from the molecular center and push (pull) it to the other side. The different threshold voltage between the Cl-up to Cl-down switching and the reverse process may be caused by the asymmetry of the tip-ClAlPc-graphite system.

5.5 Summary

In this chapter, we have demonstrated reversible switching of single-dipole molecule imbedded in two different 2D hydrogen-bonded binary ClAlPc:PFP molecular networks on HOPG. The ClAlPc molecule can be reversibly switched between the Cl-up and the Cl-down configurations by controlling the polarity of the voltage pulse applied to the STM tip. On the basis of experimental results and DFT calculations, we propose that the reversible switching between the Cl-up and the Cl-down configurations is induced by the "shuttling" of the Cl atom between two sides of ClAlPc molecular plane. The switching is spatially confined to the addressed molecule, reversible, controllable and leaves the neighboring binary molecular network unaffected, demonstrating the great potential for applications in molecular high density data storage devices.

Chapter 6: Conclusion and Outlook

6.1 Thesis Summary

In this thesis, we aim to study the molecular self-assembly on surfaces as well as single molecule manipulations within these self-assembled monolayers, with particular emphasis on the single-dipole molecule switching. Three different systems were presented to demonstrate the essential steps required for the molecular switches to have practical applications: understanding the molecular self-assembly processes on surface and hence constructing molecular nanostructure arrays with a high degree of controllability and tunability; featuring the single molecular building blocks with desired functionality; imbedding these functional molecules into more complex networks to immobilize and isolate them in a repetitive and spatially ordered manner. LT-STM was utilized for real-spacing imaging, electronic structure characterization as well as single molecule manipulation. UPS measurements and DFT calculations were also employed to provide complementary information.

For the first part of this work (Chapter 3), in situ LT-STM and UPS were utilized to study the 2D crystallization of C_{60}:pentacene binary system on surfaces. It was found that on Ag(111), three different C_{60} 2D molecular arrays can be fabricated by simply controlling the post-annealing temperature of the binary molecular system. A regular extended 2D nanomesh structure with an ordered nanocavity array was formed when the sample was annealed at 360K

for 30 min. Further annealing this binary molecular system at 370K for 80 min led to the structure transformation from the long range ordered nanomesh structure to the assemblies involving the coexistence of two different types of C_{60} structures, namely C_{60} pair array and C_{60} pentamer array. When the sample was further annealed at 410K for 30 min, the C_{60} pair was completely disappeared and the surface was then dominated by the C_{60} pentamer array. Same self-assembly experiment of C_{60} on the monolayer pentacene covered graphite was also carried out. However, the C_{60} pair array was the only observed superstructures on HOPG even after annealing at different temperatures. This clearly reveals that molecule-substrate interfacial interactions strongly affect the self-assembly processes of the C_{60}:pentacene binary system. UPS has been used to evaluate the nature of C_{60}-pentacene intermolecular interactions. It was found that that the degree of the charge transfer at the C_{60}:pentacene interface is negligible or very small, and hence the interface is dominated by the π-π interaction. Such detailed study allows us to understand that the arrangement of molecules on surfaces is governed by a combination of molecule-substrate interactions and intermolecular interactions. A subtle balance of these interactions can lead to the formation of well-defined supramolecular architectures over macroscopic areas. Moreover, understanding and hence the controlling of the nanostructure at the organic donor-acceptor heterojunction interfaces are also crucial for organic photovoltaic cells.

In chapter 4, a functional dipole molecule VOPc was used as the molecular building block due to the presence of a permanent dipole moment in the molecular center. In order to retain the functionality of the VOPc molecule, self-assembly of VOPc was carried out on inert graphite. Well ordered VOPc monolayer can be formed where all molecules adopt the O-up configuration with the molecular π-plane parallel to the graphite surface. The second layer VOPc adsorbed with an O-down configuration. Single molecule switching can be realized in the closely-packed monolayer. By controlling the polarity of the pulse voltage applied to the tip, VOPc molecules can be switched between O-up and O-down configurations. We have investigated the switching rate as a function of tunneling current. It was found that by simply increasing the tunneling current from 10 pA to 100pA, the switching rate increased more than one order of magnitude. During this process, the change of the electric field between the tip and the underlying molecule was negligible. Hence, we proposed that the molecular switching is most likely triggered by the inelastically tunneled electrons. Differences in the electronic structures between the O-up and O-down states can further be verified by STS. The combination of STM and STS enable the complementary investigations of the adsorption geometry and electronic properties of a single molecule spontaneously. The precise switching of VOPc molecules demonstrates the great potential for applications in ultrahigh density data storage devices.

In chapter 5, we aim to incorporate the single molecular switches into a more complex and rationally designed nanostructure. To achieve this, another single dipole molecule ClAlPc and PFP molecule were selected as the molecular building blocks. To minimize the substrate effect, inert graphite was used as the substrate. In this case, ClAlPc molecules can be interconnected with PFP molecules via multiple intermolecular hydrogen bonds between the periphery H atoms on ClAlPc and the F atom of the neighboring PFP molecules. By varying the binary molecular ratio, the interdipole distance of the molecular dipole dot arrays and hence the dipole densities can be easily tuned with atomic precision. Moreover, formation of multiple intermolecular hydrogen bonding can further enhance the structure stability of these molecular nanostructure arrays during the switching process. A highly ordered hexagonal binary work was formed after coadsorption of PFP and ClAlPc with a PFP:ClAlPc ratio of 1:2 on HOPG followed by annealing at 370K for 40 min. Increasing the molecular ratio of PFP:ClAlPc to 2:1 gave rise to the formation of a highly ordered “square” network. The reversible switching of ClAlPc between Cl-up and Cl-down configurations can be realized in both the hexagonal and the “square” network by controlling the polarity of the voltage pulse applied to the STM tip. The reversible switching observed for ClAlPc molecules exclusively affects the addressed molecule and leaves the neighboring molecular network and in-plane orientation of the switched molecule unaffected. Although the hydrogen bonds of ClAlPc imbedded in the

hexagonal and “square” networks are different, the threshold voltage for these two systems is same. All these observations suggest that the dipole switching process is unlikely to be caused by the molecular flipping. Hence, we propose that the switching is caused by the “shuttling” of the Cl atom between two sides of the ClAlPc plane. DFT and the nudged elastic band (NEB) algorithm were employed to find the minimum-energy-path of the Cl atom. The work described here is a first step towards manipulating a single molecular switch in a binary molecular network and demonstrate the feasibility of wiring the molecular switches into circuits to perform the basic function of electronic devices.

6.2 Future Work

In this thesis, we have studied the molecular self-assembly and reversible switching of single-dipole molecule within the self-assembled monolayers on graphite. Featuring the molecular building blocks with other functionalities, a high level control over their electronic or magnetic states, and equivalently, self-assembly on a very large scale and high tunability, are the key ingredients for their integration into complex molecular devices.

Control over the magnetic moment of a molecule is a key issue in the emerging field of molecular spintronics. However, the studies in the previous works mainly focus on the molecules on metal substrate, where the strong coupling between the molecule and the substrate can greatly modify the intrinsic properties of the molecular spin system.[237, 343, 344] When an external

stimulus is applied to manipulate the spin state of the molecule, both the molecule-substrate interaction and response of the molecule to the external stimuli will contribute to the final state of the molecule, which will complicate the switching process and confuse the understanding of the switching mechanism.[96] To reduce the interaction between the molecule and the substrate, it is desirable to study single spin manipulation on inert substrate, which has been rarely addressed so far.

In addition, instead of simply using the tunneling electrons from the STM tip as the stimuli, gas molecules can be used in company with STM to manipulate the molecular electronic state at both ensembles of molecules and single-molecule level. In metal-phthalocyanines and metal-porphyrins, the metal center is usually coordinatively unsaturated and presents a local reactive site.[75, 76, 96-99] By axial coordination of small molecules to the metal center, their electronic properties can be substantially altered. Reversible control of individual molecule can be achieved through attachment and detachment of gas molecule. The ensemble of the molecules on the surface can be set to one state by gas exposure, and the desired information can be encoded on this monolayer by STM single molecule manipulation to switch the selected molecule to another state. This opens up new avenue of broader applications, both in gas sensors and high density data storage devices.

Bibliography

[1] A. Aviram and M. A. Ratner, Chem. Phys. Lett. **29**, 277 (1974).

[2] M. A. Reed, C. Zhou, C. J. Muller, T. P. Burgin, and J. M. Tour, Science **278**, 252 (1997).

[3] M. Di Ventra, S. T. Pantelides, and N. D. Lang, Phys. Rev. Lett. **84**, 979 (2000).

[4] R. H. M. Smit, Y. Noat, C. Untiedt, N. D. Lang, M. C. van Hemert, and J. M. van Ruitenbeek, Nature **419**, 906 (2002).

[5] J. Reichert, R. Ochs, D. Beckmann, H. B. Weber, M. Mayor, and H. v. Löhneysen, Phys. Rev. Lett. **88**, 176804 (2002).

[6] B. Xu and N. J. Tao, Science **301**, 1221 (2003).

[7] L. Venkataraman, J. E. Klare, C. Nuckolls, M. S. Hybertsen, and M. L. Steigerwald, Nature **442**, 904 (2006).

[8] S. Y. Quek, M. Kamenetska, M. L. Steigerwald, H. J. Choi, S. G. Louie, M. S. Hybertsen, J. B. Neaton, and L. Venkataraman, Nat. Nanotechnol. **4**, 230 (2009).

[9] I. Díez-Pérez, J. Hihath, Y. Lee, L. Yu, L. Adamska, M. A. Kozhushner, I. I. Oleynik, and N. Tao, Nat. Chem. **1**, 635 (2009).

[10] H. Vazquez, R. Skouta, S. Schneebeli, M. Kamenetska, R. Breslow, L. Venkataraman, and M. S. Hybertsen, Nat. Nanotechnol. **7**, 663 (2012).

[11] B. Xu, X. Xiao, and N. J. Tao, J. Am. Chem. Soc. **125**, 16164 (2003).

[12] D. R. Ward, N. J. Halas, J. W. Ciszek, J. M. Tour, Y. Wu, P. Nordlander, and D. Natelson, Nano Lett. **8**, 919 (2008).

[13] G. Binnig and H. Rohrer, IBM J. Res. Dev. **44**, 279 (2000).

[14] F. J. Giessibl, Rev. Mod. Phys. **75**, 949 (2003).

[15] N. J. Tao, Nat. Nanotechnol. **1**, 173 (2006).

[16] Y. Selzer and D. L. Allara, Ann. Rev. Phys. Chem. **57**, 593 (2006).

[17] C. Joachim and M. A. Ratner, Proc. Natl. Acad. Sci. **102**, 8801 (2005).

[18] S. V. Aradhya and L. Venkataraman, Nat. Nanotechnol. **8**, 399 (2013).

[19] Nat. Nanotechnol. **8**, 377 (2013).

[20] M. Ratner, Nat. Nanotechnol. **8**, 378 (2013).

[21] E. Lortscher, Nat. Nanotechnol. **8**, 381 (2013).

[22] Nat. Nanotechnol. **8**, 385 (2013).

[23] M. Galperin and A. Nitzan, Phys. Chem. Chem. Phys. **14**, 9421 (2012).

[24] Z. Liu, S.-Y. Ding, Z.-B. Chen, X. Wang, J.-H. Tian, J. R. Anema, X.-S. Zhou, D.-Y. Wu, B.-W. Mao, X. Xu, B. Ren, and Z.-Q. Tian, Nat. Commun. **2**, 305 (2011).

[25] G. Hoffmann, L. Libioulle, and R. Berndt, Phys. Rev. B **65**, 212107 (2002).

[26] H. L. Tierney, C. J. Murphy, A. D. Jewell, A. E. Baber, E. V. Iski, H. Y. Khodaverdian, A. F. McGuire, N. Klebanov, and E. C. H. Sykes, Nat. Nanotechnol. **6**, 625 (2011).

[27] T. Kudernac, N. Ruangsupapichat, M. Parschau, B. Macia, N. Katsonis, S. R. Harutyunyan, K.-H. Ernst, and B. L. Feringa, Nature **479**, 208 (2011).

[28] L. Grill, K.-H. Rieder, F. Moresco, G. Rapenne, S. Stojkovic, X. Bouju, and C. Joachim, Nat. Nanotechnol. **2**, 95 (2007).

[29] S. Sanvito, Chem. Soc. Rev. **40**, 3336 (2011).

[30] W. Liang, M. P. Shores, M. Bockrath, J. R. Long, and H. Park, Nature **417**, 725

(2002).

[31] L. Bogani and W. Wernsdorfer, Nat. Mater. **7**, 179 (2008).

[32] H. B. Heersche, et al., Phys. Rev. Lett. **96**, 206801 (2006).

[33] E. A. Osorio, K. Moth-Poulsen, H. S. J. van der Zant, J. Paaske, P. Hedegård, K. Flensberg, J. Bendix, and T. Bjørnholm, Nano Lett. **10**, 105 (2009).

[34] S. Schmaus, A. Bagrets, Y. Nahas, T. K. Yamada, A. Bork, M. Bowen, E. Beaurepaire, F. Evers, and W. Wulfhekel, Nat. Nanotechnol. **6**, 185 (2011).

[35] C. Iacovita, M. V. Rastei, B. W. Heinrich, T. Brumme, J. Kortus, L. Limot, and J. P. Bucher, Phys. Rev. Lett. **101**, 116602 (2008).

[36] R. Vincent, S. Klyatskaya, M. Ruben, W. Wernsdorfer, and F. Balestro, Nature **488**, 357 (2012).

[37] A. R. Rocha, V. M. Garcia-suarez, S. W. Bailey, C. J. Lambert, J. Ferrer, and S. Sanvito, Nat. Mater. **4**, 335 (2005).

[38] G. Guillaud, J. Simon, and J. P. Germain, Coord. Chem. Rev. **178–180, Part 2**, 1433 (1998).

[39] N. A. Rakow and K. S. Suslick, Nature **406**, 710 (2000).

[40] F. I. Bohrer, A. Sharoni, C. Colesniuc, J. Park, I. K. Schuller, A. C. Kummel, and W. C. Trogler, J. Am. Chem. Soc.**129**, 5640 (2007).

[41] T. G. Gopakumar, H. Tang, J. Morillo, and R. Berndt, J. Am. Chem. Soc. **134**, 11844 (2012).

[42] X. H. Qiu, G. V. Nazin, and W. Ho, Phys. Rev. Lett. **93**, 196806 (2004).

[43] P. Liljeroth, J. Repp, and G. Meyer, Science **317**, 1203 (2007).

[44] J. Henzl, M. Mehlhorn, H. Gawronski, K.-H. Rieder, and K. Morgenstern, Angew. Chem. Int. Ed. **45**, 603 (2006).

[45] B.-Y. Choi, S.-J. Kahng, S. Kim, H. Kim, H. W. Kim, Y. J. Song, J. Ihm, and Y. Kuk, Phys. Rev. Lett. **96**, 156106 (2006).

[46] Y. Wang, J. r. Kröger, R. Berndt, and W. A. Hofer, J. Am. Chem. Soc. **131**, 3639 (2009).

[47] N. Pavliček, B. Fleury, M. Neu, J. Niedenführ, C. Herranz-Lancho, M. Ruben, and J. Repp, Phys. Rev. Lett. **108**, 086101 (2012).

[48] T. Leoni, O. Guillermet, H. Walch, V. Langlais, A. Scheuermann, J. Bonvoisin, and S. Gauthier, Phys. Rev. Lett. **106**, 216103 (2011).

[49] S. W. Wu, N. Ogawa, and W. Ho, Science **312**, 1362 (2006).

[50] Y.-S. Fu, T. Zhang, S.-H. Ji, X. Chen, X.-C. Ma, J.-F. Jia, and Q.-K. Xue, Phys. Rev. Lett. **103**, 257202 (2009).

[51] I. Swart, T. Sonnleitner, and J. Repp, Nano Lett. **11**, 1580 (2011).

[52] F. Mohn, J. Repp, L. Gross, G. Meyer, M. S. Dyer, and M. Persson, Phys. Rev. Lett. **105**, 266102 (2010).

[53] J. Repp, G. Meyer, F. E. Olsson, and M. Persson, Science **305**, 493 (2004).

[54] Z. J. Donhauser, B. A. Mantooth, K. F. Kelly, L. A. Bumm, J. D. Monnell, J. J. Stapleton, D. W. Price Jr., A. M. Rawlett, D. L. Allara, J. M. Tour, and P. S. Weiss, Science **292**, 2303 (2001).

[55] H. Yanagi, K. Ikuta, H. Mukai, and T. Shibutani, Nano Lett. **2**, 951 (2002).

[56] M. Alemani, M. V. Peters, S. Hecht, K.-H. Rieder, F. Moresco, and L. Grill, J. Am.

Chem. Soc. **128**, 14446 (2006).

[57] C. P. Collier, G. Mattersteig, E. W. Wong, Y. Luo, K. Beverly, J. Sampaio, F. M. Raymo, J. F. Stoddart, and J. R. Heath, Science **289**, 1172 (2000).

[58] M. Lastapis, M. Martin, D. Riedel, L. Hellner, G. Comtet, and G. Dujardin, Science **308**, 1000 (2005).

[59] G. Pace, V. Ferri, C. Grave, M. Elbing, C. von Hänisch, M. Zharnikov, M. Mayor, M. A. Rampi, and P. Samorì, Proc. Natl. Acad. Sci. **104**, 9937 (2007).

[60] F. Moresco, G. Meyer, K.-H. Rieder, H. Tang, A. Gourdon, and C. Joachim, Phys. Rev. Lett. **86**, 672 (2001).

[61] V. Iancu, A. Deshpande, and S.-W. Hla, Nano Lett. **6**, 820 (2006).

[62] M. J. Comstock, N. Levy, A. Kirakosian, J. Cho, F. Lauterwasser, J. H. Harvey, D. A. Strubbe, J. M. J. Fréchet, D. Trauner, S. G. Louie, and M. F. Crommie, Phys. Rev. Lett. **99**, 038301 (2007).

[63] M. Parschau, D. Passerone, K.-H. Rieder, H. J. Hug, and K.-H. Ernst, Angew. Chem. Int. Ed. **48**, 4065 (2009).

[64] T. Miyamachi, M. Gruber, V. Davesne, M. Bowen, S. Boukari, L. Joly, F. Scheurer, G. Rogez, T. K. Yamada, P. Ohresser, E. Beaurepaire, and W. Wulfhekel, Nat. Commun. **3**, 938 (2012).

[65] T. G. Gopakumar, F. Matino, H. Naggert, A. Bannwarth, F. Tuczek, and R. Berndt, Angew. Chem. Int. Ed. **51**, 6262 (2012).

[66] C. Uhlmann, I. Swart, and J. Repp, Nano Lett. **13**, 777 (2013).

[67] V. Iancu and S.-W. Hla, Proc. Natl. Acad. Sci. **103**, 13718 (2006).

[68] W. Auwarter, K. Seufert, F. Bischoff, D. Ecija, S. Vijayaraghavan, S. Joshi, F. Klappenberger, N. Samudrala, and J. V. Barth, Nat. Nanotechnol. **7**, 41 (2012).

[69] M. J. Comstock, D. A. Strubbe, L. Berbil-Bautista, N. Levy, J. Cho, D. Poulsen, J. M. J. Fréchet, S. G. Louie, and M. F. Crommie, Phys. Rev. Lett. **104**, 178301 (2010).

[70] S. Weigelt, C. Busse, L. Petersen, E. Rauls, B. Hammer, K. V. Gothelf, F. Besenbacher, and T. R. Linderoth, Nat. Mater. **5**, 112 (2006).

[71] K. Morgenstern, Acc. Chem. Res. **42**, 213 (2009).

[72] S. W. Wu, N. Ogawa, G. V. Nazin, and W. Ho, J. Phys. Chem. C **112**, 5241 (2008).

[73] Y.-S. Fu, J. Schwöbel, S.-W. Hla, A. Dilullo, G. Hoffmann, S. Klyatskaya, M. Ruben, and R. Wiesendanger, Nano Lett. **12**, 3931 (2012).

[74] J. L. Zhang, T. C. Niu, A. T. S. Wee, and W. Chen, Phys. Chem. Chem. Phys. **15**, 12414 (2013).

[75] L. Liu, K. Yang, Y. Jiang, B. Song, W. Xiao, L. Li, H. Zhou, Y. Wang, S. Du, M. Ouyang, W. A. Hofer, A. H. C. Neto, and H.-J. Gao, Sci. Rep. **3**, 1210 (2013).

[76] A. Stróżecka, M. Soriano, J. I. Pascual, and J. J. Palacios, Phys. Rev. Lett. **109**, 147202 (2012).

[77] M. del Valle, R. Gutierrez, C. Tejedor, and G. Cuniberti, Nat. Nanotechnol. **2**, 176 (2007).

[78] M. Wolf and P. Tegeder, Surf. Sci. **603**, 1506 (2009).

[79] R. D. Ramsier and J. T. Yates Jr, Surf. Sci. Rep. **12**, 246 (1991).

[80] J. W. Gadzuk and C. W. Clark, J. Chem. Phys. **91**, 3174 (1989).

[81] J. A. Misewich, T. F. Heinz, and D. M. Newns, Phys. Rev. Lett. **68**, 3737 (1992).

[82] J. W. Gadzuk, Phys. Rev. B **44**, 13466 (1991).
[83] T. Komeda, Prog. Surf. Sci. **78**, 41 (2005).
[84] L. Grill, J. Phys.: Condens. Matter. **20**, 053001 (2008).
[85] S.-W. Hla and K.-H. Rieder, Ann. Rev. Phys. Chem. **54**, 307 (2003).
[86] L. Bartels, G. Meyer, K. H. Rieder, D. Velic, E. Knoesel, A. Hotzel, M. Wolf, and G. Ertl, Phys. Rev. Lett. **80**, 2004 (1998).
[87] B. C. Stipe, M. A. Rezaei, W. Ho, S. Gao, M. Persson, and B. I. Lundqvist, Phys. Rev. Lett. **78**, 4410 (1997).
[88] T. Komeda, Y. Kim, M. Kawai, B. N. J. Persson, and H. Ueba, Science **295**, 2055 (2002).
[89] B. C. Stipe, M. A. Rezaei, and W. Ho, Phys. Rev. Lett. **81**, 1263 (1998).
[90] T. Komeda, Y. Kim, Y. Fujita, Y. Sainoo, and M. Kawai, J. Chem. Phys. **120**, 5347 (2004).
[91] L. Chen, H. Li, and A. T. S. Wee, ACS Nano **3**, 3684 (2009).
[92] R. E. Palmer, Prog. Surf. Sci. **41**, 51 (1992).
[93] M. F. Perutz, Nature **228**, 726 (1970).
[94] K. J. Albert, N. S. Lewis, C. L. Schauer, G. A. Sotzing, S. E. Stitzel, T. P. Vaid, and D. R. Walt, Chem. Rev. **100**, 2595 (2000).
[95] J. D. Wright, Prog. Surf. Sci. **31**, 1 (1989).
[96] K. Flechtner, A. Kretschmann, H.-P. Steinrück, and J. M. Gottfried, J. Am. Chem. Soc. **129**, 12110 (2007).
[97] W. Hieringer, K. Flechtner, A. Kretschmann, K. Seufert, W. Auwärter, J. V. Barth, A. Görling, H.-P. Steinrück, and J. M. Gottfried, J. Am. Chem. Soc. **133**, 6206 (2011).
[98] J. Miguel, C. F. Hermanns, M. Bernien, A. Krüger, and W. Kuch, J. Phys. Chem. C **2**, 1455 (2011).
[99] C. Isvoranu, B. Wang, E. Ataman, J. Knudsen, K. Schulte, J. N. Andersen, M.-L. Bocquet, and J. Schnadt, J. Phys. Chem. C **115**, 24718 (2011).
[100] C. Wäckerlin, D. Chylarecka, A. Kleibert, K. Müller, C. Iacovita, F. Nolting, T. A. Jung, and N. Ballav, Nat. Commun. **1**, 61 (2010).
[101] I. Mochida, K. Suetsugu, H. Fujitsu, and K. Takeshita, J. Phys. Chem. **87**, 1524 (1983).
[102] S.-W. Hla, J. Vac. Sci. Technol. B **23**, 1351 (2005).
[103] D. M. Elgler and E. K. Schweizer, Nature **344**, 524 (1990).
[104] D. G. de Oteyza, P. Gorman, Y.-C. Chen, S. Wickenburg, A. Riss, D. J. Mowbray, G. Etkin, Z. Pedramrazi, H.-Z. Tsai, and A. Rubio, Science **340**, 1434 (2013).
[105] R. A. van Delden, M. K. J. ter Wiel, M. M. Pollard, J. Vicario, N. Koumura, and B. L. Feringa, Nature **437**, 1337 (2005).
[106] J. V. Hernández, E. R. Kay, and D. A. Leigh, Science **306**, 1532 (2004).
[107] U. G. E. Perera, F. Ample, H. Kersell, Y. Zhang, G. Vives, J. Echeverria, M. Grisolia, G. Rapenne, C. Joachim, and S-W. Hla, Nat. Nanotechnol. **8**, 46 (2013).
[108] S. J. v. d. Molen and P. Liljeroth, J. Phys.: Condens. Matter. **22**, 133001 (2010).
[109] J. R. Friedman, M. P. Sarachik, J. Tejada, and R. Ziolo, Phys. Rev. Lett. **76**, 3830 (1996).
[110] L. Lecren, W. Wernsdorfer, Y.-G. Li, O. Roubeau, H. Miyasaka, and R. Clérac, J. Am.

Chem. Soc. **127**, 11311 (2005).

[111] J. Park, A. N. Pasupathy, J. I. Goldsmith, C. Chang, Y. Yaish, J. R. Petta, M. Rinkoski, J. P. Sethna, H. D. Abruña, P. L. McEuen, and D. C. Ralph, Nature **417**, 722 (2002).

[112] G.-H. Kim and T.-S. Kim, Phys. Rev. Lett. **92**, 137203 (2004).

[113] T. Komeda, H. Isshiki, J. Liu, Y.-F. Zhang, N. Lorente, K. Katoh, B. K. Breedlove, and M. Yamashita, Nat. Commun. **2**, 217 (2011).

[114] F. E. Olsson, S. Paavilainen, M. Persson, J. Repp, and G. Meyer, Phys. Rev. Lett. **98**, 176803 (2007).

[115] J. A. A. W. Elemans, S. Lei, and S. De Feyter, Angew. Chem. Int. Ed. **48**, 7298 (2009).

[116] C. D. Dimitrakopoulos and P. R. L. Malenfant, Adv. Mater. **14**, 99 (2002).

[117] V. Coropceanu, J. Cornil, D. A. da Silva Filho, Y. Olivier, R. Silbey, and J.-L. Brédas, Chem. Rev. **107**, 926 (2007).

[118] C. Joachim and M. A. Ratner, Proc. Natl. Acad. Sci. **102**, 8801 (2005).

[119] C. Joachim, J. K. Gimzewski, and A. Aviram, Nature **408**, 541 (2000).

[120] A. Nitzan and M. A. Ratner, Science **300**, 1384 (2003).

[121] R. L. Carroll and C. B. Gorman, Angew. Chem. Int. Ed. **41**, 4378 (2002).

[122] T. J. Park, S. Y. Lee, S. J. Lee, J. P. Park, K. S. Yang, K.-B. Lee, S. Ko, J. B. Park, T. Kim, S. K. Kim, Y. B. Shin, B. H. Chung, S.-J. Ku, D. H. Kim, and I. S. Choi, Anal. Chem. **78**, 7197 (2006).

[123] N. L. Rosi and C. A. Mirkin, Chem. Rev. **105**, 1547 (2005).

[124] J. C. Smith, K.-B. Lee, Q. Wang, M. G. Finn, J. E. Johnson, M. Mrksich, and C. A. Mirkin, Nano Lett. **3**, 883 (2003).

[125] N. A. A. Zwaneveld, R. m. Pawlak, M. Abel, D. Catalin, D. Gigmes, D. Bertin, and L. Porte, J. Am. Chem. Soc. **130**, 6678 (2008).

[126] S. Weigelt, C. Busse, C. Bombis, M. M. Knudsen, K. V. Gothelf, T. Strunskus, C. Wöll, M. Dahlbom, B. Hammer, E. Lægsgaard, F. Besenbacher, and T. R. Linderoth, Angew. Chem. Int. Ed. **46**, 9227 (2007).

[127] D. F. Perepichka and F. Rosei, Science **323**, 216 (2009).

[128] L. Grill, M. Dyer, L. Lafferentz, M. Persson, M. V. Peters, and S. Hecht, Nat. Nanotechnol. **2**, 687 (2007).

[129] M. Treier, N. V. Richardson, and R. Fasel, J. Am. Chem. Soc. **130**, 14054 (2008).

[130] A. Gourdon, Angew. Chem. Int. Ed. **47**, 6950 (2008).

[131] J. V. Barth, J. Weckesser, C. Cai, P. Günter, L. Bürgi, O. Jeandupeux, and K. Kern, Angew. Chem. Int. Ed. **39**, 1230 (2000).

[132] J. V. Barth, J. Weckesser, G. Trimarchi, M. Vladimirova, A. De Vita, C. Cai, H. Brune, P. Günter, and K. Kern, J. Am. Chem. Soc. **124**, 7991 (2002).

[133] A. Dmitriev, N. Lin, J. Weckesser, J. V. Barth, and K. Kern, J. Phys. Chem. B **106**, 6907 (2002).

[134] S. Griessl, M. Lackinger, M. Edelwirth, M. Hietschold, and W. M. Heckl, Single Mol. **3**, 25 (2002).

[135] J. A. Theobald, N. S. Oxtoby, M. A. Phillips, N. R. Champness, and P. H. Beton, Nature **424**, 1029 (2003).

[136] J. Weckesser, A. De Vita, J. V. Barth, C. Cai, and K. Kern, Phys. Rev. Lett. **87**,

096101 (2001).

[137] T. Huang, Z. Hu, A. Zhao, H. Wang, B. Wang, J. Yang, and J. G. Hou, J. Am. Chem. Soc. **129**, 3857 (2007).

[138] G. Pawin, K. L. Wong, K.-Y. Kwon, and L. Bartels, Science **313**, 961 (2006).

[139] J. A. Theobald, N. S. Oxtoby, N. R. Champness, P. H. Beton, and T. J. S. Dennis, Langmuir **21**, 2038 (2005).

[140] L. M. A. Perdigão, E. W. Perkins, J. Ma, P. A. Staniec, B. L. Rogers, N. R. Champness, and P. H. Beton, J. Phys. Chem. B **110**, 12539 (2006).

[141] P. A. Staniec, L. M. A. Perdigão, A. Saywell, N. R. Champness, and P. H. Beton, ChemPhysChem **8**, 2177 (2007).

[142] T. Yokoyama, S. Yokoyama, T. Kamikado, Y. Okuno, and S. Mashiko, Nature **413**, 619 (2001).

[143] J. C. Swarbrick, B. L. Rogers, N. R. Champness, and P. H. Beton, J. Phys. Chem. B **110**, 6110 (2006).

[144] L. M. A. Perdigao, N. R. Champness, and P. H. Beton, Chem. Commun., 538 (2006).

[145] R. Otero, M. Schöck, L. M. Molina, E. Lægsgaard, I. Stensgaard, B. Hammer, and F. Besenbacher, Angew. Chem. Int. Ed. **44**, 2270 (2005).

[146] J. Schnadt, E. Rauls, W. Xu, R. T. Vang, J. Knudsen, E. Lægsgaard, Z. Li, B. Hammer, and F. Besenbacher, Phys. Rev. Lett. **100**, 046103 (2008).

[147] Y. Wang, M. Lingenfelder, T. Classen, G. Costantini, and K. Kern, J. Am. Chem. Soc. **129**, 15742 (2007).

[148] R. Otero, M. Lukas, R. E. A. Kelly, W. Xu, E. Lægsgaard, I. Stensgaard, L. N. Kantorovich, and F. Besenbacher, Science **319**, 312 (2008).

[149] A. Llanes-Pallas, M. Matena, T. Jung, M. Prato, M. Stöhr, and D. Bonifazi, Angew. Chem. Int. Ed. **47**, 7726 (2008).

[150] M. Stöhr, M. Wahl, H. Spillmann, L. H. Gade, and T. A. Jung, Small **3**, 1336 (2007).

[151] J. Ma, B. L. Rogers, M. J. Humphry, D. J. Ring, G. Goretzki, N. R. Champness, and P. H. Beton, J. Phys. Chem. B **110**, 12207 (2006).

[152] P. A. Staniec, L. M. A. Perdigão, B. L. Rogers, N. R. Champness, and P. H. Beton, J. Phys. Chem. C **111**, 886 (2006).

[153] M. E. Cañas-Ventura, W. Xiao, D. Wasserfallen, K. Müllen, H. Brune, J. V. Barth, and R. Fasel, Angew. Chem. Int. Ed. **46**, 1814 (2007).

[154] F. Silly, A. Q. Shaw, M. R. Castell, and G. A. D. Briggs, Chem. Commun., 1907 (2008).

[155] U. K. Weber, V. M. Burlakov, L. M. A. Perdigão, R. H. J. Fawcett, P. H. Beton, N. R. Champness, J. H. Jefferson, G. A. D. Briggs, and D. G. Pettifor, Phys. Rev. Lett. **100**, 156101 (2008).

[156] K. Tahara, S. Lei, W. Mamdouh, Y. Yamaguchi, T. Ichikawa, H. Uji-i, M. Sonoda, K. Hirose, F. C. De Schryver, S. De Feyter, and Y. Tobe, J. Am. Chem. Soc. **130**, 6666 (2008).

[157] J. Lu, S.-B. Lei, Q.-D. Zeng, S.-Z. Kang, C. Wang, L.-J. Wan, and C.-L. Bai, J. Phys. Chem. B **108**, 5161 (2004).

[158] X.-H. Kong, K. Deng, Y.-L. Yang, Q.-D. Zeng, and C. Wang, J. Phys. Chem. C **111**, 17382 (2007).

[159] S.-S. Li, B. H. Northrop, Q.-H. Yuan, L.-J. Wan, and P. J. Stang, Acc. Chem. Res. **42**, 249 (2008).

[160] M. Li, K. Deng, S.-B. Lei, Y.-L. Yang, T.-S. Wang, Y.-T. Shen, C.-R. Wang, Q.-D. Zeng, and C. Wang, Angew. Chem. Int. Ed. **47**, 6717 (2008).

[161] R. Madueno, M. T. Raisanen, C. Silien, and M. Buck, Nature **454**, 618 (2008).

[162] S. Lei, M. Surin, K. Tahara, J. Adisoejoso, R. Lazzaroni, Y. Tobe, and S. D. Feyter, Nano Lett. **8**, 2541 (2008).

[163] B. Calmettes, S. Nagarajan, A. Gourdon, M. Abel, L. Porte, and R. Coratger, Angew. Chem. Int. Ed. **47**, 6994 (2008).

[164] O. Ivasenko, J. M. MacLeod, K. Y. Chernichenko, E. S. Balenkova, R. V. Shpanchenko, V. G. Nenajdenko, F. Rosei, and D. F. Perepichka, Chem. Commun., 1192 (2009).

[165] L. M. A. Perdigão, A. Saywell, G. N. Fontes, P. A. Staniec, G. Goretzki, A. G. Phillips, N. R. Champness, and P. H. Beton, Chem.-Eur. J. **14**, 7600 (2008).

[166] E. Barrena, D. G. de Oteyza, H. Dosch, and Y. Wakayama, ChemPhysChem **8**, 1915 (2007).

[167] S. De Feyter and F. C. De Schryver, Chem. Soc. Rev. **32**, 139 (2003).

[168] S. De Feyter, A. Gesquière, M. M. Abdel-Mottaleb, P. C. M. Grim, F. C. De Schryver, C. Meiners, M. Sieffert, S. Valiyaveettil, and K. Müllen, Acc. Chem. Res. **33**, 520 (2000).

[169] X. Zhang, T. Chen, H.-J. Yan, D. Wang, Q.-H. Fan, L.-J. Wan, K. Ghosh, H.-B. Yang, and P. J. Stang, ACS Nano **4**, 5685 (2010).

[170] W. D. Xiao, Y. H. Jiang, K. Aït-Mansour, P. Ruffieux, H. J. Gao, and R. Fasel, J. Phys. Chem. C **114**, 6646 (2010).

[171] A. Dmitriev, H. Spillmann, M. Lingenfelder, N. Lin, J. V. Barth, and K. Kern, Langmuir **20**, 4799 (2004).

[172] A. Dmitriev, H. Spillmann, N. Lin, J. V. Barth, and K. Kern, Angew. Chem Int. Ed. **42**, 2670 (2003).

[173] S. Stepanow, M. Lingenfelder, A. Dmitriev, H. Spillmann, E. Delvigne, N. Lin, X. Deng, C. Cai, J. V. Barth, and K. Kern, Nat. Mater. **3**, 229 (2004).

[174] P. Messina, A. Dmitriev, N. Lin, H. Spillmann, M. Abel, J. V. Barth, and K. Kern, J. Am. Chem. Soc. **124**, 14000 (2002).

[175] H. Spillmann, A. Dmitriev, N. Lin, P. Messina, J. V. Barth, and K. Kern, J. Am. Chem. Soc. **125**, 10725 (2003).

[176] S. Stepanow, N. Lin, J. V. Barth, and K. Kern, Chem. Commun., 2153 (2006).

[177] N. Lin, A. Dmitriev, J. Weckesser, J. V. Barth, and K. Kern, Angew. Chem Int. Ed. **41**, 4779 (2002).

[178] M. A. Lingenfelder, H. Spillmann, A. Dmitriev, S. Stepanow, N. Lin, J. V. Barth, and K. Kern, Chem.-Eur. J. **10**, 1913 (2004).

[179] S. Stepanow, N. Lin, J. V. Barth, and K. Kern, J. Phys. Chem. B **110**, 23472 (2006).

[180] N. Lin, S. Stepanow, F. Vidal, J. V. Barth, and K. Kern, Chem. Commun., 1681 (2005).

[181] N. Lin, A. Langner, S. L. Tait, C. Rajadurai, M. Ruben, and K. Kern, Chem. Commun., 4860 (2007).

[182] A. Langner, S. L. Tait, N. Lin, R. Chandrasekar, M. Ruben, and K. Kern, Angew. Chem. Int. Ed. **47**, 8835 (2008).

[183] A. Langner, S. L. Tait, N. Lin, C. Rajadurai, M. Ruben, and K. Kern, Proc. Natl. Acad. Sci. **104**, 17927 (2007).

[184] U. Schlickum, R. Decker, F. Klappenberger, G. Zoppellaro, S. Klyatskaya, M. Ruben, I. Silanes, A. Arnau, K. Kern, H. Brune, and J. V. Barth, Nano Lett. **7**, 3813 (2007).

[185] K. Tahara, S. Lei, J. Adisoejoso, S. De Feyter, and Y. Tobe, Chem. Commun. **46**, 8507 (2010).

[186] H. Spillmann, A. Kiebele, M. Stöhr, T. A. Jung, D. Bonifazi, F. Cheng, and F. Diederich, Adv. Mater. **18**, 275 (2006).

[187] D. Bonifazi, A. Kiebele, M. Stöhr, F. Cheng, T. Jung, F. Diederich, and H. Spillmann, Adv. Funct. Mater. **17**, 1051 (2007).

[188] S. Furukawa, K. Tahara, F. C. De Schryver, M. Van der Auweraer, Y. Tobe, and S. De Feyter, Angew. Chem. Int. Ed. **46**, 2831 (2007).

[189] D. Bléger, D. Kreher, F. Mathevet, A.-J. Attias, G. Schull, A. Huard, L. Douillard, C. Fiorini-Debuischert, and F. Charra, Angew. Chem. Int. Ed. **46**, 7404 (2007).

[190] K. Tahara, S. Furukawa, H. Uji-i, T. Uchino, T. Ichikawa, J. Zhang, W. Mamdouh, M. Sonoda, F. C. De Schryver, S. De Feyter, and Y. Tobe, J. Am. Chem. Soc. **128**, 16613 (2006).

[191] S. Furukawa, H. Uji-i, K. Tahara, T. Ichikawa, M. Sonoda, F. C. De Schryver, Y. Tobe, and S. De Feyter, J. Am. Chem. Soc. **128**, 3502 (2006).

[192] S. Lei, K. Tahara, X. Feng, S. Furukawa, F. C. De Schryver, K. Müllen, Y. Tobe, and S. De Feyter, J. Am. Chem. Soc. **130**, 7119 (2008).

[193] S. Lei, K. Tahara, F. C. De Schryver, M. Van der Auweraer, Y. Tobe, and S. De Feyter, Angew. Chem. Int. Ed. **47**, 2964 (2008).

[194] W. Xiao, X. Feng, P. Ruffieux, O. Gröning, K. Müllen, and R. Fasel, J. Am. Chem. Soc. **130**, 8910 (2008).

[195] J. Mao, H. Zhang, Y. Jiang, Y. Pan, M. Gao, W. Xiao, and H. J. Gao, J. Am. Chem. Soc. **131**, 14136 (2009).

[196] S. B. Lei, S. X. Yin, C. Wang, L. J. Wan, and C. L. Bai, Chem. Mater. **14**, 2837 (2002).

[197] T. Chen, Q. Chen, X. Zhang, D. Wang, and L.-J. Wan, J. Am. Chem. Soc. **132**, 5598 (2010).

[198] K. Wong, K.-Y. Kwon, B. V. Rao, A. Liu, and L. Bartels, J. Am. Chem. Soc. **126**, 7762 (2004).

[199] M. Böhringer, K. Morgenstern, W.-D. Schneider, M. Wühn, C. Wöll, and R. Berndt, Surf. Sci. **444**, 199 (2000).

[200] H. L. Zhang, W. Chen, H. Huang, L. Chen, and A. T. S. Wee, J. Am. Chem. Soc. **130**, 2720 (2008).

[201] H. L. Zhang, W. Chen, L. Chen, H. Huang, X. S. Wang, J. Yuhara, and A. T. S. Wee, Small **3**, 2015 (2007).

[202] W. Chen, H. L. Zhang, H. Huang, L. Chen, and A. T. S. Wee, Appl. Phys. Lett. **92**, 193301 (2008).

[203] L. Chen, W. Chen, H. Huang, H. L. Zhang, J. Yuhara, and A. T. S. Wee, Adv. Mater.

20, 484 (2008).

[204] D. G. de Oteyza, J. M. García-Lastra, M. Corso, B. P. Doyle, L. Floreano, A. Morgante, Y. Wakayama, A. Rubio, and J. E. Ortega, Adv. Funct. Mater. **19**, 3567 (2009).

[205] H. Zhang, W. D. Xiao, J. Mao, H. Zhou, G. Li, Y. Zhang, L. Liu, S. Du, and H. J. Gao, J. Phys. Chem. C **116**, 11091 (2012).

[206] L.-J. Wan, Acc. Chem. Res. **39**, 334 (2006).

[207] S. Yoshimoto, Y. Honda, O. Ito, and K. Itaya, J. Am. Chem. Soc. **130**, 1085 (2007).

[208] L. Piot, F. Silly, L. Tortech, Y. Nicolas, P. Blanchard, J. Roncali, and D. Fichou, J. Am. Chem. Soc. **131**, 12864 (2009).

[209] K. Suto, S. Yoshimoto, and K. Itaya, J. Am. Chem. Soc. **125**, 14976 (2003).

[210] T. Kudernac, S. Lei, J. A. A. W. Elemans, and S. De Feyter, Chem. Soc. Rev. **38**, 402 (2009).

[211] R. M. Kramer, C. Li, D. C. Carter, M. O. Stone, and R. R. Naik, J. Am. Chem. Soc. **126**, 13282 (2004).

[212] M. T. Klem, D. Willits, D. J. Solis, A. M. Belcher, M. Young, and T. Douglas, Adv. Funct. Mater. **15**, 1489 (2005).

[213] T. Chen, W.-H. Yang, D. Wang, and L.-J. Wan, Nat. Commun. **4**, 1389 (2013).

[214] J. S. Seo, D. Whang, H. Lee, S. I. Jun, J. Oh, Y. J. Jeon, and K. Kim, Nature **404**, 982 (2000).

[215] M. E. Davis, Nature **417**, 813 (2002).

[216] C. J. Kepert, T. J. Prior, and M. J. Rosseinsky, J. Am. Chem. Soc. **122**, 5158 (2000).

[217] M. Fujita, Y. J. Kwon, S. Washizu, and K. Ogura, J. Am. Chem. Soc. **116**, 1151 (1994).

[218] T. R. Cook, Y.-R. Zheng, and P. J. Stang, Chem. Rev. **113**, 734 (2012).

[219] M. Yoon, R. Srirambalaji, and K. Kim, Chem. Rev. **112**, 1196 (2011).

[220] A. Corma, H. García, and F. X. Llabrés i Xamena, Chem. Rev. **110**, 4606 (2010).

[221] J. V. Barth, Surf. Sci. **603**, 1533 (2009).

[222] O. M. Yaghi, G. Li, and H. Li, Nature **378**, 703 (1995).

[223] M. E. Kosal, J.-H. Chou, S. R. Wilson, and K. S. Suslick, Nat. Mater. **1**, 118 (2002).

[224] M. Eddaoudi, H. Li, and O. M. Yaghi, J. Am. Chem. Soc. **122**, 1391 (2000).

[225] H. Li, M. Eddaoudi, T. L. Groy, and O. M. Yaghi, J. Am. Chem. Soc. **120**, 8571 (1998).

[226] M. Eddaoudi, J. Kim, N. Rosi, D. Vodak, J. Wachter, M. O'Keeffe, and O. M. Yaghi, Science **295**, 469 (2002).

[227] N. L. Rosi, J. Eckert, M. Eddaoudi, D. T. Vodak, J. Kim, M. O'Keeffe, and O. M. Yaghi, Science **300**, 1127 (2003).

[228] A. J. Fletcher, E. J. Cussen, T. J. Prior, M. J. Rosseinsky, C. J. Kepert, and K. M. Thomas, J. Am. Chem. Soc. **123**, 10001 (2001).

[229] J.-R. Li, J. Sculley, and H.-C. Zhou, Chem. Rev. **112**, 869 (2011).

[230] B. Chen, S. Xiang, and G. Qian, Acc. Chem. Res. **43**, 1115 (2010).

[231] B. Moulton, J. Lu, R. Hajndl, S. Hariharan, and M. J. Zaworotko, Angew. Chem. Int. Ed. **41**, 2821 (2002).

[232] H. Srikanth, R. Hajndl, B. Moulton, Zaworotko, and J. M, J. Appl. Phys. **93**, 7089

(2003).
233 D. Maspoch, D. Ruiz-Molina, K. Wurst, N. Domingo, M. Cavallini, F. Biscarini, J. Tejada, C. Rovira, and J. Veciana, Nat. Mater. **2**, 190 (2003).
234 Y. Li Huang, Y. Lu, T. C. Niu, H. Huang, S. Kera, N. Ueno, A. T. S. Wee, and W. Chen, Small **8**, 1423 (2012).
235 H. Yanagi, K. Ikuta, H. Mukai, and T. Shibutani, Nano Lett. **2**, 951 (2002).
236 Y. Wang, J. r. Kröger, R. Berndt, and W. A. Hofer, J. Am. Chem. Soc. **131**, 3639 (2009).
237 H. Wende, M. Bernien, J. Luo, C. Sorg, N. Ponpandian, J. Kurde, J. Miguel, M. Piantek, X. Xu, Ph. Eckhold, W. Kuch, K. Baberschke, P. M. Panchmatia, B. Sanyal, P. M. Oppeneer, and O. Eriksson, Nat. Mater. **6**, 516 (2007).
238 M. Alemani, M. V. Peters, S. Hecht, K.-H. Rieder, F. Moresco, and L. Grill, J. Am. Chem. Soc. **128**, 14446 (2006).
239 J. V. Barth, G. Costantini, and K. Kern, Nature **437**, 671 (2005).
240 F. Rosei, J. Phys.: Condens. Matter. **16**, S1373 (2004).
241 F. Tao and S. L. Bernasek, Chem. Rev. **107**, 1408 (2007).
242 W. Chen and A. T. S. Wee, J. Phys. D: Appl. Phys. **40**, 6287 (2007).
243 F. Rosei, M. Schunack, Y. Naitoh, P. Jiang, A. Gourdon, E. Laegsgaard, I. Stensgaard, C. Joachim, and F. Besenbacher, Prog. Surf. Sci. **71**, 95 (2003).
244 J. V. Barth, Surf. Sci. Rep. **40**, 75 (2000).
245 J. K. Gimzewski and C. Joachim, Science **283**, 1683 (1999).
246 F. Vonau, D. Suhr, D. Aubel, L. Bouteiller, G. Reiter, and L. Simon, Phys. Rev. Lett. **94**, 066103 (2005).
247 F. Vonau, D. Aubel, L. Bouteiller, G. Reiter, and L. Simon, Phys. Rev. Lett. **99**, 086103 (2007).
248 K. W. Hipps, L. Scudiero, D. E. Barlow, and M. P. Cooke, J. Am. Chem. Soc. **124**, 2126 (2002).
249 J. V. Barth, Ann. Rev. Phys. Chem. **58**, 375 (2007).
250 D. Bonifazi, S. Mohnani, and A. Llanes-Pallas, Chem.-Eur. J. **15**, 7004 (2009).
251 T. Yokoyama, T. Takahashi, K. Shinozaki, and M. Okamoto, Phys. Rev. Lett. **98**, 206102 (2007).
252 H. Brune, M. Giovannini, K. Bromann, and K. Kern, Nature **394**, 451 (1998).
253 V. Marsico, M. Blanc, K. Kuhnke, and K. Kern, Phys. Rev. Lett. **78**, 94 (1997).
254 S. Lukas, G. Witte, and C. Wöll, Phys. Rev. Lett. **88**, 028301 (2001).
255 W. Chen, H. Li, H. Huang, Y. Fu, H. L. Zhang, J. Ma, and A. T. S. Wee, J. Am. Chem. Soc. **130**, 12285 (2008).
256 I. Fernandez-Torrente, S. Monturet, K. J. Franke, J. Fraxedas, N. Lorente, and J. I. Pascual, Phys. Rev. Lett. **99**, 176103 (2007).
257 S. Blankenburg and W. G. Schmidt, Phys. Rev. Lett. **99**, 196107 (2007).
258 Q. Chen and N. V. Richardson, Nat. Mater. **2**, 324 (2003).
259 S. Blankenburg and W. G. Schmidt, Phys. Rev. B **74**, 155419 (2006).
260 M. Preuss, W. G. Schmidt, and F. Bechstedt, Phys. Rev. Lett. **94**, 236102 (2005).
261 K. Pohl, M. C. Bartelt, J. de la Figuera, N. C. Bartelt, J. Hrbek, and R. Q. Hwang, Nature **397**, 238 (1999).

[262] M. Corso, W. Auwärter, M. Muntwiler, A. Tamai, T. Greber, and J. Osterwalder, Science **303**, 217 (2004).
[263] H. Dil, J. Lobo-Checa, R. Laskowski, P. Blaha, S. Berner, J. Osterwalder, and T. Greber, Science **319**, 1824 (2008).
[264] M. Böhringer, K. Morgenstern, W.-D. Schneider, R. Berndt, F. Mauri, A. De Vita, and R. Car, Phys. Rev. Lett. **83**, 324 (1999).
[265] C. Didiot, S. Pons, B. Kierren, Y. Fagot-Revurat, and D. Malterre, Surf. Sci. **600**, 3917 (2006).
[266] N. Weiss, T. Cren, M. epple, S. Rusponi, G. Baudot, S. Rohart, A. Tejeda, V. Repain, S. Rousset, P. Ohresser, F. Scheurer, P. Bencok, and H. Brune, Phys. Rev. Lett. **95**, 157204 (2005).
[267] P. Gambardella, M. Blanc, H. Brune, K. Kuhnke, and K. Kern, Phys. Rev. B **61**, 2254 (2000).
[268] J. Repp, F. Moresco, G. Meyer, K.-H. Rieder, P. Hyldgaard, and M. Persson, Phys. Rev. Lett. **85**, 2981 (2000).
[269] N. Knorr, H. Brune, M. Epple, A. Hirstein, M. A. Schneider, and K. Kern, Phys. Rev. B **65**, 115420 (2002).
[270] F. Silly, M. Pivetta, M. Ternes, F. Patthey, J. P. Pelz, and W.-D. Schneider, Phys. Rev. Lett. **92**, 016101 (2004).
[271] M. Ternes, C. Weber, M. Pivetta, F. Patthey, J. P. Pelz, T. Giamarchi, F. Mila, and W.-D. Schneider, Phys. Rev. Lett. **93**, 146805 (2004).
[272] S. U. Nanayakkara, E. C. H. Sykes, L. C. Fernández-Torres, M. M. Blake, and P. S. Weiss, Phys. Rev. Lett. **98**, 206108 (2007).
[273] T. Steiner, Angew. Chem. Int. Ed. **41**, 48 (2002).
[274] H. Liang, Y. He, Y. Ye, X. Xu, F. Cheng, W. Sun, X. Shao, Y. Wang, J. Li, and K. Wu, Coord. Chem. Rev. **253**, 2959 (2009).
[275] G. Binnig, H. Rohrer, C. Gerber, and E. Weibel, Appl. Phys. Lett. **40**, 178 (1982).
[276] G. Binnig, H. Rohrer, C. Gerber, and E. Weibel, Phys. Rev. Lett. **50**, 120 (1983).
[277] J. A. Kubby and J. J. Boland, Surf. Sci. Rep. **26**, 61 (1996).
[278] J. Tersoff and D. R. Hamann, Phys. Rev. Lett. **50**, 1998 (1983).
[279] J. Tersoff and D. R. Hamann, Phys. Rev. B **31**, 805 (1985).
[280] R. A. Wolkow, Ann. Rev. Phys. Chem. **50**, 413 (1999).
[281] C. J. Chen, Introduction to Scanning Tunneling Microscopy, Oxford University Press, New York (2008).
[282] R. J. Hamers, Ann. Rev. Phys. Chem. **40**, 531 (1989).
[283] R. Wiesendanger, H.-J. Guntherodt, Scanning Tunneling Microscopy I: General Principles and Applications to Clean and Adsorbate-covered Surfaces, Springer, New York (1992).
[284] R. Martel, P. Avouris, and I.-W. Lyo, Science **272**, 385 (1996).
[285] B. C. Stipe, M. A. Rezaei, and W. Ho, Science **280**, 1732 (1998).
[286] W. Chen, H. Li, H. Huang, Y. Fu, H. L. Zhang, J. Ma, and A. T. S. Wee, J. Am. Chem. Soc. **130**, 12285 (2008).
[287] W. Chen, H. L. Zhang, H. Huang, L. Chen, and A. T. S. Wee, Appl. Phys. Lett. **92**, 193301 (2008).

[288] S. Hüfner, *Photoelectron Spectroscopy: Principles and Applications* (Springer, 2003).
[289] S. Zhong, J. Q. Zhong, H. Y. Mao, J. L. Zhang, J. D. Lin, and W. Chen, Phys. Chem. Chem. Phys. **14**, 14127 (2012).
[290] N. Koch, J. Phys.: Condens. Matt. **20**, 184008 (2008).
[291] W. Chen, D. Qi, X. Gao, and A. T. S. Wee, Prog. Surf. Sci. **84**, 279 (2009).
[292] J. Q. Zhong, H. Huang, H. Y. Mao, R. Wang, S. Zhong, and W. Chen, J. Chem. Phys. **134**, 154706 (2011).
[293] J. Q. Zhong, H. Y. Mao, R. Wang, J. D. Lin, Y. B. Zhao, J. L. Zhang, D. G. Ma, and W. Chen, Org. Electron. **13**, 2793 (2012).
[294] V. Coropceanu, J. Cornil, D. A. da Silva Filho, Y. Olivier, R. Silbey, and J.-L. Brédas, Chem. Rev. **107**, 926 (2007).
[295] N. L. Rosi and C. A. Mirkin, Chem. Rev. **105**, 1547 (2005).
[296] J. P. RABE and S. BUCHHOLZ, Science **253**, 424 (1991).
[297] F. Tao and S. L. Bernasek, Chem. Rev. **107**, 1408 (2007).
[298] H. J. Gao and L. Gao, Prog. Surf. Sci. **85**, 28 (2010).
[299] Y. Ye, W. Sun, Y. Wang, X. Shao, X. Xu, F. Cheng, J. Li, and K. Wu, J. Phys. Chem. C **111**, 10138 (2007).
[300] G.-B. Pan, J.-M. Liu, H.-M. Zhang, L.-J. Wan, Q.-Y. Zheng, and C.-L. Bai, Angew. Chem. Int. Ed. **42**, 2747 (2003).
[301] M. de Wild, S. Berner, H. Suzuki, H. Yanagi, D. Schlettwein, S. Ivan, A. Baratoff, H.-J. Guentherodt, and T. A. Jung, ChemPhysChem **3**, 881 (2002).
[302] B. Xu, C. Tao, E. D. Williams, and J. E. Reutt-Robey, J. Am. Chem. Soc. **128**, 8493 (2006).
[303] S. Yoshimoto, E. Tsutsumi, R. Narita, Y. Murata, M. Murata, K. Fujiwara, K. Komatsu, O. Ito, and K. Itaya, J. Am. Chem. Soc. **129**, 4366 (2007).
[304] R. Wang, H. Y. Mao, H. Huang, D. C. Qi, and W. Chen, J. Appl. Phys. **109** (2011).
[305] W. Chen, H. L. Zhang, H. Huang, L. Chen, and A. T. S. Wee, Appl. Phys. Lett. **92** (2008).
[306] W. Chen, H. Zhang, H. Huang, L. Chen, and A. T. S. Wee, ACS Nano **2**, 693 (2008).
[307] H. L. Zhang, W. Chen, H. Huang, L. Chen, and A. T. S. Wee, J. Am. Chem. Soc. **130**, 2720 (2008).
[308] Y. L. Huang, W. Chen, H. Li, J. Ma, J. Pflaum, and A. T. S. Wee, Small **6**, 70 (2010).
[309] Y. L. Huang, W. Chen, and A. T. S. Wee, J. Am. Chem. Soc. **133**, 820 (2010).
[310] J. A. Lipton-Duffin, O. Ivasenko, D. F. Perepichka, and F. Rosei, Small **5**, 592 (2009).
[311] N. Koch, ChemPhysChem **8**, 1438 (2007).
[312] P. Peumans, S. Uchida, and S. R. Forrest, Nature **425**, 158 (2003).
[313] F. Yang, M. Shtein, and S. R. Forrest, Nat. Mater. **4**, 37 (2005).
[314] W. Ma, C. Yang, X. Gong, K. Lee, and A. J. Heeger, Adv. Funct. Mater. **15**, 1617 (2005).
[315] R. Otero, D. Écija, G. Fernández, J. M. Gallego, L. Sánchez, N. Martín, and R. Miranda, Nano Lett. **7**, 2602 (2007).
[316] L. Sánchez, R. Otero, J. M. a. Gallego, R. Miranda, and N. Martín, Chem. Rev. **109**, 2081 (2009).

[317] S. Uchida, J. Xue, B. P. Rand, and S. R. Forrest, Appl. Phys. Lett. **84**, 4218 (2004).
[318] D. B. Dougherty, W. Jin, W. G. Cullen, J. E. Reutt-Robey, and S. W. Robey, J. Phys. Chem. C **112**, 20334 (2008).
[319] P. A. Heiney, J. E. Fischer, A. R. McGhie, W. J. Romanow, A. M. Denenstein, J. P. McCauley Jr, A. B. Smith, and D. E. Cox, Phys. Rev. Lett. **66**, 2911 (1991).
[320] L.-L. Wang and H.-P. Cheng, Phys. Rev. B **69**, 165417 (2004).
[321] P. Lambin, A. A. Lucas, and J. P. Vigneron, Phys. Rev. B **46**, 1794 (1992).
[322] H. Ishii, K. Sugiyama, E. Ito, and K. Seki, Adv. Mater. **11**, 605 (1999).
[323] W. Chen, D.-C. Qi, H. Huang, X. Gao, and A. T. S. Wee, Adv. Funct. Mater. **21**, 410 (2011).
[324] J. Hwang, A. Wan, and A. Kahn, Mater. Sci. Eng. R **64**, 1 (2009).
[325] Q. Liu, Y. Y. Zhang, N. Jiang, H. G. Zhang, L. Gao, S. X. Du, and H. J. Gao, Phys. Rev. Lett. **104**, 166101 (2010).
[326] A. Zhao, Q. Li, L. Chen, H. Xiang, W. Wang, S. Pan, B. Wang, X. Xiao, J. Yang, J. G. Hou, and Q. Zhu, Science **309**, 1542 (2005).
[327] S.-B. Lei, K. Deng, D.-L. Yang, Q.-D. Zeng, and C. Wang, J. Phys. Chem. B **110**, 1256 (2006).
[328] G. V. Nazin, X. H. Qiu, and W. Ho, Science **302**, 77 (2003).
[329] H. Fukagawa, S. Hosoumi, H. Yamane, S. Kera, and N. Ueno, Phys. Rev. B **83**, 085304 (2011).
[330] T. Niu, C. Zhou, J. Zhang, S. Zhong, H. Cheng, and W. Chen, J. Phys. Chem. C **116**, 11565 (2012).
[331] S. L. Wong, H. Huang, Y. Wang, L. Cao, D. Qi, I. Santoso, W. Chen, and A. T. S. Wee, ACS Nano **5**, 7662 (2011).
[332] L. Scifo, M. Dubois, M. Brun, euml, P. Rannou, S. Latil, A. Rubio, and B. Grévin, Nano Lett. **6**, 1711 (2006).
[333] Y. Ning, J. Jiang, Z. Shi, Q. Fu, J. Liu, Y. Luo, B. Z. Tang, and N. Lin, J. Phys. Chem. C **113**, 26 (2008).
[334] D. I. Gittins, D. Bethell, D. J. Schiffrin, and R. J. Nichols, Nature **408**, 67 (2000).
[335] K. Walzer and M. Hietschold, Surf. Sci. **471**, 1 (2001).
[336] M. Lackinger, T. Müller, T. G. Gopakumar, F. Müller, M. Hietschold, and G. W. Flynn, J. Phys. Chem. B **108**, 2279 (2004).
[337] K. W. Hipps and J. J. Hoagland, Langmuir **7**, 2180 (1991).
[338] U. Mazur and K. W. Hipps, J. Phys. Chem. **99**, 6684 (1995).
[339] K. W. Hipps, D. E. Barlow, and U. Mazur, J. Phys. Chem. B **104**, 2444 (2000).
[340] K. W. Hipps and L. Scudiero, J. Chem. Educ. **82**, 704 (2005).
[341] T. C. Niu, Y. L. Huang, J. T. Sun, S. Kera, N. Ueno, A. T. S. Wee, and W. Chen, Appl. Phys. Lett. **99**, 143114 (2011).
[342] T. G. Gopakumar, H. Tang, J. Morillo, and R. Berndt, J. Am. Chem. Soc. **134**, 11844 (2012).
[343] M. Bernien, J. Miguel, C. Weis, Md. E. Ali, J. Kurde, B. Krumme, P. M. Panchmatia, B. Sanyal, M. Piantek, P. Srivastava, K. Baberschke, P. M. Oppeneer, O. Eriksson, W. Kuch, and H. Wende, Phys. Rev. Lett. **102**, 047202 (2009).
[344] M. Bernien, X. Xu, J. Miguel, M. Piantek, Ph. Eckhold, J. Luo, J. Kurde, W. Kuch, K.

Baverschke, H. Wende, and P. Srivastava, Phys. Rev. B **76**, 214406 (2007).
345 W. Chen, H. Huang, and A. T. S. Wee,. Chem. Commun. 4276 (2008).